SYSTEM INTEGRATION, SIGNAL PROCESSING AND APPLICATION OF SMART COMPRESSION WEARABLE SYSTEM

HENG LUO

PhD

The Hong Kong Polytechnic University

2025

The Hong Kong Polytechnic University
School of Fashion and Textiles

System Integration, Signal Processing and Application of Smart Compression Wearable System

Heng LUO

A thesis submitted in partial fulfillment of the requirements for the degree of Doctor of Philosophy

September 2024

CERTIFICATE OF ORIGINALITY

I hereby declare that this thesis is my own work and that, to the best of my knowledge and belief, it reproduces no material previously published or written, nor material that has been accepted for the award of any other degree or diploma, except where due acknowledgement has been made in the text.

(Signed)

_____

Heng LUO (Name of student)

_____

ABSTRACT

Compression therapies have a historical tradition spanning thousands of years. In contemporary practice, compression garments are extensively utilized for managing chronic venous diseases, scar management, orthopedic applications, body shaping, sportswear, and other uses. The development of imperceptible, multifunctional, long-term wearable smart compression garments is highly desirable, as these can monitor pressure variations and provide valuable information during therapy, potentially enhancing therapeutic efficacy. However, traditional compression garments lack real-time pressure measurement capabilities.

Several laboratory investigations into smart compression garments have been conducted by various researchers, but these prototypes are often single-functional, bulky, and unsuitable for prolonged wear. Consequently, this study proposed an innovative integrated smart compression wearable system, comprising compression garments, embedded fabric capacitive pressure sensors, edge control units, interactive user interfaces, and dedicated software applications. This system offers numerous advantages, including high sensitivity to low pressure, mechanical flexibility, integration with external systems, rapid internal component upgrades and simplified repairs, configurable software parameters and modular hardware components, and a low cost of US$ 33.

To accurately measure static and dynamic pressure on the human body, textile capacitive pressure sensors with a sandwich structure were designed, tested, and integrated. These sensors feature a dielectric layer filled with polydimethylsiloxane mixed with carbon black powder and roughened by abrasive papers. The laboratory-fabricated sensors exhibit several benefits, including facile fabrication, low cost, satisfactory accuracy and repeatability, high conformity to curved surfaces, adjustable integration with compression garments, high sensitivity below 50 mmHg, energy-efficient design, and rapid response times.

The sensing performance of the smart compression garment system is compromised by parasitic capacitances caused by surrounding electromagnetic interference, proximity effects, and deformation on curved surfaces, which manifest as frequency-overlapped and non-stationary noise in real-world applications. Traditional deterministic and stochastic signal processing methods are inadequate for improving denoising performance. Therefore, a novel encoder-decoder deep neural network architecture was developed to enhance noise reduction and achieve high-resolution pressure detection. This architecture employs stacked autoencoders for the encoders and is trained for various tasks for the decoders, offering high interpretability, cost-effective unsupervised learning, and compatibility with edge control units with limited computational and storage capacities.

Empirical validations included 100-minute flat surface pressure recordings with seven standard weights, producing 22,498 capacitance-pressure data pairs for algorithm training

and testing. The algorithms achieved a root mean square error (RMSE) in pressure measurement of 0.7891 mmHg, a 38% improvement over traditional polynomial regression methods. Subsequent fine-tuning over 1000 epochs with the substitution of various frozen encoders resulted in an RMSE of approximately 0.9 mmHg. Additionally, the system's effectiveness was verified through 12-minute curved surface pressure recordings over ten days, producing 75,888 capacitance-pressure data pairs. The textile capacitive pressure sensors were attached to position B, B1, and C on a medium-sized wooden mannequin leg, with a sphygmomanometer used to tightly wrap the sensor on the leg and exert seven different pressure levels. The algorithms exhibited RMSEs of 0.0283 mmHg, 0.0633 mmHg, and 0.0387 mmHg for positions B, B1, and C, respectively, representing improvements of 98%, 97%, and 98% over traditional polynomial regression methods.

Continuous monitoring of lower extremity muscle function is essential, given the critical role these muscles play in posture maintenance, locomotion, and dynamic movements. However, conventional assessment techniques, such as electromyography and physiological cross-sectional area measurements, often lack the capacity to deliver accurate, real-time data while maintaining user comfort and practicality in both clinical and community environments. To address these challenges, this study introduced an application of the proposed smart compression stocking system.

A clinical validation study was conducted involving twelve healthy young adults who performed maximum voluntary isometric contractions of ankle plantarflexion under

standardized conditions. Muscle force data were collected simultaneously using the smart compression stocking system and a calibrated Humac NORM dynamometer, which served as the reference standard. Statistical analysis demonstrated strong linear correlations between the outputs of the two systems, with correlation coefficients exceeding 0.92. Further, two-way analysis of variance demonstrated that the ankle joint angle ($p = 0.055$) had a more significant impact on measurement outcomes compared to inter-participant variability ($p = 0.290$). These results validate the smart compression stocking system as a reliable and practical tool for monitoring lower extremity muscle force during isometric contractions. The system holds significant potential for applications in clinical assessment, rehabilitation monitoring, and sports performance evaluation.

In summary, this thesis comprehensively and systematically studied, designed, implemented, and optimized wearable capacitive pressure sensors, tailored system integration of the smart compression garment system, unified signal processing methods, and evaluated the system by healthcare applications. The aim is to deliver cost-effective pressure management and relevant healthcare information for anyone, anytime, anywhere.

PUBLICATIONS

1. Refereed Journal Papers - directly from this research

1. Luo, H., Xiong, Y., Zhu, M., Wei, X. and Tao, X., 2024. Integrated Wearable System for Monitoring Skeletal Muscle Force of Lower Extremities. *Sensors (Basel, Switzerland)*, *24*(14).
2. Luo, H., Xiong, Y., X. and Tao, X., 2024. Smart Compression Stockings Driven By Interpretable Unsupervised Deep Learning. *International Journal of Intelligent Systems*. Under review.

2. Refereed Journal Papers - from other projects during my PhD

1. Bao, Q., Zhang, Z., Luo, H. and Tao, X., 2022. Evaluating and Modeling the Degradation of PLA/PHB Fabrics in Marine Water. *Polymers*, *15*(1), p.82.
2. Yang, S., Tao, X., Chen, W., Mao, J., Luo, H., Lin, S., Zhang, L. and Hao, J., 2022. Ionic Hydrogel for Efficient and Scalable Moisture-Electric Generation. *Advanced Materials*, *34*(21), p.2200693.

3. Patents

1. X.M. Tao, Y. Xiong, X. Wang, H. Luo, K. Ma, S. Liu, Method for Customized Design of Compression Stockings Based on the Profile of the Lower Limb, Chinese Patent, Application submitted.
2. Y. Xiong, H. Luo, X.M. Tao, Computer aided design (CAD) module for customized

design of compression stockings, Chinese Patent, Application submitted.

3. X.M. Tao, J. Li, H. Luo, L.L. Ma, Fast test system for surface concentration of antimicrobial agents and prediction model for antimicrobial properties, Chinese Patent, Application submitted.

ACKNOWLEDGEMENTS

It is an honor for me to begin PhD research life in the Hong Kong Polytechnic University in 2021. I tried my best to grasp this opportunity to broaden my horizon and furthermore explore the area that had been touched or dived into so deeply. This journey was not an even way, but I kept to the Deming cycle practice, that is Plan-Do-Check-Act. Through this process, I practiced learning by doing. I would like to express gratitude to those failure moments, as Friedrich Nietzsche pointed out "that which does not kill us makes us stronger." Going through a difficult time in the COVID-19 pandemic, I cherished that “all human wisdom is contained in these two words: wait and hope”.

I would like to wholeheartedly express my deep appreciation to my supervisor for her invaluable guidance, support, and mentorship throughout the course of this endeavor. Prof. Xiaoming Tao is more than a globally revered scholar giant but also an everlasting spiritual model who devotes her whole life to her research career and never wastes one day. Prof. Tao has broad interests in electronics, textiles, materials, and others. It is much more impressive for everyone who works with her that she is curious about emerging new things and understands the fundamental mechanism at a fast speed that has been almost never seen in any others. For everyone around her, “she lifts the lamp besides the golden door!”

I also would like to express my gratitude to my fellow group members: Dr. Ying Xiong, Dr. Su Yang, Dr. Bao Yang, Dr. Xi Wang, Dr. Su Liu, Dr. Bo Fang, Dr. Qi Bao, Dr. Lisha Zhang,

Dr. Jun Li, Dr. Shuping Lin, Dr. Ziheng Zhang, Dr. Junhong Pu, Mr. Shirui Liu, Ms. Xujiao Ding, Ms. Kit Ming Ma, Ms. Jinli Piao, Ms. Linlin Ma, Mr. Jin Liu, Mr. Songge Zhang, Mr. Shengyang Tang, Mr. Jingyang Wu, Ms. Jing Yang. I sincerely appreciate their kind help and support.

I would like to extend my sincere appreciation to the esteemed panels for their unwavering dedication and meticulous review throughout this process. Gratitude is also due to The Hong Kong Polytechnic University and the School of Fashion and Textiles for their invaluable support. Furthermore, I would like to express my heartfelt thanks to the laboratory personnel and technicians for their technical assistance, as well as for the diligent efforts of the general officers involved. Their collective contributions have been instrumental in the successful execution of this endeavor.

Finally, I would like to thank my parents and my friends for continuously supporting me through this hard journey of discovery. Thank you for your meticulous caring and tolerant love.

TABLE OF CONTENTS

LIST OF FIGURES

LIST OF TABLES

NOMENCLATURE

General Symbols

C	Capacitance
P	Pressure
T	Tensile force
r	Radius
A	Contact area
$\boldsymbol{\varepsilon}$	Permittivity
ε_0	Free space permittivity
ε_r	Relative permittivity
d	Distance
$\boldsymbol{x_{max}}$	The maximum number in x
$\boldsymbol{x_{min}}$	The minimum number in x
$\boldsymbol{\hat{y}}$	The ground truth value of y
m	Mass
g	The acceleration of gravity ($9.8\ N/Kg$)
s	Contact area
NT	Muscle Torque
RR	Correlation Coefficients
rr	Correlation Coefficients
$\boldsymbol{C_{norm}}$	Normalized Capacitance
$\boldsymbol{NT_{norm}}$	Normalized Muscle Torque

A	uppercase Alpha fitting coefficient (slope)
B	uppercase Beta fitting coefficient (intercept)
$\boldsymbol{\alpha}$	lowercase Alpha fitting coefficient (slope) after normalization
$\boldsymbol{\beta}$	lowercase Beta fitting coefficient (intercept) after normalization

Abbreviations

MCS	Medical Compression Stocking
CVD	Chronic Venous Disease
EMG	Electromyography
ECG	Electrocardiogram
EEG	Electroencephalogram
PD	Parkinson's Disease
FoG	Freezing of Gaits
PDMS	Polydimethylsiloxane
TPU	Thermoplastic Polyurethane
CB	Carbon Black
ABS	Acrylonitrile Butadiene Styrene
SRAM	Static Random Access Memory
LED	Light-Emitting Diode
CMOS	Complementary Metal-Oxide-Semiconductor
SoC	System on Chip
RISC	Reduced Instruction Set Computer
PCB	Printed Circuit Board
SPI	Serial Peripheral Interface
I2C	Inter-Integrated Circuit
UART	Universal Asynchronous Receiver-Transmitter
USART	Universal Synchronous and Asynchronous Receiver-Transmitter
APB	Advanced Peripheral Bus
USB	Universal Serial Bus
CAN	Controller Area Network
BLE	Bluetooth Low Energy
SQL	Structured Query Language

API	Application Programming Interface
SDK	Software Development Kit
UI	User Interface
BOM	Bill of Material
ADC	Analog-to-Digital Converter
SQNR	Signal-to-Quantization-Noise Ratio
SNR	Signal-to-Noise Ratio
IIR	Infinite Impulse Response
FIR	Finite Impulse Response
FT	Fourier Transform
CTFS	Continuous Time Fourier Series
CTFT	Continuous Time Fourier Transform
DTFS	Discrete Time Fourier Series
DTFT	Discrete Time Fourier Transform
FFT	Fast Fourier Transform
MLE	Maximum Likelihood Estimation
MAP	Maximum A Posteriori Estimation
IID	Independent and Identical Distributed
PDF	Probability Density Function
TFR	Time-Frequency Representation
STFT	Short-Term Fourier Transform
PSD	Power Spectral Density
WT	Wavelet Transform
CWT	Continuous Wavelet Transform
DWT	Discrete Wavelet Transform
ARIMA	Autoregressive Integrated Moving Average
ARMA	Autoregressive Moving Average
AR	Autoregression

MA	Moving Average
ACF	Autocorrelation Function
PACF	Partial Autocorrelation Function
AIC	Akaike Information Criterion
BIC	Bayesian Information Criterion
CRISP-DM	Cross-Industry Standard Process for Data Mining
ML	Machine Learning
DL	Deep Learning
NN	Neural Networks
MLP	Multi-Layer Perceptron
CNN	Convolutional Neural Network
RNN	Recurrent Neural Network
SGD	Stochastic Gradient Descent
PCSA	Physiological Cross-Sectional Area
ATP	Adenosine Triphosphate
MRI	Magnetic Resonance Imaging
CT	Computed Tomography
IOT	Internet of Things
IP	Internet Protocol
LAN	Local Area Network
MSE	Mean Square Error
RMSE	Root Mean Square Error
LMS	Least Mean Square
EMD	Empirical Mode Decomposition
LSTM	Long Short-Term Memory
GRU	Gated Recurrent Unit
PCA	Principal Component Analysis
DAE	Denoising Autoencoder

CAE	Contractive Autoencoder
SAE	Sparse Autoencoder
VAE	Variational Autoencoder
AAE	Adversarial Autoencoder
GAN	Generative Adversarial Network
FLOP	Floating-point Operation
ReLU	Rectified Linear Unit
FPGA	Field Programmable Gate Array
DSP	Digital Signal Processor
STIMES	Smart Textile-Integrated Microelectronic Systems
NUI	Natural User Interface
ANOVA	Analysis of Variance
IaaS	Infrastructure as a Service
PaaS	Platform as a Service
SaaS	Software as a Service
HTTPS	Hypertext Transfer Protocol Secure
GCP	Google Cloud Platform
CI	Continuous Integration
CD	Continuous Delivery
BMI	Body Mass Index
MVIC	Maximum Voluntary Isometric Contraction
OLTP	Online Transaction Processing
OLAP	Online Analytical Processing
BD	Big Data
FL	Federated Learning

Chapter 1 Introduction

1.1. Background

Various functional garments are widely used and attract more and more attention; among them, compression garments are one broad unique functional category. Currently, commercialized off-the-shelf compression garments utilize elastomeric fibers and yarns and well-designed fabric structures to generate appropriate mechanical pressure, so that contact human skins and underlying tissues are supported, stabilized, compressed, and strained. Furthermore, transmitting pressure from the surface to the internal is beneficial for skin healing, blood circulation, lymph circulation, and capillary reabsorption. Therefore, compression garments are generally recommended for medical curing applications, athletic applications, body shaping applications, and geriatric healthcare applications [1-4].

In retrospect along the historical timeline, Hippocrates of Kos, who was a Greek physician during the Age of Pericles and renowned as the “Father of Medicine”, mentioned the compression therapy, which utilized externally exerted pressure to fix the posture of wounded lower extremities resisting against natural gravity with the aim of better heal. Other invented devices could also benefit this healing according to various wounded parts [5]. In 1628, William Harvey studied the relationship between venous stasis and external pressure, which prompted

later on emerging kinds of compression therapy methods, such as laced stocking, elastic bands, tight bandage with resin, cellulose fiber stocking, chemical fiber stocking (acrylic, nylon, polyester) [6]. Not until the 19th century when mass production of commercial bandages came up and was wildly used in clinical trials, compression therapy became much more popular and effective. In the meantime, compression stockings with elastomer yarns were first introduced to produce graduated compression distribution [7, 8]. After that, in the 20th century compression therapy was used to cure burned skin to accelerate scar formation and alleviate hypertrophic scars [9].

To achieve high performance of effective and efficient healing, several characteristics of compression garments are highlighted and set higher priorities, such as graduated compression distribution (higher pressure at the ankle and lower pressure at the thigh), pressure gradient distribution (avoiding partially reverse pressure gradients), stability, flexibility, duration, biosafety. It was studied that the discomfort pressure range is approximately 5.88-9.80 kPa (44.1-73.5 mmHg), although this is distinct according to individual preference difference, healing body parts difference, therapy approaches difference, which however is indicated as a little more than the average blood pressure in capillaries close to skin surface of approximate 4.30 kPa (32.3 mmHg). High external pressure might obstruct capillaries from working to some extent. The comfort pressure range is approximately 1.96-3.92 kPa (14.7-29.4 mmHg), although this is also distinct according to individual preference differences, healing body parts differences, and therapy approaches differences. The compression garments exerted pressure should be well designed, as insufficient pressure cannot meet the therapy requirements or need

to extend therapy duration while surpassing pressure can cause discomfort, numbness, partial dysfunction, and even life-threatening injuries [10]. Besides external pressure, the user-friendly design of compression garments also involves biosafety, including air permeability, heat transmission, moisture transmission, tactile stimulation, biocompatibility, and even antibacterial and antivirus properties, especially for clinical purposes and during the COVID-19 pandemic situation.

Apart from medical usage, compression garments are popularly adopted in sportswear [11-13]. The purposes are to upgrade the athletic performance of speed or stamina on one hand, and on the other hand, to minimize possible injuries during training or competition, to improve remedy, and to accelerate recovery afterward [14]. In general, moderate pressure is broadly recommended, especially for amateur sports activities and individual fitness. Moreover, compression garments are considered appropriate for body shaping as suitable pressure is exerted on desired tightly fitting human body parts [15, 16].

Traditional commercial compression garments are widely used in chronic venous disease management, scar management, orthopedic application, body shaping application, sportswear application, and other applications. For all of these applications, pressure management is essential. However, traditional functional compression garments cannot provide accurate and real-time pressure measurement. Moreover, there have been several explorations on smart compression garments, which are single-functional, large, bulky, and not suitable for long-time wearables. Hence, the imperceptible, multifunctional, long-term used smart compression

garments are highly desirable as they can monitor the variation in pressure and offer information during therapy or even advice on how to enhance therapy efficacy.

There are huge academic gaps. According to the author's knowledge, there is no systematic research and implementation from scratch for smart compression garments to achieve real-time pressure management, which includes hardware design, software design, algorithm design, and clinical experiment design. Although there are several laboratory explorations on piezoresistive sensors, resistive stretch sensors, optical fiber sensors, and capacitive pressure sensors, nonetheless, the academic work has never in-depth investigated the unified framework of hardware design, software design, algorithm design, clinical experiment design for smart compression garment systems and deployment for multitasks scenarios. With the fast development of textile flexible sensors, the sensors still have complex responsive functions and are susceptible to dynamic surroundings, leading to worse performance of conventional signal processing approaches and highly demanding new signal processing approaches to do noise reduction. Thanks to deep learning, transferring learning, and edge computing, it is possible to propose a unified algorithm architecture to complete various tasks with high accuracy and adaptiveness. Applying smart compression garment systems to healthcare is precious and challenging. To focus on monitoring lower extremities muscles which are essential for daily activities such as maintaining posture, walking, and executing dynamic movements, the conventional methods seldom touched in vivo nor achieved high long-term usage conformity. The smart compression garment systems are plausible new solutions and lack clinical experiment evidence.

1.2. Objectives

For the sake of realizing a smart compression garment, it should be considered to use compression garments, embedded flexible sensors, edge control units, user interactive devices, and software applications. The components are all available off-the-shelf, commonly used, lower cost. The whole system has the advantages of high sensitivity to pressure, mechanical flexibility, modular design, configurable hardware and software. The specific objectives are listed as follows:

(1) To select components, design and make prototypes of smart compression garment systems, including compression garments, textile capacitive sensors, edge control units, user interactive devices, software applications, and cloud backend. To design and implement laboratory user experience tests and clinical experiments for purposes of evaluating the overall performance of the smart compression garment systems and accordingly iteratively improving relevant hardware and software design.

(2) To optimize the textile capacitive sensors, achieving high sensitivity in the low-pressure range and good conformity to curved surfaces. To calibrate laboratory fabricated textile capacitive sensors for long-term use regarding flat surface pressure measurements and different curvature surface pressure measurements respectively.

(3) In-depth analysis of the signal processing methods and propose a new unified solution architecture to denoise for frequency overlap and non-stationary noise concerning laboratory-fabricated flexible sensors. To iteratively optimize the algorithms, based on the established flat surface pressure dataset and curve surface pressure dataset.

(4) To investigate the application of monitoring skeletal muscle force of lower extremities, design, and complete comprehensive clinical experiments through healthy participants to perform maximum voluntary isometric contraction of ankle plantarflexion, and statistical analysis to achieve convincible conclusions.

1.3. Methodology

To accomplish the aforementioned objectives, it is imperative to define the research methodology for this project through a comprehensive review aimed at identifying various requirements of different compression garment applications and an in-depth study of signal processing methods to find out the potential directions of a new desired signal processing method for the smart compression garment. Then hardware and software design and implementation are completed, to evaluate the final performance. Healthcare applications are investigated and desired clinical experiments are designed and analyzed elaborately. In this section, detailed methodologies are illustrated below, including the main techniques for system architecture design, electronic devices design, mobile device software design, signal processing design, performance evaluation, clinical experiment design, and data analysis.

(1) A comprehensive review is conducted on different compression garments and compression therapies, focusing on chronic venous disease management, scar management, orthopedic application, body shaping application, sportswear application, and other applications. It is identified for the research gap between current compression garments and desired smart functional garments requirements.

(2) Different signal processing methods and noise reduction methods are summarized and investigated in depth, to deal with flexible sensors induced frequency overlap and non-stationary noise issues. This forms guidelines to cope with diverse compression garments application scenarios. Moreover, deep learning and transferring methods are investigated, to achieve unified deep learning based algorithms to deal with noise reduction and downstream multiple tasks.

(3) Literature review concentrates on compression garment systems applications for healthcare, furthermore muscle force generation mechanism, the importance of monitoring lower extremities muscle force, current popular methods to detect the muscle force and their limitations. This highlights the worth and urgency of applying the smart compression garment systems.

(4) According to the smart compression garments research gap, hardware and software architecture is determined and designed. The architecture can utilize off-the-shelf and lower-

cost components and commonly used facility tools or platforms so that the architecture takes advantage of low cost, flexibility, user-friendliness, easy external systems integration, rapid upgrade and repair, easy adaptation to various application scenarios.

(5) Based on deep learning methods, new signal processing is researched and proposed. Focusing on pressure management of medical compression stockings, unsupervised deep learning based encoder-decoder algorithms are proposed to do noise reduction, to improve the resolution and precision of pressure calculation for flexible capacitive pressure sensors. In the laboratory, the flat surface and curved surface pressure experiments are designed and implemented through a laboratory horizontal flat platform, constant standard normal weights, one medium-sized wooden mannequin leg, and one commercial sphygmomanometer, datasets are established respectively and analyzed about their distribution to reflect the characteristics of fabric sandwich-structured pressure sensors. The performance of the algorithms is evaluated based on these datasets and compared with the benchmark of traditional polynomial regression models.

(6) To continuously monitor lower extremities muscles, traditional assessment methods, like electromyography and physiological cross-sectional area measurements, often struggle to provide precise real-time data while ensuring user comfort and practicality in both clinical and community settings. The smart compression stocking system is upgraded accordingly. Then design and implementation of a clinical study on the relationship between measured pressure changes and generated gastrocnemius muscle force measured by Humac NORM, involving

healthy young individuals to perform maximum voluntary isometric contraction of ankle plantarflexion. Statistical analysis is used on the obtained dataset to test the hypothesis of a positive linear correlation and evaluate the efficacy of subject samples.

1.4. Research Significance

The primary contribution of this research lies in the comprehensive examination of smart compression garments from a systemic perspective. The novelty of this work can be attributed to the following key aspects:

(1) In-depth investigation of characteristics of fabric capacitive pressure sensors. The sensors' responses were analyzed regarding short-term continuous flat surface pressure, long-term curve surface pressure, and different curvature surface pressure, considering current textile flexible sensors are highly susceptible to deformation on curved surfaces and fluctuation along the timeline.

(2) The new unified signal processing architecture, i.e. encoder-decoder architecture, was proposed, which takes advantage of high compatibility, high interpretability, inter-changeable modules, and easy application to downstream multi-tasks.

(3) Deep learning neural networks were adopted, transferring the paradigm from complicated data processing algorithms to general deep learning approaches, which can save plenty of

intensive labor on deriving close expressions of formulas and improve accuracy by a large margin.

(4) The unified infrastructure system, including hardware, software, and user interface, was designed and implemented. User-centered evaluation was conducted. Different compression garment applications validated the effectiveness of the proposed architecture.

(5) A clinical study to monitor skeletal muscle force of lower extremities. This is significant because lower extremities muscles are essential for basic human daily activities, but conventional methods seldom touched in vivo nor achieved high long-term usage conformity.

(6) Proposed system integration, signal processing, and applications of smart compression garment systems have merits of low cost, simple design, the capability of mass production, and sustaining large scale of practical use.

This research involves smart textiles, electronics engineering, computer science, artificial intelligence, and medical research, which would underscore the importance and value of facilitating Interdisciplinary Research, inspire new findings and developments, and stimulate more end-to-end architecture design and implementation of smart wearable systems. It is expected this research will demonstrate the value of the smart compression garment system with compression garments, embedded flexible fabric-based sensors, edge control units, user

interactive devices, software applications, and cloud backend, and accelerate the application of the smart compression garment system on human healthcare activities monitoring.

1.5. Outlines of the Thesis

The thesis regarding smart compression garments is presented in six chapters, with the main contents briefing in Figure 1-1.

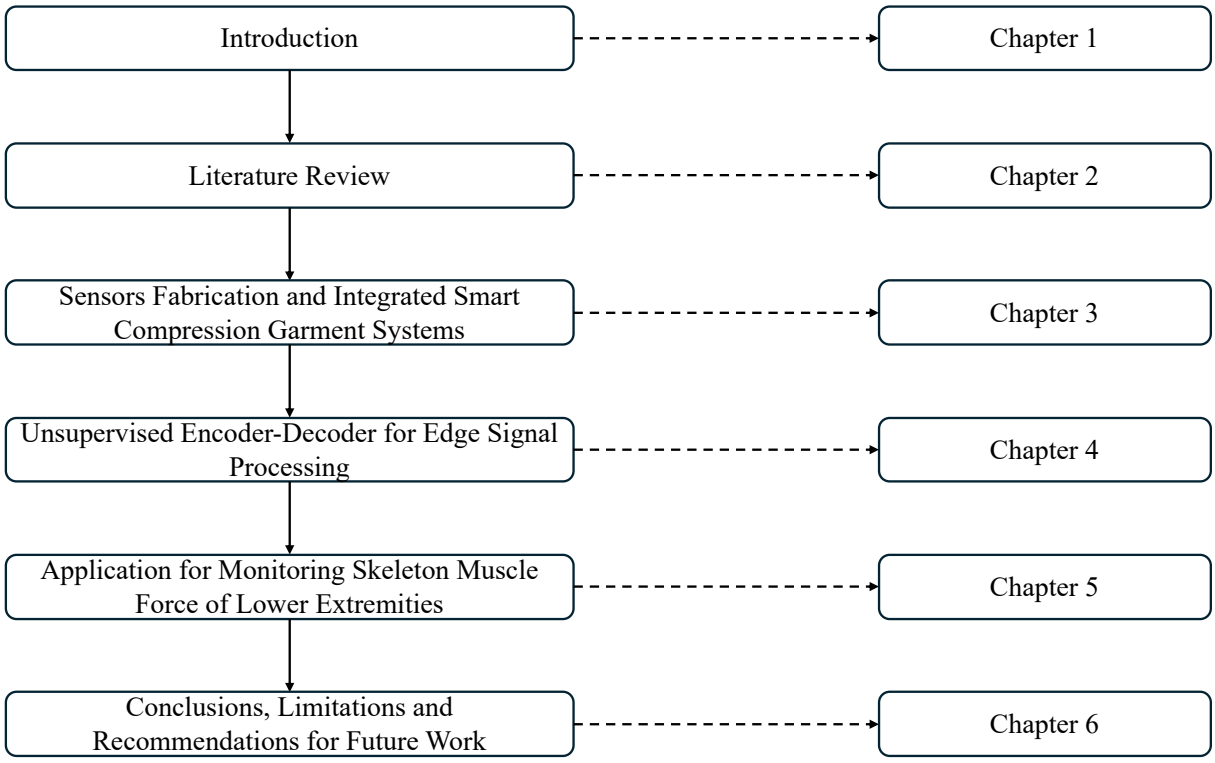

Figure 1-1 Thesis structure illustration.

Chapter 1 serves as the introduction to this study, encompassing essential elements such as the project background, identified problems, project objectives, and adopted research methodology.

This chapter provides a comprehensive overview of the study's context, outlining the research questions and aims while delineating the chosen approach for conducting the research.

Chapter 2 presents a comprehensive literature review that encompasses the relevant topics explored in this thesis. It covers various compression garments and compression therapies, with different application requirements. Signal processing methods are systemically investigated to cope with diverse compression garment application scenarios. Furthermore, it reviews the mechanism of muscle contraction and current monitoring technology to monitor skeletal muscles' contraction.

Chapter 3 explains in detail new smart compression garment systems, including compression garments, embedded flexible sensors, edge control units, user interactive devices, and software applications. Wireless communication protocol selection and hardware cost are discussed.
It also describes the preparation work of fabric-based sensors, including textile capacitive pressure sensor fabrication, basic performance testing, and sensor module design.

Chapter 4 reveals the end-to-end deep learning algorithms. To cope with flexible sensors-induced noise issues, the unsupervised encoder-decoder architecture is introduced for different downstream tasks. For the collected flat surface pressure dataset, the algorithm gains a 38% increase in accuracy from that obtained by traditional polynomial regression. For collected curve surface pressure datasets, the algorithms gain 98%, 97%, 98% increase accuracy from

that obtained by traditional polynomial regression for the B position, B1 position, C position respectively.

Chapter 5 introduces a clinical study of the relationship between measured pressure change and generated gastrocnemius muscle force, involving 12 healthy young individuals to perform maximum voluntary isometric contraction of ankle plantarflexion; the identified linear relationship between measured pressure changes and generated gastrocnemius muscle force enables monitoring the muscle force of the lower extremities in isometric mode.

Chapter 6 serves as a summary of the principal findings derived from this research endeavor. In addition, this chapter addresses the limitations inherent in the study and offers insightful recommendations for future research endeavors related to hardware upgrades, signal processing upgrades, and potential MetaHealth applications. By consolidating the key outcomes of the research, acknowledging its constraints, and proposing avenues for further exploration, Chapter 6 contributes to the overall understanding of the research's significance and paves the way for future advancements in the field.

Chapter 2 Literature Review

2.1. Introduction

This chapter introduces the background and process of designing a smart medical compression stocking system. Compression garments are widely used in chronic venous disease management, scar management, orthopedic application, body shaping application, sportswear application, and other applications. However, traditional functional compression garments cannot provide accurate and real-time pressure measurement. In addition, for the functional compression garment with different wearable sensors and sensing networks, signal processing is the vital stage to determine how successful the whole wearable system is. This chapter discusses mainly basic concepts, classic theories, general dealing techniques, emerging issues, and recommendations so that it is convenient to apply to practice accordingly. Furthermore, continuous monitoring of lower extremity muscle function is crucial due to the essential role these muscles play in daily activities such as maintaining posture, walking, and executing dynamic movements. Traditional assessment methods, like electromyography and physiological cross-sectional area measurements, often struggle to provide precise real-time data while ensuring user comfort and practicality in both clinical and community settings. Hence it is highly valuable to design a novel smart compression garment system.

Section 2.2 describes the history of compression therapies and compression garments. Section 2.3 in detail illustrates traditional commercial compression garments applied in chronic venous disease management, scar management, orthopedic application, body shaping application, sportswear application, and other applications, and the research gap is highlighted. Section 2.4 discusses the signal processing for wearable systems. Section 2.4.1 describes preprocessing methods, including amplifying, denoising, filtering, sampling, quantization, and analog-to-digital (A/D) conversion. Sections 2.4.2 and 2.4.3 describe classic mainstream signal processing methods, i.e. deterministic signal processing and stochastic signal processing. Section 2.4.4 describes several advanced signal processing methods, such as stochastic process, wavelet transform. Section 2.4.5 describes several popular data science processing methods, such as machine learning, deep learning. Section 2.5 introduces the importance of the gastrocnemius muscle for human daily activities, the mechanism of muscles' contraction, and current technologies to monitor skeletal muscles' contraction including the electromyography (EMG) methods and physiological cross-sectional area (PCSA) methods and their limitations. Section 2.6 briefly provides a summary.

2.2. Compression Garment Introduction

Various functional garments are widely used and attract more and more attention; among them, compression garments are one broad unique functional category. Currently, commercialized off-the-shelf compression garments utilize elastomeric fibers and yarns and well-designed fabric structures to generate appropriate mechanical pressure, so that contact human skins and

underlying tissues are supported, stabilized, compressed, and strained. Furthermore, transmitting pressure from the surface to the internal is beneficial for skin healing, blood circulation, lymph circulation, and capillary reabsorption. Therefore, compression garments are generally recommended for medical curing applications, athletic applications, body shaping applications, and geriatric healthcare applications [1-4].

In retrospect along the historical timeline, Hippocrates of Kos, who was a Greek physician during the Age of Pericles and renowned as the “Father of Medicine”, mentioned the compression therapy, which utilized externally exerted pressure to fix the posture of wounded lower extremities resisting against natural gravity for better healing. Other invented devices could also benefit this healing according to various wounded parts [5]. In 1628, William Harvey studied the relationship between venous stasis and external pressure, which prompted later on emerging kinds of compression therapy methods, such as laced stocking, elastic bands, tight bandage with resin, cellulose fiber stocking, chemical fiber stocking (acrylic, nylon, polyester) [6]. Not until the 19th century when mass production of commercial bandages came up and was wildly used in clinical trials, compression therapy became much more popular and effective. In the meantime, compression stockings with elastomer yarns were first introduced to produce graduated compression distribution [7, 8]. After that, in the 20th century compression therapy was used to cure burned skin to accelerate scar formation and alleviate hypertrophic scars [9].

To achieve high performance of effective and efficient healing, several characteristics of compression garments are highlighted and set higher priorities, such as graduated compression

distribution (higher pressure at the ankle and lower pressure at the thigh), pressure gradient distribution (avoiding partially reverse pressure gradients), stability, flexibility, duration, biosafety. It was studied that the discomfort pressure range is approximately 5.88-9.80 kPa (44.1-73.5 mmHg), although there is variation according to individual preference difference, healing body parts difference, therapy approaches difference, which however is indicated as a little more than the average blood pressure in capillaries close to the skin surface of approximate 4.30 kPa (32.3 mmHg). High external pressure might obstruct capillaries from working to some extent. The comfort pressure range is approximately 1.96-3.92 kPa (14.7-29.4 mmHg), although there is also variation according to individual preference difference, healing body parts difference, and therapy approaches difference. The compression garments exerted pressure should be well designed, as insufficient pressure cannot meet the therapy requirements or need to extend therapy duration while surpassing pressure can cause discomfort, numbness, partial dysfunction, and even life-threatening injuries [10]. Besides external pressure, the user-friendly design of compression garments should also consider biosafety, including air permeability, heat transmission, moisture transmission, tactile stimulation, biocompatibility, even antibacterial and antivirus properties, especially for clinical purposes and during the pandemic situation.

Apart from medical usage, compression garments are popularly adopted in sportswear [11-13]. The purposes are to upgrade the athletic performance of speed or stamina on one hand, and on the other hand, to minimize possible injuries during training or competition, to improve remedy, and to accelerate recovery afterward [14]. In general, moderate pressure is broadly recommended, especially for amateur sports activities and individual fitness. Moreover,

compression garments are considered appropriate for body shaping as suitable pressure is exerted on desired tightly fitting human body parts [15, 16].

2.3. General Functional Compression Garment

2.3.1. Chronic venous disease management

Chronic Venous Disease (CVD), also known as Chronic Venous Insufficiency (CVI), is a debilitating condition where a severe pooling of blood in the veins slows down or hampers the return of blood to the heart, with a general prevalence between 60-70% [17]. CVD is regarded as the most prevalent venous disorder in the veins of the lower extremities, which heavily negatively impacts 5% to 30% adult population health status in the world [18]. This disease is more common at older age and more dominant in females [19]. The pathophysiology is complicated and not so obvious, involving individual genetic susceptibility, personal and environmental influential factors, including age, gender, pregnancy, obesity, deep and superficial vein thrombosis, phlebitis, May-Thurner compressions, sedentary lifestyle, occupation, smoking, long-term inactivity, prolonged standing or sitting, previous leg injuries [20-23]. The consequential symptoms consist of partial pain, telangiectasias, reticular veins, varicose veins, swelling, edema, pigmentation, dermal irritation, eczema, lipodermatosclerosis, and venous ulcer [24].

Patients' primary venous valvular incompetence and congenital vein wall weakness can cause a sequence of reflux of the venous valves of superficial veins, venous hypertension, and then

inflammation which is an evident clinical indication [25, 26]. Compression therapy is introduced at large as a conservative treatment or palliative care with minimal side effects for the sake of ameliorating venous insufficiency. Externally exerted pressure counterbalances patients' internal pressure distribution disorder, so that implementing gradually decreased pressure from ankles to thighs smooths blood flow in veins to normal status, increases the speed of blood flowback, reduces venous wall distention and hypertension, restores venous valvular functions, escalate capillary reabsorption, enhances hemodynamics and lymphatic circulation, deactivates inflammation, alleviates clinical signs such as swollen limbs and edema, despite that more severe chronic symptoms need specific surgical operations.

Compression therapy generally utilizes various compression garments, such as medical compression stockings (MCSs) or compression bandages. For theoretical analysis, one approach is to apply Pascal's Law and form an evenly distributed pressure enclosed system where pressure leads to decreased vein diameter, push back valve orientation, and smooths blood flow [27]. Another approach is to apply Laplace's Law and form a graduated distributed pressure garment, where different geometrical shapes of lower extremities are taken into account [28].

In general, mild symptoms patients are recommended to use lower pressure MCS by therapists while severe symptoms need higher pressure. Slight venous insufficiency patients can wear MCSs exerting ankle pressure of 10-20 mmHg. Varicose veins patients need MCSs providing 20-30 mmHg pressure. Active ulcers need 30-40 mmHg pressure. More severe symptoms like

lymphedema need 40-50 mmHg pressure and even higher [29]. Insufficient lower pressure or surplus higher pressure are both invalid and sometimes may cause negative effects [30]. Long time wearing MCSs is beneficial for soothing symptoms, taking effect from at least four to six months. It is recommended for continuous wearing until the necessity of temporary taking off, such as bathing and sleeping.

Compression bandages are another widely adopted approach, taking account of low cost, simple usage, and stable pressure. The pressure exerted by compression bandages can be classified as mild when less than 20 mmHg pressure, medium during between 20 to 40 mmHg pressure, strong during between 40 to 60 mmHg pressure, and very strong when greater than 60 mmHg pressure [31]. Pressure between 35 to 45 mmHg when wearing at ankle positions is practically appropriate and clinically effective [31, 32]. Considering safety reasons and side effects of lower stretchable bandages, 30 mmHg pressure exerted at upper extremities is the upper limit, while pressure between 50 to 60 mmHg at lower extremities is the upper limit [33]. For patients with ambulatory venous hypertension and intermittent venous occlusion, a pressure of greater than 50 mmHg is acceptable, which produces intermittent high-pressure peaks during patients' lower extremities movement working as massage effect and are attuned by multilayer lower stretchable bandages rather than elastic ones [34, 35]. Furthermore, some novel compression bandages can produce the desired pressure between 30 to 35 mmHg independent of distinct patient limb shapes and sizes [8].

2.3.2. Scar management

Skin dermal injuries and even severe skin burn injuries can cause a variety of skin complicated diseases, such as a hypertrophic scar, and corresponding complicated symptoms such as pruritus, erythema, pain, and articular stiffness by scar contracture under the condition of a nearby joint. All of these explicitly or implicitly lead to skin functional damage, or physiological, psychological, and aesthetic problems [36]. To improve the quality of patient's life, compression garments were introduced in the 1970s. They were adopted for treatment or prophylaxis avoiding hypertrophic scars. Although there is a lack of substantial supportive evidence to clearly explain the relevant mechanism, the probable explanation is that pressure by compression garments hinders collagen formation, promotes collagen lysis, increases cell apoptosis, decreases blood flow, and reduces oxygen supply near the scar tissues [37, 38]. Thus, compression garments are required a long time to wear. A typical solution is 23 hours for each day and continuous for at least one year until scars grow mature. Pressure between 20 to 30 mmHg is regarded as appropriate [39, 40]. Compression garments can be used for 2 to 3 months before being changed to a new one because they naturally diminish elasticity over time [41-43]. Some common disadvantages of compression garments include limited usage, skin discomfort, and undesired pressure. Compression garments cannot generate the desired pressure for flat or concave scar areas. For practical purposes, additional padding or face masks are inserted between these contact interfaces [44-46].

2.3.3. Orthopedic application

Compression garments are also widely for orthopedic supporting purposes, such as back supports, lumbar supports, calf supports, shoulder braces, elbow braces, and ankle braces [47]

[47]. Their utilities can be classified into preventive support, functional support, and rehabilitative support, which is recommended by physicians or adopted by deliberate users. Although there is no common standard to guide, available compression garments can be customized to some extent to satisfy self-comfort and desired supporting forces [48]. The compression garments are beneficial for paraplegic patients, motor disability patients, children, old people, and pregnant women, to produce anatomical correction, enforce body functional strength, and even improve motor functions [49]. It is not necessary to wear for a long period to provide supportive forces, especially for temporal dysfunctional patients, such as pregnant women and incorrect posture juveniles. Apart from the main parts of knitted elastic fabric, functional supportive compression garments generally have a solid frame made of silicone or metallic material and extra components of straps, fasteners, hinges, so that elasticity can be adaptive and supportive forces can be adjustable [50].

2.3.4. Body shaping application

Compression garments are also used to shape specific body parts for aesthetic purposes [15]. Traditionally a girdle is regularly worn by young women to uplift the hip and tighten the abdomen, which is regarded as a gorgeous body figure. Girdles can provide light, medium, or firm levels of support, while the firmer stands for girdles with tighter and multiple layers of fabrics, nevertheless avoiding discomfort or physiological damage. Thus, exerted pressure level is highly concerned, when applying to mainly ten anatomic positions, such as left side, right side, left front tummy, right front tummy, front tummy, left front lower, right front lower, left hips, right hips, waist. People prefer a higher pressure of approximately 11.5 mmHg at two

body sides, a lower pressure of approximately 4.5 mmHg at the hip, medium pressure of approximately 6.5 mmHg at the waist, which indicates an overall average pressure of approximately 7.5 mmHg [51]. If the pressure increases greater than 30-40 mmHg, users will feel somehow uncomfortable [52]. Thus, befitting girdles involves material, garment size, design patterns, and construction, as well as users' factors such as body size, anatomic positions, bone structure, and muscle resilience.

2.3.5. Sportswear application

A variety of compression garments are widely applied as functional sportswear to enhance performance or accelerate recovery speed, including compression shirts, compression sleeves, and compression underwear, On one hand, compression garments can generate proper pressure to improve blood flow, which can provide more oxygen, more energy, fast discharging metabolite, such as lactate, on the other hand, tight garments with smooth outside surfaces can largely cut down fluid resistance during fierce athletic competitions [4]. Furthermore, compression sportswear fixes muscle disturbance displacement, spurring neurotransmission, and enhancing body mechanical capability [12]. For instance, compression sportswear can improve flexion and extension torque ranges and hamstrings controlling the legs [53]. Despite advantages during training or competitions, they are validated as helpful for post-exercise recovery by degrading muscle soreness, swelling, pains, and trauma rapidly in the short term and efficiently regaining muscle forces in the long term [54-57]. In addition, sportswear benefits athletes' psychological status during or after exercise [58, 59]. However, evidence of compression sportswear in certain high-intensity exercises is still elusive [60].

Researches on the effective pressure of compression sportswear attract much attention. It is useful for venous circulation if pressure is set lower than approximately 7.5 mmHg at trunk positions. If pressure is greater than approximately 8.6 mmHg at the chest position, corresponding pressure at the waist is measured as more than approximately 2.7 mmHg, however, it leads to the discomfort of swimmers, if pressure exceeds approximately 4.2 mmHg at the abdomen position [61]. Similarly, higher pressure at the shoulders or inguinal positions causes skin blood suppressed and flown to peripheral areas, latency periods of blood pressure recovery after exercise, which is exceptionally detrimental for long-term rehearsal activities [62].

2.3.6. Other applications

Compression garments have found utility as maternity wear, wherein a specific type known as a bellyband, wrap, or abdominal binder is commonly employed. These garments share similarities with tube tops in terms of their design and functionality. However, it is specifically designed to be worn over the abdomen of pregnant women [63] [63]. These garments are frequently utilized during the postpartum period as well, serving the purpose of offering support to the abdominal and back regions. By doing so, they enhance the ease of performing daily activities and contribute to improved posture for mothers.

Compression garments are believed to bring positive influence, especially for the elderly, such as improved appearance of limbs, decreased symptoms of depression, better sleep qualities,

increased activity levels, enhanced muscle force, gained balance control, and strengthened proprioception [64-68].

Table 2-1 Overview of Therapeutic Applications and Suggested Pressure Levels for Compression Garments Across Various Conditions

Application	Condition/Use	Suggested Pressure Levels (mmHg)	Notes
Chronic Venous Disease Management	MCSs (Mild Symptoms)	10–20	Recommended for slight venous insufficiency.
	MCSs (Varicose Veins)	20–30	Suitable for patients with varicose veins.
	MCSs (Active Ulcers)	30–40	Required for managing active ulcers.
	MCSs (Severe Symptoms)	40–50 or higher	Necessary for more severe symptoms such as lymphedema.
	Compression Bandages (Mild)	<20	Economical and easy to use, providing stable pressure.
	Compression Bandages (Medium)	20–40	Provides moderate pressure for therapeutic purposes.
	Compression Bandages (Strong)	40–60	Suitable for strong compression needs.
	Compression Bandages (Very Strong)	>60	Applicable for conditions like ambulatory venous hypertension and intermittent venous occlusion.
	Ankle Position	35–45	Clinically effective pressure range for compression bandages at the ankle.
	Upper Extremities	≤30	Maximum safe pressure for upper extremities.
	Lower Extremities	50–60	Maximum safe pressure for lower extremities.
Scar Management	Hypertrophic Scars	20–30	Pressure aids in reducing collagen formation and blood flow near scar tissue. Recommended for 23 hours daily for at least one year. Garments should be replaced every 2 to 3 months due to loss of elasticity.
Orthopedic Application	Supportive Garments	Customizable	Used for preventive, functional, and rehabilitative support. Includes back, lumbar, and joint supports. Elasticity and supportive forces are adjustable, often incorporating solid frames and additional components.
Body Shaping Application	Girdles	4.5–11.5	Utilized for aesthetic body shaping. Higher pressure (~11.5 mmHg) at body sides, lower (~4.5 mmHg) at hips, medium (~6.5 mmHg) at waist. Overall average pressure ~7.5 mmHg. Discomfort may occur if pressure exceeds 30-40 mmHg.
Sportswear Application	Functional Sportswear	<7.5 (trunk), >8.6 (chest)	Enhances athletic performance and recovery. Improves blood flow and reduces fluid resistance. Pressure >4.2 mmHg at the abdomen may cause discomfort. Higher pressure at shoulders/inguinal areas can be detrimental.
Other Applications	Maternity Wear	N/A	Includes bellybands and abdominal binders. Provides support to the abdominal and back regions, improving posture and facilitating daily activities for mothers.
	Elderly Benefits	N/A	Enhances limb appearance, reduces depression symptoms, improves sleep quality, increases activity levels, and strengthens muscle force, balance control, and proprioception.

Table 2-1 provides a comprehensive summary of the functions, recommended pressure levels, and additional notes for the use of compression garments in managing chronic venous disease, scar management, orthopedic support, body shaping, sportswear, and other applications.

2.3.7. Challenges of traditional compression garments

Traditional commercial compression garments are widely used in chronic venous disease management, scar management, orthopedic application, body shaping application, sportswear application, and other applications. For all these applications, pressure management is essential. However, traditional functional compression garments cannot provide accurate and real-time pressure measurement. Furthermore, the users cannot receive simultaneous feedback whether in danger out of maloperation or are recommended to continue out of desired movements or postures. Moreover, although traditional functional compression therapy is adopted, patient or user compliance and follow-up care are still challenging. On the other hand, it is highly worth digitalizing patients' or users' daily life health status and realizing teleconsultation which is believed to be the future trend to at large reduce the workload burden and cost of current healthcare systems.

Hence there are huge academic gaps. According to the author's knowledge, there is no systematic research and implementation from scratch for smart compression garments to achieve real-time pressure management, which includes hardware design, software design, and algorithm design. Although there are several laboratory explorations, such as piezoresistive sensors [69-72], resistive stretch sensors [73], optical fiber sensors [74, 75], and capacitive

pressure sensors [76], nonetheless, academic work has never been in-depth investigated the unified framework of hardware and software design for smart compression garment systems and deployment for multitasks scenarios. Due to the fast development of textile flexible sensors, there is lacking systematic review and research of signal processing methods to deal with these sensors. The sensors have complex responsive functions and are susceptible to electromagnetic interference, proximity effects, and deformation on curved surfaces, leading to worse performance by conventional signal processing approaches and requiring new signal processing approaches. Finally, total cost-effectiveness and adaptive utility are seldom researched, which impedes the use of smart compression garments at large scale.

2.4. Wearable Sensors for Pressure Measurement

2.4.1. Different pressure sensors

Smart compression garments need wearable sensors to detect static pressure and dynamic pressure. Static pressure measurement should cover the range of 0 to 50 mmHg [77]. Dynamic pressure is involved, considering the users' activities and exercises, which cause the deformation of muscle or tendons, positions on human bodies changes, and furthermore, lead to pressure distribution change. Relatively high sensitivity in the low-pressure range below 50 mmHg, stable continuous output, resilience to temperature impact and humidity impact, small size and thinness, high flexibility, and conformation on the curve surface are all desired characteristics.

Piezoelectric sensors [78] and triboelectric sensors [79, 80] are popular research topics since they are self-powered devices and beneficial to carbon neutrality. Nevertheless, their work mechanism relies on the dynamic movement stimuli of repeated pressure exerted and removed to generate transient signals and output voltage signals drift over the longer time static pressure. Hence, they are suitable for dynamic pressure measurement.

Optical sensors, piezoresistive sensors, and capacitive sensors can accommodate static pressure measurement and dynamic pressure measurement. Optical sensors [81, 82] possess the benefits of high measurement accuracy, high sensitivity, good resolution, and resistance to surrounding electromagnetic fields' impact. They need complex system design, including light emitter device, light receiver device, and complicated configuration, which means larger sizes of devices, higher cost, higher power consumption, and difficulties in integrating, repairing, and upgrading. The optical fibers, as light transmittance media, are susceptible to holder deformation, fragile, and easy to cause light leakage and light pollution.

Piezoresistive sensors can be one of the candidates for wearable pressure measurement sensors, with the advantages of simple fabrication, low cost, flexibility, and dexterous appliances. They commonly adopt two electrodes and a piezoresistive layer in between, to form a sandwich structure. Embedding conductive materials with microporous structure and optimized microstructure surface could obliviously increment sensors' sensitivity [83-85]. Micro-semicylinders are more effective in polydimethylsiloxane (PDMS) conductive film resistive pressure sensors [86]. Micropores are another way to design microstructure to raise sensitivity

[87]. Different microstructure substrate materials were studied effectively, including paper [88], textile [89], and plants [90]. However, temperature change susceptibility, limited sensitivity in the low-pressure range below 50 mmHg, thickness, high hysteresis, and non-linearity in larger range hamper the piezoresistive sensors' wearable applications [91-94].

Capacitive sensors represent a particularly advantageous technology for wearable pressure sensing applications, offering superior performance characteristics including enhanced sensitivity, minimal power requirements, extended operational stability, exceptional mechanical durability, reduced hysteresis effects, and rapid response times. The fundamental structure employs a parallel-plate capacitor configuration consisting of two conductive electrodes separated by an intermediate dielectric material, creating a sandwich-type structure where applied pressure modulates the inter-electrode distance and consequently alters the measurable capacitance. This transduction mechanism enables precise pressure quantification through capacitance variations while maintaining the mechanical flexibility essential for textile integration and comfortable wearable deployment. The capacitance can be derived as $C = \varepsilon_0 \varepsilon_r \frac{A}{d}$, where ε_0 is free space permittivity, ε_r is relative permittivity, A is the contact area of two parallel conductive plates, and d is the distance between the two plates. As ε_r, A, d are changed and influenced by exterior mechanical stimuli, the capacitance will change accordingly. Hence several approaches to increasing relative permittivity and dielectric deformation can improve sensors' sensitivity. Adding conductive fillers in the dielectric layer can increase the relative permittivity, such as carbon nanotubes, and metallic nanoparticles [95]. Making

micropores in low-modulus elastomers enlarges dielectric deformation under pressure and also increases the relative permittivity [96-100]. Making microstructures in the dielectric layer can lead to higher sensitivity and higher mechanical deformation, which can further reduce the response time and hysteresis issue caused by viscoelastic deformation. Microstructure studies involve micro-pyramids [101, 102], micro-domes [103], micro-pillar-array [104], micro-array [105, 106], rough interfaces [107-109] and others [110-112]. In summary, the comparison among these different pressure sensor types is illustrated in Table 2-2.

Table 2-2 Different pressure sensor types comparison.

Sensors Categories	**Classification**	**Characteristics**	**Distinctions**
Piezoelectric Sensors	Active Sensors	only suitable for dynamic measurement	self-powered, output drift over time under static pressure, transient output signal
Triboelectric Sensors	Active Sensors	only suitable for dynamic measurement	self-powered, output drift over time under static pressure, transient output signal
Piezoresistive Sensors	Passive Sensors	both static and dynamic monitoring	low sensitivity in low pressure range, temperature change impact, high hysteresis, non-linearity
Optical Sensors	Passive Sensors	both static and dynamic monitoring	high power consumption, complicated measure system
Capacitive Sensors	Passive Sensors	both static and dynamic monitoring	moderate or high sensitivity, high durability, low hysteresis, fast response speed

Recent advancements in flexible capacitive pressure sensors have focused on optimizing microstructures, utilizing novel materials, and improving overall structural design [113]. These innovations have significantly enhanced sensor sensitivity, broadened detection ranges, and improved performance under diverse pressure conditions.

The design and engineering of microstructural dielectric layers have been pivotal in improving capacitive sensors sensitivity and detection capabilities. For instance, cylindrical ladder microstructures introduced in 2023 achieved 3.9 times higher sensitivity (0.12 kPa^{-1}) compared to sensors without such structures [114]. Similarly, porous Ecoflex with aligned airgap structures, developed in 2022, demonstrated high sensitivity within the 20-100 kPa range and a low detection limit of 20 Pa [115]. The synergistic effect of the surface hemispherical microstructure and the internal porous structure supported high sensitivity of 3.15 kPa^{-1} and wide pressure range of 0-200 kPa in 2022 [116]. Micro-structured PDMS film embedded with a layer of multi-walled carbon nanotubes (MWCNT) as the micro-structured conductive electrode, published in 2021, can reach 1.3 kPa^{-1} in the pressure range of 0-100 Pa [117]. Advancements in 2024 included porous PDMS dielectric layers with hole arrays by laser ablation and sacrificial templates, achieving a sensitivity of 0.694 kPa^{-1} and a broad pressure response from 3 Pa to 200 kPa [118]. Other notable innovations include microstructured composite dielectric layers (MCDL) introduced in 2022, which extended the linear detection range to 0-1.3 MPa and has a sensitivity of 0.00397 kPa^{-1} in the 0-600 kPa linear range [119], and micro-pyramidal PDMS combined with three-dimensional vertical graphene (VG) electrodes, attaining exceptional sensitivity of up to 6.04 kPa^{-1} in the 0-1 kPa range [120]. In 2023, a porous PDMS elastomer featuring both pores and engineered grooves achieved 6-8 times higher sensitivity and excellent linearity within a 0-50 kPa range [121]. In the same year, the distinctive three-dimensional architecture of the spacer fabric, characterized by its polyester pile construction, was instrumental in achieving a pressure sensitivity of 0.04 kPa^{-1} [122].

The introduction of novel materials and composites has further driven capacitive sensors performance. For example, spiked nickel/polyimide composite nanofiber membranes developed in 2024 enhanced sensitivity to 4.04 MPa^{-1} under high pressure up to 1.5 MPa [123]. A dual microstructure composite dielectric made from PDMS/BaTiO3/SrTiO3, also introduced in 2024, achieved a sensitivity of 2.681 kPa^{-1} [124]. Biomimetic hibiscus flower-inspired microstructures coated with silver nanowires and an ionic gel film, presented in the same year, demonstrated ultrahigh sensitivity of 48.57 kPa^{-1} in the 0-1 kPa range [125]. Earlier, in 2022, researchers utilized ammonium bicarbonate (NH4HCO3) doped PDMS to create dielectrics with adjustable porosity, enabling pressure detection across a wide range (0-1200 kPa) [126]. Additionally, cost-effective polyurethane (PU) sheets, developed in 2025, provided highly deformable sensors with a sensitivity of 0.377 kPa^{-1} [127]. In 2024, utilizing a carboxyl iron particle-paraffin wax (CIP-PW)/silicone composite as the dielectric layer allows for temperature and magnetism-controlled tunable wide detection range of 0.2-350 kPa at the frequency range of 0-5 Hz [128].

Beyond microstructure design, advancements in overall sensor architecture have significantly improved performance. Kirigami-inspired conductive layers, introduced in 2024, enhanced sensitivity by approximately threefold and extended sensing distances by up to 170% compared to conventional designs [129]. Novel electrode shapes and configurations have also been explored, achieving a remarkable 79-fold improvement in sensitivity over traditional diaphragm-based pressure sensors of similar dimensions [130].

Table 2-3 Performance Metrics of Advanced Flexible Capacitive Pressure Sensors (2021-2025).

Sensor Type/Key Innovation	Year	Sensitivity (kPa^{-1} or MPa^{-1})	Pressure Range (kPa or MPa)	Response Time (ms)	Stability/Cycles	Detection Limit (Pa)	Key Application/Note	References
MWCNT electrodes, PDMS dielectric	2021	1.3 kPa^{-1}	0-100 Pa	Not specified	4000 cycles	Not specified	Arterial pulse, breathing monitoring	[117]
Cone-type MCDL	2022	3.97×10^{-3} kPa^{-1} (0-600 kPa)	0-1.3 MPa	Not specified	Not specified	Not specified	Wearable monitoring, spatial pressure sensing	[119]
Porous Ecoflex (aligned airgap)	2022	Not specified	20-100 kPa	~100	High operational stability	20	Electronic skin, wearable medical devices	[115]
PDMS with various porosity (NH_4HCO_3)	2022	Higher sensitivity	0-1200 kPa	Not specified	Not specified	Not specified	Human motion detection (fingerprint, joint, knee)	[126]
PDMS with hemispheric surface microstructure & porous internal structure	2022	3.15 kPa^{-1}	0-200 kPa	Not specified	Not specified	27	Robot skin, intelligent prosthetic hands	[116]
Cylindrical ladder microstructure	2023	0.12 kPa^{-1}	Not specified	Not specified	Not specified	Not specified	Rainfall frequency monitoring	[114]
Soft capacitive pressure sensor (spacer fabric)	2023	0.04 kPa^{-1}	Not specified	7 (recovery)	10000 cycles	Not specified	Human walking phase monitoring	[122]
VG electrode / micro-pyramidal PDMS	2023	6.04 kPa^{-1} (0-1 kPa), 0.69 kPa^{-1} (1-10 kPa)	0-10 kPa	Not specified	Not specified	Not specified	Finger joint, knee motion, facial expression	[120]
Porous PDMS elastomer (grooves)	2023	6-8x higher sensitivity	0-50 kPa	~50	Good linearity	3.5	Wearable devices (finger/wrist bending), object identification	[121]
Spiked Ni/PI composite nanofiber	2024	4.04 MPa^{-1}	1.5 MPa	30 (response) / 40 (recovery)	1000 cycles	Not specified	Human motion, sleeping posture, plantar pressure	[123]
Porous PDMS dielectric (hole array)	2024	0.694 kPa^{-1}(0-1 kPa)	0-200 kPa	96 (response) / 118 (recovery)	500 cycles	3	Human physiological activities	[118]
PDMS/$BaTiO_3$/$SrTiO_3$ composite	2024	2.681 kPa^{-1}	Not specified	39 (response) / 61 (release)	5000 cycles	Low detection threshold	Human pulse, heartbeat, robot arm sensing	[124]
Biomimetic hibiscus flower microstructures	2024	48.57 kPa^{-1} (0-1 kPa), 15.24 kPa^{-1} (1-30 kPa), 3.74 kPa^{-1} (30-120 kPa)	0-120 kPa	<58	Not specified	Not specified	Physiological signals, plantar pressure	[125]
(CIP-PW)/silicone composite	2024	0.011 kPa^{-1} (0-72 kPa, room temperature), 0.00619 kPa^{-1} (72-200 kPa, room temperature), 0.034 kPa^{-1} (0-24 kPa, 60 °C), 0.017 kPa^{-1} (24-80 kPa, 60 °C), 0.00891 kPa^{-1} (0-60 kPa, 300 mT), 0.002758 kPa^{-1} (60-400k kPa, 300 mT)	0.2-350 kPa	Not specified	Not specified	200	Human movements (finger, arm, and foot motions), wearable devices, e-skin, robotics, medical monitoring	[128]
PU layer (cost-effective)	2025	0.377358 kPa^{-1}	Not specified	Not specified	Not specified	Not specified	Affordable, simple, sustainable sensor	[127]

These innovations in microstructure design, material composition, and structural optimization collectively underscore the rapid progress in capacitive sensors technology, as summarized in the Table 2-3, paving the way for highly sensitive, versatile, and efficient pressure-sensing solutions.

2.4.2. Wearable pressure sensor selection criteria

[131] evaluated a silicon piezoresistive sensor-based portable pressure-monitoring device specifically designed for use with compression garments in the treatment of burn-induced hypertrophic scars. Their study demonstrated that maintaining a therapeutic pressure range of 15-25 mmHg significantly improved scar thickness and erythema, highlighting the clinical utility of pressure feedback in optimizing treatment outcomes. Similarly, [132] conducted a comparative assessment of two commercially available piezoresistive and capacitive pressure sensors embedded within compression apparel for athletes. Their findings underscored the potential of thin, flexible sensors to provide real-time compression data, thereby informing the iterative design of athletic garments that effectively balance performance and comfort. Despite these advancements, existing research has predominantly treated pressure sensors and garments as separate entities, lacking seamless integration for continuous, real-time, adaptive monitoring. Consequently, neither intermittent measurements nor post-hoc compensatory adjustments adequately capture dynamic changes in muscle force or environmental conditions.

Recent innovations in wearable technology have focused on enhancing the monitoring of physiological parameters through the integration of advanced sensors. One such development is presented by [133], which introduces a wearable arm-band incorporating stretchable fabric-strain sensors alongside surface electromyography electrodes. This system is designed to detect and predict biceps brachii fatigue during dynamic elbow flexion exercises. The proposed technology demonstrates robust performance in distinguishing between non-fatigued, onset,

and advanced fatigue phases, underscoring its potential for in-field monitoring of upper-limb muscle endurance. This capability is particularly valuable for athletes, clinicians, and ergonomics specialists seeking to optimize performance and prevent injury. In a related advancement, [134] describes the embedding of a melt-blown fiber pressure sensor within a standard breathing mask. This innovation captures minute variations in airflow pressure associated with inhalation and exhalation, achieving sub-Pascal resolution across multiple respiratory states. The system offers a noninvasive, wearable solution for monitoring breathing patterns, with applications in health screening and sleep apnea detection. Despite these promising developments, the studies face challenges related to overfitting risks and the lack of comprehensive wearable system design, integration, and improvement. Addressing these issues is crucial for advancing the practical application and reliability of such wearable technologies.

Therefore, to accurately and real-time measure static and dynamic pressure on compression garments is still challenging and needs more study. High sensitivity in the low-pressure range below 50 mmHg, rapid response speed, thinness, simpleness to be integrated with the compression garments, ease of connecting to the dedicated circuit board, resilience to surrounding interference, and conformation to the curved surface are significant driving factors in this thesis. Moreover, the cost of fabrication should be cut down to facilitate larger population usage. On one side, filler materials for wearable sensors should consider low cost, extensive use, and conveniently available materials. On the other side, making microstructures should also consider low cost, simple process, and easily standardized methods. Regarding textile capacitive pressure sensors, it is a feasible option to adopt filler materials of PDMS and mixed

carbon black (CB) powder to increment the relative permittivity and make microstructures through the rough process by abrasive papers to increment the relative permittivity and enlarge dielectric deformation under pressure [109].

2.5. Signal Processing for Wearable Systems

2.5.1. Signal preprocessing

2.5.1.1. signal conditioning

Different information sources always generate analog signals, which feature temporal and spatial continuity, and value continuity, such as human motion, health indicators, etc. [135-137] Wearable sensors or sensor networks convert all kinds of these analog signals into electric analog signals. Because of wearable sensors' output range limitation, components instability, and energy loss, worsened by ambient interference and noise, weak signals are commonly acquired, i.e. small voltage and small current. Hence, an amplifier module is commonly needed. Depending on applications, power amplifiers or amplitude amplifiers are chosen, where both have the advantages of low noise and high input impedance, thus reducing the impact of noise introduced by the amplifier itself and cutting off inverse impact caused by cascaded circuits.

For analog circuit design, different filters are added then, so that analog signals of interest are passed through while others are blocked. Conventionally there are low-pass, high-pass, and band-pass filters, fitting for different application purposes. Analog filter performance highly relies on stable electronic components. On the other hand, digital filters can be added after the

analog-to-digital converter (ADC) stage, replacing analog filters before the ADC stage. Digital filter design will be discussed later. The signal preprocessing is shown in Figure 2-1.

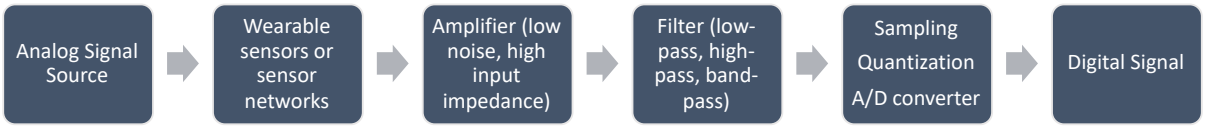

Figure 2-1 Schematic diagram of signal preprocessing system.

There are also other signal conditioning methods, such as rectifiers (half-wave, full-wave), envelope detectors, etc. depending on application purposes. Analog circuits have better energy consumption efficiency. However, it is an obvious trend that nowadays engineers put more effort into digital circuit design rather than analog circuit design pursuing stabilized output signals, simplified analysis, easy fault detection, and access to simulations.

2.5.1.2. sampling and quantization

Sampling represents reading analog signals' instantaneous values at predetermined time instances. For most cases, it is widely used for equally spaced time interval sampling rather than variant spaced time interval sampling. Moreover, spatial sampling means to read values at spatial intervals.

According to Shannon or Nyquist Theorem, if a signal is sampled (for an infinite period) at a sampling frequency fs (time intervals Ts = 1/fs) higher than double that of the highest frequency of interest (bandwidth), it can be ascertained no loss of information, which also means to

reconstruct a signal from its samples by using interpolation. Thus, it calls the non-distortion smallest sampling frequency as Nyquist rate, and one-half of sampling frequency (sample rate) as the Nyquist frequency, as shown in Figure 2-2. If the sampling frequency is not double higher of bandwidth of a signal, the information is distorted, referring to “aliasing”, which is called undersampling. For best practice, it is highly recommended to use a higher sampling frequency, such as 4 times instead of 2 times the bandwidth of a signal, which is called oversampling.

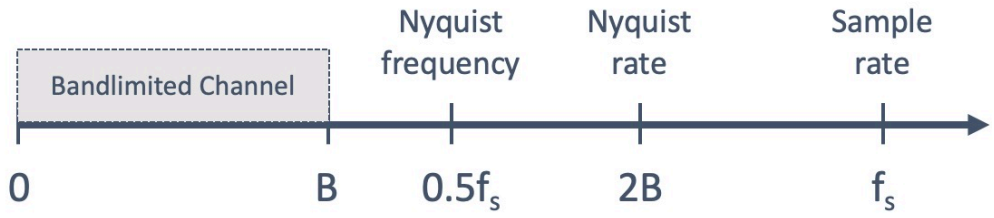

Figure 2-2 Relationship of Nyquist rate and frequency.

After sampling, a continuous signal is converted into a discrete sequence. Then quantization can map continuous infinite values to a predetermined smaller set of discrete finite values, as illustrated in Figure 2-3. Rounding and truncation are typical common techniques. A/D converters transform the sampled voltages or currents into different “levels” which can be represented in binary code. The total number of levels is calculated as 2^n-1, where n is the number of bits of converters, so that resolution can be derived (Resolution = Range/(2^n-1)), as explained in Table 2-4. In practice, resolution is determined at the beginning and then a specific ADC module can be determined.

After quantization, digital signals are generated. Unfortunately, the quantization process often introduces error noise. For most cases, this can be modeled as an additive white noise which is independent of input signals and has a flat power spectral density. Typically, input analog signal amplitude is much larger than ADC resolution, thus quantization error noise has an approximately uniform distribution, which has a mean of zero and the root mean square deviation of $\frac{1}{\sqrt{12}}Resolution \approx 0.289Resolution$ by utilizing the rounding technique, a non-zero mean of $0.5Resolution$ and the root mean square deviation of $\frac{1}{\sqrt{3}}Resolution \approx 0.577Resolution$ by utilizing truncation technique. While input analog signals commonly have a high amplitude and wide frequency spectrum, the potential signal-to-quantization-noise ratio (SQNR) can be derived as $SQNR = 20\log_{10}(2^n) \approx 6.02n\ dB$, assuming n bits ADC is used. For example, a 16-bit ADC has a potential SQNR of $16 \times 6.02 = 96.3\ dB$, which stands for a high-value ratio, hence quantization error noise can be omitted for simplifying analysis.

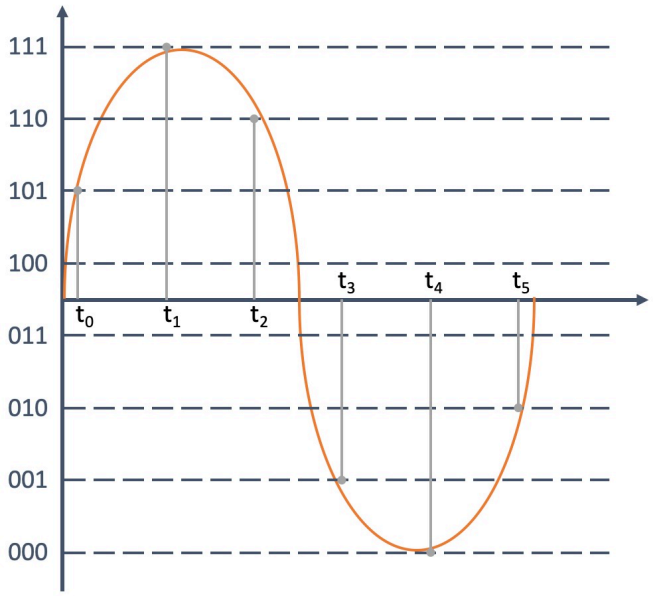

Figure 2-3 Illustration of sampling and quantization.

Table 2-4 Relationship of resolution and number of bits of ADC.

Number of bits (n bits ADC)	**Number of levels ($N = 2^n-1$)**	**Voltage Range (± 5 V)**	**Resolution (± 5 V input range)**
8	255	-5 V ~ +5 V	39.062 mV
10	1023	-5 V ~ +5 V	9.765 mV
12	4095	-5 V ~ +5 V	2.441 mV
14	16383	-5 V ~ +5 V	0.610 mV
16	65535	-5 V ~ +5 V	0.152 mV

2.5.1.3. analog-to-digital conversion

In a wearable system, a suitable analog-to-digital converter to complete A/D conversion should be determined, which converts an input analog voltage or current to a digital number representing the magnitude of the voltage or current. Generally, commercial ADC devices have functions of amplitude gain, denoise, sampling, and quantization.

The amplitude gain and ADC input range and resolution are comprehensively taken into account before determining ADC devices. For example, the desired resolution is predetermined as 1 μV/bit. Measuring the maximal peak-to-peak amplitude of input signals to get 60 mV, it is obtained the number of levels N (60 mV/1 μV = 60000) needed for quantization, and thus how many bits n is needed (here n = 16, because $2^{16} = 65535 > 60000$). In conclusion, 16 bits ADC with a 60 mV range and zero amplitude gain is sufficient, or 12 bits ADC with a 60 mV range and amplitude gain of 16 ($16 = 2^4$).

It is highly recommended that the resolution of ADC is somewhat lower than the noise level of the expected system and the range of ADC is somewhat larger than the expected maximum peak-to-peak amplitude of input analog signals. There is a trade-off between efficiency and accuracy.

For practical application, most detection signals are of low frequency, therefore sampling frequency is easily satisfactory. For example, if the purpose is to detect human physical motions that are generally lower than 20 Hz, thus the Nyquist rate is 40 Hz. The sampling frequency of 100 Hz is sufficient.

2.5.1.4. digital filter

There is plenty of noise, and unwanted disturbance in an electrical signal for any electronic system, which are generally classified into internal noise and external noise. Internal noise consists of thermal noise, shot noise, flicker noise, burst noise, etc. External noise consists of intermodulation noise, crosstalk, atmospheric interference, atmospheric background noise, etc. Noise cannot be eliminated but attenuated commonly by utilizing different filters, so that the signal-to-noise ratio is increased, and the signal of interest is strengthened.

If to detect human physical motions is desired, then a 20 Hz low-pass filter is implemented to attenuate high-frequency noise components. Otherwise, if other information except human physical motions is desired, then a high-pass filter with a cut-off frequency of 20 Hz is applied. Moreover, it is important for practice, a) it should be avoided to remove the bandwidth where

signals show very high, near maximum power density, b) filters are not perfect components, which means there is no 100% rigid cut-off and thus it is reasonable to choose 3 dB cut-off frequency to represent, there are residual unwanted signals, and it causes somewhat amplitude distortion and phase rotation of remaining signals.

A digital filter is widely used for its flexible design and simple analysis. There are typical two categories: infinite impulse response (IIR) filter and finite impulse response (FIR) filter, correspondingly the recursive filter and the non-recursive filter. For FIR filter design, a proper window function can be chosen from these candidates: rectangular window, triangular window, sine window, flat top window, Gaussian window, Welch window, Tukey window, Hann window, Hamming window, Blackman window, Kaiser window, etc. For IIR filter design, it can be completed by inheriting from these candidates: Chebyshev filter, Butterworth filter, and elliptic filter.

2.5.1.5. denoise

Besides a variety of filters, other practical denoise techniques are applied. For example, regarding wearable EMG systems [136, 137], in the EMG band (10-500 Hz), some sensors output voltage noise lower than 1 μV_{RMS} and corresponding to approximately 4-6 μV_{pp}. The dominant noise components are due to the electrode skin interface. Hence, improving interface connection (e.g. using a larger electrode interface) can reduce the noise level and has no impact on the latter signal processing stages. The same idea applies to the reduction of the impact of ambient interference and noise, crosstalk, and so on.

Some techniques are used to disentangle the interplay of voltage noise and current noise. Under some conditions (e.g. dry skin or hair, very small electrode), the electrode skin contact impedance can be as high as 1 MΩ. Thus, a noise current of 100 pA_{RMS} can lead to theoretically unacceptable 100 μV_{RMS}, corresponding to approximately 4-6 μV_{pp} for normally detecting voltage, which implies unneglectable of any nuance fluctuation of current. Therefore, a precedent circuit (e.g. amplifier) must have high input impedance, reaching hundreds of MΩ to limit bad consequences of electrode impedance unbalance.

Sometimes dither technique is utilized, i.e. intentionally adding small Gaussian white noise to input signals before processing. In this way, it can be achieved: a) the total signals with a broader frequency spectrum, b) noise independent of the desired signals, c) eliminating the distortion after the signals are processed.

2.5.2. Deterministic signal processing

2.5.2.1. time domain analysis

After signal preprocessing is completed, the desired digital signal is obtained. There are popularly two distinct perspectives to view these values of the signal, i.e. deterministic values and stochastic values (or random values). However, according to the law of large numbers (Khinchin's law and Kolmogorov's law) in probability theory, it ensures that after a large number of observation signals, the same conclusion is obtained no matter applying deterministic signal processing or stochastic signal processing. Hence, for simplicity, a lot of

engineers tend to use deterministic signal processing to extract information from the time sequence digital data.

The threshold method is widely adopted, taking advantage of easy analysis, simple design and adjustability, computation and data storage efficiency. With regards to gait analysis, respiration analysis, fall detection, electrocardiogram (ECG) analysis, EMG analysis, or electroencephalogram (EEG) analysis, physical or physiological models are established consistent with current knowledge of related disciplines, signals are acquired from wearable systems and compared with the predetermined threshold to give notifications or alarms to users. For example, there is a specific gait pattern before happening of Freezing of Gaits (FoG) for Parkinson's disease [138]. Within smart insoles, signals acquired from triboelectric sensors or piezoelectric sensors are compared with the determined threshold simultaneously to send a fast response to Parkinson's patients to avoid FoG. For another case of wearable ECG system, ECG is a periodic signal, during which the internal values can be compared with various thresholds to calculate heartbeat and other detail components (e.g. P-wave, Q-wave, R-wave, S-wave, T-wave) [139], shown in Figure 2-4.

In addition, complicated algorithms are proposed to solve different problems. Although there is no uniform approach, some points should be stressed: a) the accuracy of algorithms heavily relies on relevant physical or physiological models, b) the algorithms have better interpretability, c) clean signals are essential, i.e. high SNR, no other interference, quite a small signal fluctuation.

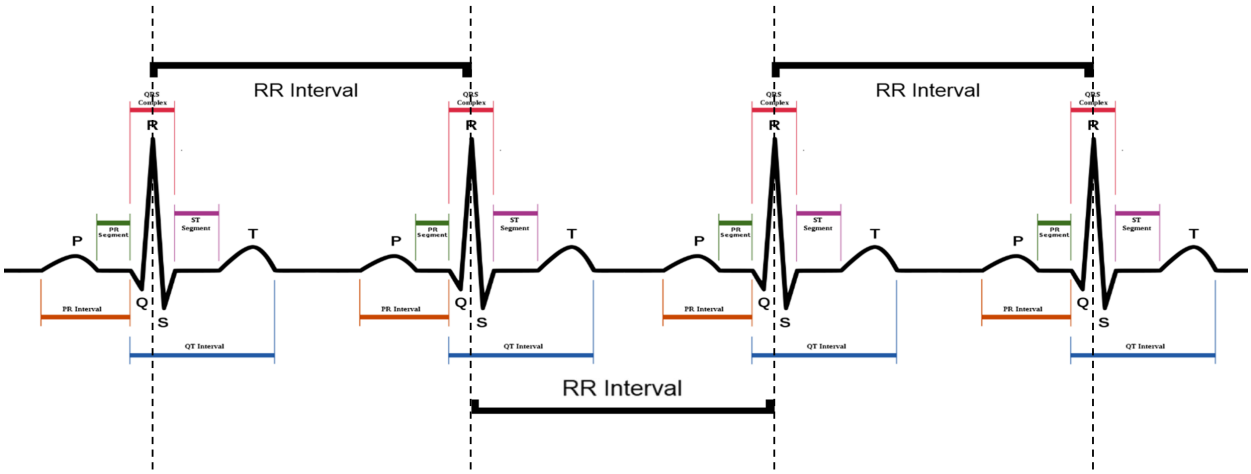

Figure 2-4 Illustration of ECG signal characteristics [140].

2.5.2.2. frequency domain analysis

For some applications, it is convenient to convert time-domain signals to frequency-domain signals, to streamline the whole system analysis, as some systems have simple and direct frequency responses, contradictory to complicated and non-closed-form time responses. For example, to detect an object's displacement, it is better to analyze the Doppler effect which is an intuitive representation of frequency shift.

A Fourier transform approach linearly transforms a time-domain signal to a frequency-domain signal represented by a linear combination of a set of orthogonal bases [141, 142]. Depending on whether the input signal is a periodic/aperiodic continuous/discrete time signal, there are typically four categories of Fourier Transform, i.e. Continuous Time Fourier Series (CTFS), Continuous Time Fourier Transform (CTFT), Discrete Time Fourier Series (DTFS), Discrete Time Fourier Transform (DTFT). Basic properties are highlighted: a) a periodic signal in the time domain corresponds to a discrete spectrum in the frequency domain, b) a continuous signal

in the time domain corresponds to an aperiodic spectrum in the frequency domain, c) an aperiodic signal in the time domain corresponds to a continuous spectrum in the frequency domain, d) a discrete signal in the time domain corresponds to a periodic spectrum in the frequency domain. Below are summaries of forward transform equations, inverse transform equations, Parseval's theorem equations (the law of conservation of energy) for CTFS, CTFT, DTFS, DTFT respectively.

Continuous Time Fourier Series:

forward transform:

$$X_k = \frac{1}{T_0}\int_0^{T_0} x(t)e^{-jk\Omega_0 t}dt \tag{2.1}$$

where $\Omega_0 = \frac{2\pi}{T_0}$ (rad/s)

inverse transform:

$$x(t) = \sum_{k=-\infty}^{+\infty} X_k e^{jk\Omega_0 t} \tag{2.2}$$

Parseval's theorem:

$$\frac{1}{T_0}\int_0^{T_0} |x(t)|^2 dt = \sum_{k=-\infty}^{\infty} |X_k|^2 \tag{2.3}$$

Continuous Time Fourier Transform:

forward transform:

$$X(j\Omega) = \int_{-\infty}^{+\infty} x(t)e^{-j\Omega t}dt \tag{2.4}$$

inverse transform:

$$x(t) = \frac{1}{2\pi}\int_{-\infty}^{+\infty} X(j\Omega)e^{j\Omega t}d\Omega \tag{2.5}$$

Parseval's theorem:

$$\int_{-\infty}^{+\infty} |x(t)|^2 dt = \frac{1}{2\pi}\int_{-\infty}^{+\infty} |X(j\Omega)|^2 d\Omega \tag{2.6}$$

Discrete Time Fourier Series:

forward transform:

$$X[k] = \frac{1}{N}\sum_{n=0}^{N-1} x[n]e^{-jk\omega_0 n} \tag{2.7}$$

where $\omega_0 = \frac{2\pi}{N}$ (rad/sample)

inverse transform:

$$x[n] = \sum_{k=0}^{N-1} X[k]e^{jk\omega_0 n} \tag{2.8}$$

Parseval's theorem:

$$\frac{1}{N}\sum_{n=0}^{N-1} |x[n]|^2 = \sum_{k=0}^{N-1} |X[k]|^2 \tag{2.9}$$

Discrete Time Fourier Transform:

forward transform:

$$X\left(e^{j\omega}\right) = \sum_{n=-\infty}^{+\infty} x[n]e^{-j\omega n} \tag{2.10}$$

inverse transform:

$$x[n] = \frac{1}{2\pi}\int_{0}^{2\pi} X\left(e^{j\omega}\right)e^{j\omega n}d\omega \tag{2.11}$$

Parseval's theorem:

$$\sum_{n=-\infty}^{+\infty} |x[n]|^2 = \frac{1}{2\pi}\int_{0}^{2\pi} \left|X\left(e^{j\omega}\right)\right|^2 d\omega \tag{2.12}$$

In practice, the Fast Fourier Transform (FFT) algorithm is applied to convert discrete time finite duration signals into the frequency domain [142], whose advantages are computational efficiency and data storage efficiency, especially for processing signals samples of an integer power of 2, where "zero padding" technique is always applied to meet the requirement without disrupting original signals information.

Moreover, the "zero padding" technique is widely used for higher frequency resolution. For example, a 250 ms duration signal is sampled as 1000 Hz to get 250 samples, and then a frequency resolution is 4 Hz if directly applying FFT. However, if adding 1750 null samples at the end (or at the beginning) of the original samples, a frequency resolution of 0.5 Hz is achieved. The technique adds no new information but provides more interpolation points at the frequency domain. To achieve higher frequency resolution with more frequency information, it

is adopted to sample more original data (e.g. higher sampling rate or longer sampling duration) and complemented by a zero padding technique.

The FFT is impacted by a phenomenon named leakage. Considering limited frequency resolution which causes frequency spectrum distortion, a portion of the power of one spectral point more or less leaks on the neighboring area. The distortion can be alleviated by choosing a proper window function for processing time domain samples.

2.5.2.3. spatial domain analysis

As any object being sensed by wearable systems occupies a specific space, according to signals collected from different spatial positions, it is feasible to rebuild the corresponding physical models and extract meaningful information. For example, some researchers fabricate smart insoles embedded in a network of flexible pressure sensors, after reconstructing the pressure distribution of users' feet, feet disease analysis and gait analysis can be done [143, 144].

Theoretically, all of the time domain analysis methods can be transplanted to spatial domain analysis. The distinction is that sequence is ordered in time or in space where signals decompose into different directions: x-axis, y-axis, z-axis. For time domain analysis, models are established with the property of causality, which is not necessary for spatial domain counterparts. Similarly, the threshold method is widely used in spatial domain analysis.

In addition, time domain signals can be converted into frequency domain signals, while spatial domain signals can also be converted into frequency domain signals, which benefits to extraction of some elements from the corresponding frequency domain. It should be stressed that one-dimensional Fourie Transform can naturally extend to two-dimensional Fourie Transform and three-dimensional Fourie Transform, which means more complicated frequency domain processing methods can be utilized.

2.5.3. Stochastic signal processing

2.5.3.1. parametric context analysis

Apart from deterministic signal processing, it inevitably encounters stochastic signal processing, under the conditions of a signal with the property of obvious uncertainty (e.g. quite low signal-to-noise ratio), or it is convenient to design a processing system and give performance metrics (e.g. designing a classifier and measuring false positive rate). Basic probability theory and statistics are supportive pillars [145-147].

Maximum Likelihood Estimation (MLE) is widely used. According to the frequentist probability perspective, an event's probability is the limit of its relative frequency in many trials, and its probability distribution is determined by inherent unknown constant parameters (e.g. $\boldsymbol{\theta}$). The parameters can be estimated by maximizing a likelihood function through observed random samples. If samples are independent and identically distributed (i.i.d.), the MLE can be described as below.

$$L(\boldsymbol{\theta}|\boldsymbol{x}) = P(\boldsymbol{x}|\boldsymbol{\theta}) = P(x_1, x_2, \cdots, x_n|\boldsymbol{\theta}) = \prod_{i=1}^{n} P(x_i|\boldsymbol{\theta}) \tag{2.13}$$

$$\widehat{\boldsymbol{\theta}}_{MLE} = \arg\max_{\boldsymbol{\theta}} L(\boldsymbol{\theta}|\boldsymbol{x}) = \arg\max_{\boldsymbol{\theta}} \prod_{i=1}^{n} P(x_i|\boldsymbol{\theta}) \tag{2.14}$$

Alternatively, Maximum A Posteriori estimation (MAP) has also a wide application. Bayesian probability perceives that probability is a reasonable expectation reflecting a state of already-acquired knowledge or quantification of a specific personal belief (hypothesis). Thus a probability is assigned to a hypothesis. Based on a hypothesis with the property of uncertainty, a prior probability (e.g. $P(\boldsymbol{\theta})$) is naturally introduced. Through observational data or evidence which is perceived as fixed, it leads to a posterior probability (e.g. $P(\boldsymbol{\theta}|\boldsymbol{x})$) or evidential probability which evaluates the probability of a hypothesis. The relationship is derived by using Bayes' theorem described below.

$$P(B_i|A) = \frac{P(B_i)P(A|B_i)}{P(A)} = \frac{P(B_i)P(A|B_i)}{\sum_{j=1}^{n} P(B_j)P(A|B_j)} \tag{2.15}$$

If samples are i.i.d., the MAP can be described as below.

$$P(\boldsymbol{\theta}|\boldsymbol{x}) = \frac{P(\boldsymbol{x}|\boldsymbol{\theta})P(\boldsymbol{\theta})}{P(\boldsymbol{x})} = \frac{P(x_1, x_2, \cdots, x_n|\boldsymbol{\theta})P(\boldsymbol{\theta})}{\int P(\boldsymbol{x}|\boldsymbol{\vartheta})P(\boldsymbol{\vartheta})d(\boldsymbol{\vartheta})} = \frac{(\prod_{i=1}^{n} P(x_i|\boldsymbol{\theta}))P(\boldsymbol{\theta})}{\int P(\boldsymbol{x}|\boldsymbol{\vartheta})P(\boldsymbol{\vartheta})d(\boldsymbol{\vartheta})} \tag{2.16}$$

$$\widehat{\boldsymbol{\theta}}_{MAP} = \arg\max_{\boldsymbol{\theta}} P(\boldsymbol{\theta}|\boldsymbol{x}) = \arg\max_{\boldsymbol{\theta}} \left(\prod_{i=1}^{n} P(x_i|\boldsymbol{\theta}) \right) P(\boldsymbol{\theta}) \tag{2.17}$$

where the posterior probability's denominator is independent of parameters thus being omitted when to solve the parameters. In a word, to assume samples' probability distribution is determined by random parameters whose probability distributions (e.g. $P(\boldsymbol{\theta})$) rely on prior knowledge. Therefore, the MAP result is corrected by prior knowledge compared with MLE. If a prior probability is independent of parameters (e.g. uniform distribution), both MAP and MLE have the same result.

After parameters are obtained by MLE or MAP, random samples can be generated by using probability distribution functions, and further be processed by a designed classifier, a designed regression model, a designed prediction model, etc. and corresponding performance metrics are naturally deductive.

2.5.3.2. nonparametric context analysis

Regarding wearable systems' real-case applications, there is a category of complicated stochastic signals, whose distributions do not well match with parameter context models. For example, the sample set presents a multi-peak distribution. Hence, their probability density functions (p.d.f.) directly from observational samples have to be estimated [148, 149].

The simplest one is to do histogram analysis or empirical distribution analysis, which means the first step is to divide the entire values range into a series of intervals (named bins), and the

second step is to count the number of samples falling into each interval. The bins are always consecutive, adjacent, non-overlapping, and equal in size.

Naturally speculating, if the total number of samples is large enough, and the size of the interval is small enough, the probability density function is obtained. Nevertheless, it is hard to meet these two conditions. Therefore, kernel density estimation is used to compromise. One method is called Parzen Window Density Estimation, where described below.

$$p_n(\boldsymbol{x}) = \frac{1}{n}\sum_{i=1}^{n}\frac{1}{h_n^d}\varphi\left(\frac{\boldsymbol{x}-\boldsymbol{x_i}}{h_n}\right) \tag{2.18}$$

where n is the total number of samples, d is the number of space dimensions, h_n is the length of the interval or window width. If h_n is large, estimated p.d.f. become smooth but with low resolution. If h_n is small, estimated p.d.f. has high resolution but sharp and unstable. Hence, h_n is a trade-off when n is limited. $\varphi(\cdot)$ is the kernel function and is commonly chosen from rectangular windows, Gaussian windows, etc. It is proved that the total number of samples is large enough, estimated p.d.f. converges, i.e. $p_n(\boldsymbol{x}) \xrightarrow{n\to\infty} p(\boldsymbol{x})$, no matter what kind of window is chosen. In a word, by using the Parzen Window technique, actually a smoother and more reliable estimated p.d.f. is obtained.

In addition, the k-Nearest Neighbor (kNN) method is used to construct a well-defined MAP classifier, that is given an unlabeled sample (e.g. $\boldsymbol{x}$), to find k closest labeled neighbors and

assign the most frequent label amongst the neighbors to $\boldsymbol{x}$. There is also a trade-off (bias to variance) to determine *k* (the larger *k*, the smoother the result is).

2.5.4. Advanced signal processing techniques

2.5.4.1. wavelet transform analysis

Wearable systems' applications confront a large number of nonstationary signals, such as heartbeat signals for 24 hours covering different activities: walking, running, sitting, sleeping, etc. Different activities have different heartbeat frequencies. Directly applying the Fourier Transform makes it hard to extract the time-variant frequency information. Therefore, time-frequency representation (TFR) analysis is introduced to deal with these nonstationary signals.

If adding truncating windows on time domain signals and doing FT, TFR can be simply done, here assuming the signal is stationary inside the window. The approach is called Short-Term Fourier Transform (STFT), expressed below for continuous time and discrete time signals respectively.

$$STFT\{x(t)\}(\tau,\Omega) = X(\tau,\Omega) = \int_{-\infty}^{+\infty} x(t)h(t-\tau)e^{-j\Omega t}dt \tag{2.19}$$

$$STFT\{x[n]\}(k,\omega) = X(k,\omega) = \sum_{n=-\infty}^{+\infty} x[n]h[n-k]e^{-j\omega n} \tag{2.20}$$

where $\int_{-\infty}^{+\infty}|h(t)|^2 dt = 1$, i.e. normalized window which is chosen from window function candidates, such as rectangular window, Hann window, Gaussian window, etc. Moreover, the spectrogram can be defined as below, representing the signal Power Spectral Density.

$$spectrogram\{x(t)\}(\tau,\Omega) = |X(\tau,\Omega)|^2 \tag{2.21}$$

The original signal is reconstructed by applying inverse STFT.

$$x(t) = \frac{1}{2\pi}\int_{-\infty}^{+\infty}\int_{-\infty}^{+\infty} X(\tau,\Omega)\, e^{j\Omega t} d\tau d\Omega \tag{2.22}$$

However, according to the Heisenberg uncertainty principle ($\Delta t \Delta\omega > constant$), time resolution and frequency resolution are dependent, i.e. it cannot gain low time resolution and low frequency resolution simultaneously. Intuitively considering STFT with a certain window width, a short window leads to a high time resolution but a low frequency resolution. This resolution problem can be solved if the window is of variable width, that is short one for high frequency parts and long one for low frequency parts. Hence Wavelet Transform (WT) is brought in [150-155].

WT method is to project input nonstationary signals on complete orthonormal basis functions, i.e. wavelet functions, which have time widths adapted to different frequency bands. It realized variable time resolution and frequency resolution simultaneously. Here Continuous Wavelet Transform (CWT) is defined as below:

$$CWT_{\psi}\{x(t)\}(a,b) = \frac{1}{\sqrt{a}}\int_{-\infty}^{+\infty} x(t)\psi\left(\frac{t-b}{a}\right)dt \tag{2.23}$$

where $\psi(t)$ is named as the mother wavelet, being chosen from different candidates, such as Morlet, Daubechies, Coiflets, Biorthogonal, Mexican Hat, Symlets, etc. The child wavelet is defined as:

$$\psi_{a,b}(t) = \frac{1}{\sqrt{a}}\psi\left(\frac{t-b}{a}\right) \tag{2.24}$$

where a is positive and stands for scaling (or dilation), b is a real number and stands for translation (or time shifting). Similar to the spectrogram in STFT, the energy distribution is defined, i.e. scalogram:

$$scalogram_{\psi}\{x(t)\}(a,b) = \left|CWT_{\psi}\{x(t)\}(a,b)\right|^2 \tag{2.25}$$

In addition, for computational efficiency, Discrete Wavelet Transform (DWT) is suitable, which means discretized scaling, translation and time, and only suitable for discrete sequence $x[n]$.

$$DWT_{\psi}\{x[n]\}(j,k) = \frac{1}{\sqrt{a^j}}\sum_{n=-\infty}^{+\infty} x[n]\psi\left[\frac{n-ka^jb}{a^j}\right] \tag{2.26}$$

where a and b are real numbers satisfying $a > 1, b > 0$, while j and k are integer numbers. Especially it can derive dyadic expression, if let $a = 2, b = 1$.

$$DWT_{\psi}\{x[n]\}(j,k) = \frac{1}{\sqrt{2^j}} \sum_{n=-\infty}^{+\infty} x[n]\psi\left[\frac{n - k2^j}{2^j}\right] \tag{2.27}$$

Correspondingly it can derive the child wavelet expression.

$$\psi_{j,k}[n] = \frac{1}{\sqrt{2^j}}\psi\left[\frac{n - k2^j}{2^j}\right] \tag{2.28}$$

Furthermore, the Mallet algorithm is the commonly used fast algorithm to implement DWT and achieve multiresolution analysis which means a signal is decomposed into a set of frequency bands with different resolutions, as illustrated in Figure 2-5. Here this is implemented on the dyadic grid, so the frequency band is divided into octave sub-bands.

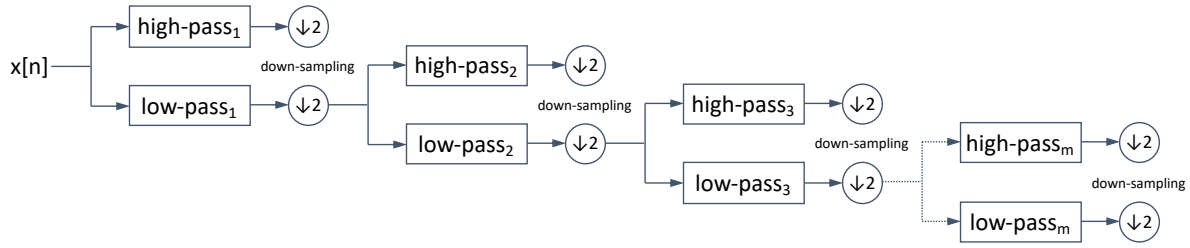

Figure 2-5 Mallet algorithm illustration.

2.5.4.2. stochastic process analysis

As discussed one random variable, furthermore it can be analyzed on a set of random variables located along the timeline (or other index parameters), which is called the Stochastic Process

[156, 157]. This technique has numerous applications in wearable systems. For example, a wearable system discriminator (e.g. Parkinson's disease) is designed by the input of a sequence of historic data (e.g. long-term gait data).

A typical stochastic process can be denoted as $\boldsymbol{X}(t, \theta)$. For an arbitrary moment $t_0 \in T$, $\boldsymbol{X}(t_0, \theta)$ becomes a random variable, while 2.5.3 STOCHASTIC SIGNAL PROCESSING techniques can be utilized. For a sample $\theta_0 \in \Theta$, $\boldsymbol{X}(t, \theta_0)$ becomes a deterministic function of time, called the sample function (or the sample path, the realization, the trajectory), while 2.5.2 DETERMINISTIC SIGNAL PROCESSING techniques can be utilized. Well-defined specific stochastic processes include the Bernoulli process, Random walks, Wiener process, Poisson process, Gaussian process, Markov process, Lévy processes, etc.

Generally, stochastic process distribution functions are difficult to gain and analyze, except above mentioned specific stochastic processes. Therefore it's a better choice to care more about the properties of a stochastic process to conveniently extract desired information or design some expected discriminators [158]. The first one of the two most important properties is stationarity, which means all random variables along the time present the same statistical behavior, i.e. independent of the time index. Strict stationarity is defined in terms of the joint distribution, while a wide sense stationarity is defined on a) a second-order process existence, b) a constant mean function, c) a correlation function depends only on the time difference. In real application, it mainly concentrates on a wide sense stationary process (or weak stationary process, covariance stationary process, second-order stationary process, Khintchin stationary process).

Additionally, it is widely used window functions on a nonstationary process to get segmented stationary processes. The second one of the two most important properties is ergodicity, which means the same statistical behavior regardless of whether any arbitrary random variable or the appropriate time average value corresponds to a single sample function. $\boldsymbol{X}(t)$ is a stationary and ergodic process, then

$$\mu = E[\boldsymbol{X}(t)] = \lim_{T\to\infty} \frac{1}{2T} \int_{-T}^{T} X(t)dt \tag{2.29}$$

$$\mu = E\{\boldsymbol{X}[n]\} = \lim_{N\to\infty} \frac{1}{2N+1} \sum_{k=-N}^{N} X[k] \tag{2.30}$$

and

$$R(\tau) = E[\boldsymbol{X}(t+\tau)\boldsymbol{X}(t)] = \lim_{T\to\infty} \frac{1}{2T} \int_{-T}^{T} X(t+\tau)X(t)dt \tag{2.31}$$

$$R[\tau] = E\{\boldsymbol{X}[n+\tau]\boldsymbol{X}[n]\} = \lim_{N\to\infty} \frac{1}{2N+1} \sum_{k=-N}^{N} X[k+\tau]\,X[k] \tag{2.32}$$

where $E[\cdot]$ stands for expected value and $R(\tau)$ is named an autocorrelation function.

When analyzing a stationary process, its energy integral along all time is infinite. Hence it is impossible to directly use the Parseval's theorem but to use a modified one by introducing Power Spectral Density (PSD), whose definition is presented below.

$$S_X(\Omega) = \lim_{T\to\infty} \frac{1}{2T} E\left[\left|\int_{-T}^{T} \boldsymbol{X}(t) e^{-j\Omega t} dt\right|^2\right] \tag{2.33}$$

so the modified equation for the average power is shown below.

$$\frac{1}{2\pi}\int_{-\infty}^{+\infty} S_X(\Omega) d\Omega = \lim_{T\to\infty} \frac{1}{2T}\int_{-T}^{T} E[|\boldsymbol{X}(t)|^2] dt \tag{2.34}$$

It is convenient to calculate PSD for a wide sense stationary process, according to the Wiener-Khinchin theorem, by Fourier Transform its autocorrelation function (e.g. $R_X(\tau)$).

$$S_X(\Omega) = \int_{-\infty}^{+\infty} R_X(\tau) e^{-j\Omega\tau} d\tau \tag{2.35}$$

$$R_X(\tau) = \frac{1}{2\pi}\int_{-\infty}^{+\infty} S_X(\Omega) e^{j\Omega\tau} d\Omega \tag{2.36}$$

and for a discrete-time process,

$$S_X(\omega) = \sum_{k=-\infty}^{+\infty} R_X[k] e^{-j\omega k} \tag{2.37}$$

$$R_X[k] = \frac{1}{2\pi}\int_{0}^{2\pi} S_X(\omega) e^{j\omega k} d\omega \tag{2.38}$$

In real applications and further complicated analysis, these models are widely adopted to rebuild the mechanism generating received time sequence, and more important to do forecast, including

Autoregressive Integrated Moving Average (ARIMA), Autoregressive Moving Average (ARMA), Autoregression (AR), and Moving Average (MA) [159]. The general main work process is depicted in Figure 2-6.

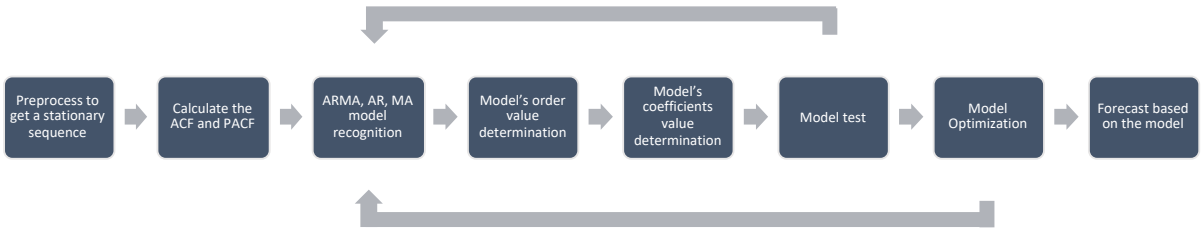

Figure 2-6 ARIMA model work process illustration.

Wherein trend differencing, seasonal differencing, and n-order differencing are beforehand applied to eliminate the non-stationarity of the original sequence. Because of noise, AR models exhibit no rigid truncated autocorrelation function (ACF) and MA models exhibit no rigid truncated partial autocorrelation function (PACF). Therefore, the Akaike Information Criterion (AIC) or Bayesian Information Criterion (BIC) can be leveraged to determine a low-order ARMA or AR or MA model. For the model test, it should ensure the residue error is White Gaussian Noise, by several test methods, such as the p-value approach, Durbin-Watson test, Ljung-Box test, etc. Finding an appropriate ARMA or AR or MA model is not an easy task, so it is advised to do iterative optimization, as shown in Figure 2-6. Finally for a model analysis, an ARMA or AR or MA model has a property of a rational PSD function.

2.5.5. Advanced data science processing techniques

2.5.5.1. machine learning

Nowadays wearable systems usually contain complex data processing subsystems, because users care more about heuristic understandable information such as different health indexes and further guidance, rather than only single signal indication, and also because there are great amounts of data and models available from diverse sources such as personal online digital twin from Web or mobile applications development companies, which makes it valuable to merge big data to give more accurate and individualized recommendation.

Data science techniques are becoming mature based on above mentioned requirements. They are very powerful when dealing with large data volumes, high data dimensions, complex data structures, sophisticated models, implicit information, etc. These techniques can automatically find out the model or pattern of available data and mine hidden desired information with respect to designed purposes. More or less it is inevitable to utilize these techniques for backend development of smart wearables.

Generally, data science follows the work process flowchart or cross-industry standard process for data mining (CRISP-DM) process, as illustrated in Figure 2-7. It is not wise to put equal effort into each phase, but some basic principles should be highlighted: a) well-define questions will lead to beneficial answers, b) data quality is the core value, otherwise poor data quality will lead to poor performance, that is garbage in and garbage out issues, hence data filtering or cleaning should always be done, c) performance criteria should be established at first since different criteria demand different models, d) depending on different applications, interpretability and privacy need to be paid more special attention during the whole work

procedure including model selection, model design, model tuning, and model deploying, e) these are dynamic procedures demanding iterative optimization and continuous improvement.

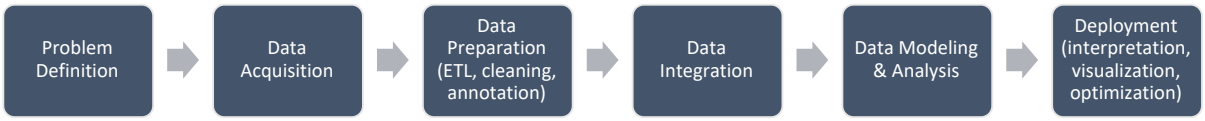

Figure 2-7 Data science work process pipeline.

Benefiting from mature and interpretable models, Machine Learning (ML) approaches are desired to deal with some interesting problems. ML approaches are based on establishing a model by exploiting sample data, named training data, to make further decisions or predictions without esoteric programming on purpose [160-163]. In a word, let machines (e.g. computers or mobiles or terminals) work as human does. Below is a summary of renowned general problems and corresponding classic ML models.

Regression problems are commonly met when trying to find the pattern of a bundle of data and do interpolation and extrapolation afterward. Popular models include Linear Regression, Polynomial Regression, Logistic Regression, etc.

Classification problems are also common when facing to do fast inference decisions. The candidate solution models include Linear Classifier (e.g. Fisher's linear discriminant, Naïve Bayes classifier), Decision Trees, Random Forest, Support Vector Machine, K Nearest Neighbor, etc.

Clustering problems are instrumental in organizing large volumes of both labeled and unlabeled data, facilitating subsequent analysis and inference of new input data. Various clustering techniques offer candidate solutions, each characterized by unique methodologies. Hierarchical clustering methods, such as Balanced Iterative Reducing and Clustering using Hierarchies (BIRCH) and Clustering Using REpresentatives (CURE), structure data into nested clusters based on hierarchical relationships. In contrast, partition-based clustering, exemplified by the K-Means algorithm, segments data into distinct groups by optimizing a specific criterion. Density-based clustering techniques, such as Density-Based Spatial Clustering of Applications with Noise (DBSCAN), focus on identifying clusters within regions of high data density. Grid-based approaches, including Statistical Information Grid (STING) and Clustering in QUEst (CLIQUE), employ a grid structure to facilitate data clustering. Model-based clustering, represented by methods like the Self-Organizing Map (SOM), utilizes statistical models to form clusters. Finally, distribution-based clustering, such as the Expectation-Maximization (EM) algorithm, presumes that data originates from a mixture of distributions to discern clusters. Each of these methodologies contributes uniquely to the effective grouping and analysis of complex datasets.

Anomaly detection problems are another category when applying ML to smart wearable systems to fight against interference and dirty data. The frequently used models include K Nearest Neighbor, Local Outlier Factor, etc.

2.5.5.2. deep learning

Apart from above mentioned ML approaches, in recent decades Deep Learning (DL) has become more and more popular and has gained much wider applications [164]. DL takes advantage of end-to-end training, which requires designers with little ability to create complex algorithm models, but focus on training data acquisition and preparation, although DL has an obvious disadvantage of interpretability challenge. Contributed by Hornik's theoretic analysis work [165-168], Neural Networks (NN) can approximate Borel measurable functions, which means these NN can replace sophisticated data processing functions. Moreover, researchers find out deeper NN can extract more abstract and more wealthy information, especially after the emergence of the AlexNet model [169, 170]. Hence, DL by using deep neural networks, becomes a generally utilized paradigm, as shown in Figure 2-8.

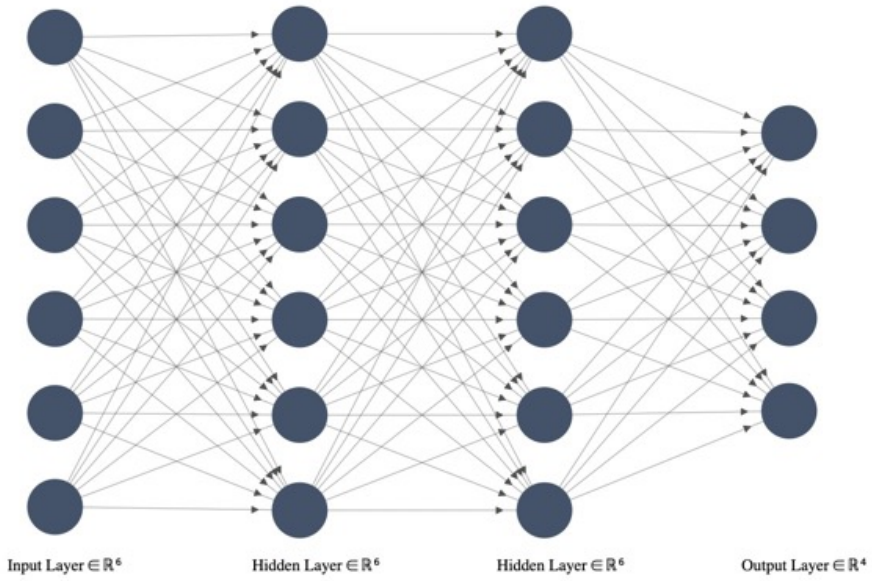

Figure 2-8 Deep neural network diagram.

Regarding of smart wearable applications, there are several basic useful techniques when applying DL: a) input data are always processed with mean subtraction and normalization, to

standardize the data of zero mean and variance equaling to 1, b) simple problems can be solved by Multi-Layer Perceptron (MLP) with less layers, while complex problems are recommend to be solved by Convolutional Neural Network (CNN) with deeper layers and replicated neurons connection patterns [170-172], and by Recurrent Neural Network (RNN) if input data is a correlated sequence [173-176], c) Hyper-parameters (e.g. number of layers, number of neutrons per layer) are reliable on different validation set data, so K-fold cross validation is recommended for small validation dataset, d) optimization techniques include Stochastic Gradient Descent, Batch Gradient Descent, Momentum [177, 178], AdaGrad [179, 180], RMSProp [181], AdaDelta [182], Adam [183, 184], etc., e) loss function determination is the core target, and adding regularization term can overcome the overfitting problem, f) to gain robustness, Batch Normalization [185], Dropout [186], etc. techniques are commonly used, g) parameters initialization can be done through Xavier initialization techniques and others for practical purpose [187-189], h) DL should be viewed as a data-driven dynamic learning process, rather than a once fixed model.

With the fast developments and various applications of wearable systems, traditional signal processing cannot give guidance to a unified architecture. The complex scenarios make it impossible to establish the system's time response or the system's frequency response to describe the characteristics of the system of interest. Moreover, probability models are not enough to describe, considering specific probability models, such as uniform distribution and Gaussian distribution, are rather sensitive to conditions, while other nonparametric methods are restricted by limited samples available. Ultimately data-driven approaches, including machine

learning and deep learning seem feasible. However, lacking interpretability, heavy computation resources and storage resources impede their wide applications. Hence, signal processing for wearable systems is worthy of special attention and research in depth.

2.6. Muscle Force Detection and Estimation

2.6.1. Importance of gastrocnemius muscle

The gastrocnemius muscle, a robust and substantial muscle situated in the posterior compartment of the lower leg, plays a pivotal role in plantar flexion of the foot, which means the downward pointing of the toes, and in the flexion of the knee joint. This muscle is anatomically composed of two distinct heads: the medial and the lateral. The medial head, which is the larger of the two, is positioned more proximally to the body's midline, whereas the lateral head is situated more distally, toward the lateral areas of the legs. It is noteworthy that the muscle fibers of the lateral head contain a greater number of sarcomeres compared to those in the medial head. However, the impact of this disparity on the muscle's length-force relationship is moderated by the variation in pennation angles between the two heads [190].

The gastrocnemius muscle receives its innervation from the tibial nerve, which is a subsidiary of the sciatic nerve. The sciatic nerve, recognized as the most voluminous nerve in the human anatomy, extends along the posterior region of the thigh, continuing its trajectory into the lower leg.

The gastrocnemius muscle is a vital muscle for many daily activities such as maintaining posture, walking, and executing dynamic movements [191, 192]. It is also important for maintaining balance and posture [193]. The gastrocnemius muscle serves a critical biomechanical function as a primary shock-absorbing mechanism during weight-bearing activities, providing essential protection to lower extremity joints during ground contact phases of locomotion. This protective function is particularly important during high-impact activities where rapid deceleration forces must be efficiently dissipated to prevent joint injury.

The gastrocnemius muscle works synergistically with the deeper soleus muscle to form the triceps surae muscle complex, as shown in Figure 2-9, which represents the primary force-generating unit for ankle plantarflexion movements. This muscle group collectively contributes approximately 80% of the total plantarflexion torque capacity [194, 195], establishing it as the dominant contributor to ankle joint function and lower extremity propulsion. The substantial force contribution of the triceps surae complex underscores its clinical significance in rehabilitation medicine and its relevance as a target for therapeutic intervention and performance assessment.

Although the gastrocnemius muscle significantly contributes to human basic postural and movement, there is seldom research directly related to muscle force generated by the gastrocnemius muscle contraction in vivo and behind the mechanism. The reasons are complex, while the most fundamental hurdle is the lack of methods and related devices to dynamically measure muscle status to determine the muscle force.

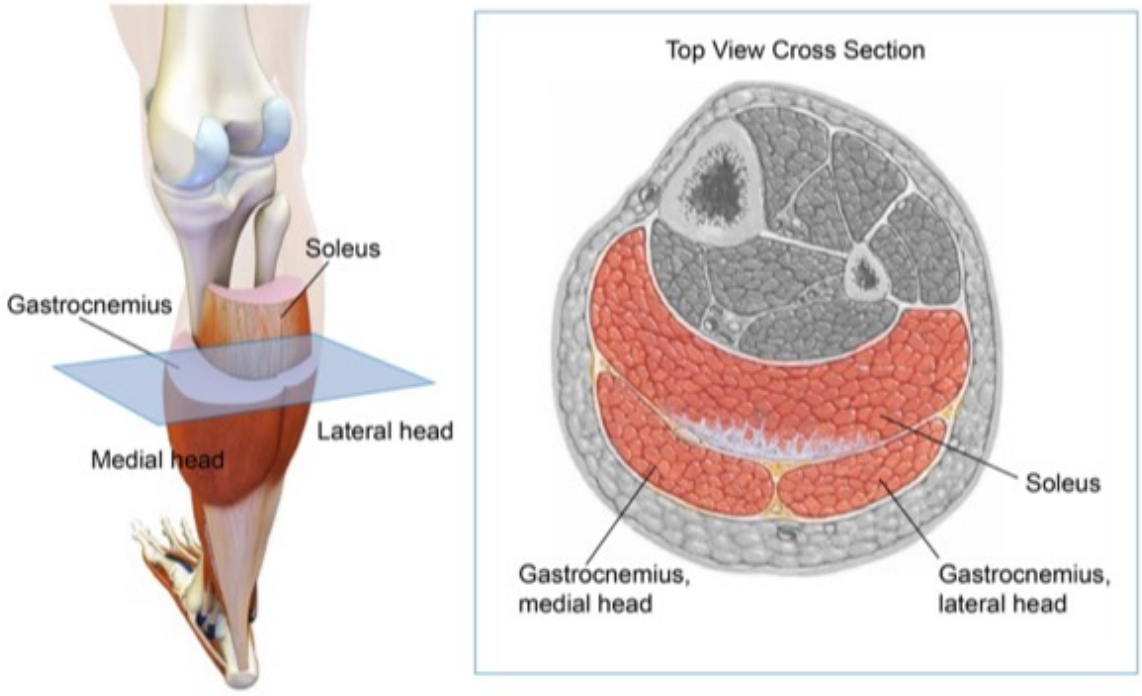

Figure 2-9 Illustration of lower extremities muscle structure and anatomic cross-section, where the triceps surae muscle complex consists of the two-headed gastrocnemius and the soleus [196].

Generally, two traditional popular modeling methods are to quantitatively predict the related muscle force [197], which are EMG-driven optimizations [198-200] and PCSA-driven optimizations [201-204]. Although there are a wide of applications of the EMG method and the PCSA method to detect muscle status qualitatively and quantitatively, both methods face inherent obstacles to obtaining accurate and simultaneous data.

2.6.2. Introduction of EMG method and limitations

EMG is a technique used to record the electrical activity of muscles [200]. The EMG received signal is powered by the depolarization of muscle fibers, which occurs when they are activated

by motor neurons. The depolarization wave travels along the muscle fiber, causing it to contract. The EMG signal can be recorded by using specific surface electrodes fixed on the skin areas near the muscle. The electrodes are connected to an amplifier and a recording device, which can then display the signal on a screen or store it for later analysis.

Upon activation, a motor neuron initiates the propagation of action potentials along its axon, which in turn stimulates the motor end plates of the corresponding muscle fibers. This stimulation results in the generation of depolarization waves that traverse the membrane of the muscle fiber at velocities ranging from 3 to 6 meters per second, extending toward the extremities of the fiber. The conductive tissues enveloping the active fibers facilitate the detection of this electrical activity by electrodes positioned at a distance, thereby constituting the EMG signal that is recorded. Concurrently, the depolarization wave precipitates the release of calcium ions, thereby instigating the mechanical contraction process. Notably, this mechanical contraction process unfolds at a markedly slower pace than the electrical depolarization, which concludes within merely 2 milliseconds. The generation of maximum force is observed within a timeframe of 20 to 150 milliseconds after a singular depolarization event, whereas the decline in force, attributed to the reuptake of calcium, necessitates a duration that is at least twice as prolonged. It is imperative to acknowledge that these mechanical aspects of muscle contraction do not, in themselves, generate electrical activity.

Skeletal muscle is constituted by fibers that are innervated by alpha-motor neurons. The soma of these neurons is located within the spinal cord, and their axons extend, traveling through

nerves to reach the target muscle. Upon arrival at the muscle, each axon bifurcates to establish different motor end plates corresponding to the respective muscle fibers. Collectively, a motor neuron and the corresponding muscle fibers are named a motor unit, which represents the fundamental unit generating muscular contraction. Motor units exhibit considerable variability in size, encompassing a range from a mere handful to several thousand fibers, and they display distinct physiological characteristics. Typically, smaller motor units incorporate slow-twitch but fatigue-resistant fibers, whereas larger units predominantly incorporate fast-twitch but fatigue-susceptible fibers. The different composition of fiber types within a muscle is determined by the specific functional demands placed upon it; for instance, muscles that maintain posture are primarily composed of slow-twitch fibers, whereas muscles that are engaged in rapid, forceful contractions tend to have a higher proportion of fast-twitch fibers.

Muscle force generation is governed by two primary mechanisms: the recruitment of motor units and the modulation of firing rates on them. The recruitment process adheres to the size principle law, whereby motor units are sequentially activated in ascending order from the smallest to the largest in response to escalating force requirements. Subsequent to their recruitment, there are firing rates progressive increment for the active motor units to meet higher demands for force. It is characteristic for motor units to fire in an asynchronous manner. The technique of EMG serves to reflect both the recruitment of motor units and variations in their generated firing rates. During minimal muscular contractions, a limited number of nearby motor units are consequently activated. Conversely, the generation of higher forces necessitates

the involvement of a greater number of motor units, with the superimposition of their generated action potentials resulting in EMG signals that exhibit a noise-like quality.

Regarding the EMG methodology, this widely utilized non-invasive technique facilitates the assessment of muscular status and enables the prediction of muscle force. There exists comprehensive guidance and established recommendations for the application of this method, exemplified by resources such as the Surface ElectroMyoGraphy for the Non-Invasive Assessment of Muscles (SEMNIAM) [205, 206]. However, the efficacy of this technique is compromised by inherent limitations, such as the phenomenon of cross-talk, variability in electrode placement, and the activation of synergistic muscles during the generation of force, among others [207].

The phenomenon of electrical cross-talk from neighboring muscles exerts an increased influence on the EMG signal quality especially when the force exerted by the target muscle intensifies. This issue is particularly pronounced in the case of smaller muscles, where the proximity of surface electrodes to adjacent musculature is often unavoidable. The complexity of cross-talk is further compounded by other factors, such as the anisotropic properties of muscle tissue and the heterogeneity of surrounding tissues. Accurately identifying the origin of signal contamination within the physiological data is frequently challenging, if not impossible. Additionally, the extent of synergistic activity from other muscle groups and the degree of co-contraction among antagonistic muscles can significantly modify the resultant contribution of muscle strength in some studies [208]. In practical applications, to enhance the accuracy of

EMG data, it is advisable to select a muscle that is solely responsible for the force being measured [209].

Variability in electrode placement is an unavoidable aspect when conducting repeated EMG measurements. This variability can significantly impact the results due to the spatial distribution of fast-twitch and slow-twitch muscle fibers within the muscle of interest and their distances to the fixed electrodes. A muscle fiber can generate action potentials whose amplitude is directly proportional to the fiber's diameter. Consequently, fast-twitch fibers, characterized by larger diameters, produce action potentials with higher amplitudes in comparison to slow-twitch fibers. However, it is important to note that the recorded signal's amplitude is inversely correlated with the distance between the active fibers and the recording electrodes. Increased distance between these elements leads to attenuated signal amplitudes. The size principle law indicates that during activities necessitating high force output, the recruitment of motor units primarily involves the largest motor units, composed of fast-twitch fibers with the largest diameters [210, 211]. Consequently, the placement of electrodes relative to fast-twitch muscle fibers plays a crucial role in determining how the electrical activity from these motor units is manifested in the surface EMG signal [212].

The integrity of EMG data may be compromised by a multitude of individual-specific factors, including stochastic electrical noise, inaccuracies in electrode placement, and intra-individual variability [213]. The application of different signal processing techniques to EMG data can yield disparate outcomes, posing a challenge in ascertaining the most suitable processing

method and the veracity of the resultant data. For instance, the application of a low-pass filter with a cutoff frequency of 25 Hz, as per Hof's method [214], marginally diminishes the signal while preserving its characteristic sharp and spiked profile. Conversely, employing Winter's method [215] for signal smoothing not only attenuates the signal but also introduces a delay in the occurrence of peak values. In conclusion, the EMG methodology is susceptible to potential inaccuracies during stages of signal acquisition, signal processing, and the subsequent data analysis, including the use of documented maximal force values for normalization purposes [216-219].

2.6.3. Introduction of PCSA method and limitations

The muscle properties of the human body are a complex and fascinating topic. The interplay of muscle anatomy, physiology, and functional demands results in a wide range of muscle specializations that allow humans to perform a variety of tasks.

In striated muscle, the structural composition comprises elongated and slender muscle fibers that are organized into fascicles and further aggregated into muscle bellies. The initiation of muscle contractions occurs when specific sites within the muscle fiber, capable of generating tension, are stimulated. The fundamental unit of muscle contraction is the sarcomere, characterized by its repetitive organization of interlocking thick myosin and thin actin protein filaments. During muscle contraction, the sarcomeres undergo a reduction in length, facilitated by the formation of cross-bridges between the myosin heads and actin molecules. This cyclic process encompasses the stages of cross-bridge formation, contraction, detachment, and

subsequent reattachment. Importantly, the energy required for this mechanism is derived from the hydrolysis of Adenosine triphosphate (ATP).

The contractile properties of a muscle are influenced by several anatomical and physiological factors, including the fascicle count: The more fascicles a muscle has, the greater its cross-sectional area and the more force it can produce. The fascicle length: This affects the total number of sarcomeres arranged in series within the muscle. Longer fascicles possess a larger number of sarcomeres, resulting in enhanced contractile velocity. Consequently, muscles with longer fascicles have greater potential for requirements of speed and movement. Pennation angle: This refers to the angle at which muscle's fascicles are oriented relative to their associated tendons. A larger pennation angle enables a wider range of motion. However, it also diminishes the muscle's ability to generate force. The size and types of muscle fibers: muscle fibers come in two main types: slow-twitch fibers and fast-twitch fibers. Slow-twitch fibers are fatigue-resistant and have a high oxidative capacity, while fast-twitch fibers are capable of generating high-force contractions but fatigue more quickly. The type of muscle fibers in a muscle is determined by its functional demands.

The force-generating capacity within a muscle has a higher correlation with its total number of sarcomeres and associated cross-bridges. Increased sarcomere content, via greater muscle fiber number, permits more myosin-actin interactions and heightened force production. Thus, a muscle's cross-sectional area, which encapsulates its fiber number, provides an index of

maximal force generation. PCSA represents a measurement of a muscle's force generation capacity [220].

The operational range of a muscle is contingent upon the length of its fascicles. An increase in fascicle length correlates with an enhanced range of motion that the muscle is capable of executing. Nonetheless, an augmentation in fascicle length may concurrently result in a diminished capacity for force production within the muscle. Given a constant muscle volume, it is infeasible to simultaneously maximize both muscle-generating force and operational range due to the intrinsic force-velocity relationship. For example, postural muscles are characterized by a requirement for high force output with minimal changes in length, whereas muscles involved in rapid movements typically exhibit shorter lengths but higher contractile velocities. The architecture of muscle is subject to adaptation to optimize parameters such as force, excursion, work, and power to meet specific functional demands, thereby enabling humans to execute a diverse array of activities.

PCSA is recognized as a representative metric for quantifying muscle force within the domain of quantitative muscle architecture [221, 222]. The calculation of PCSA requires the integration of multiple anatomical parameters, including muscle volume, fascicle length, and pennation angle measurements. These geometric and architectural parameters are essential for accurately determining the effective cross-sectional area of muscle fibers that contribute to force generation. Muscle performance estimation, including both maximum isometric force capacity and instantaneous power output, is mathematically derived through the multiplication of PCSA

by maximum isometric stress values [223-225]. This fundamental relationship provides the theoretical foundation for predicting muscle force-generating capacity based on anatomical measurements and established stress constants for skeletal muscle tissue.

$$PCSA\ (cm^2) = \frac{Muscle\ Volume\ (cm^3) \times Pennation\ Angle\ (\cos\theta)}{Fascicle\ Length\ (cm)} = \frac{Muscle\ Mass\ (g) \times Pennation\ Angle\ (\cos\theta)}{Muscle\ Density\ (g \cdot cm^{-3}) \times Fascicle\ Length\ (cm)} \quad (2.39)$$

In contemporary practice, PCSA of a muscle may be quantified to ascertain the muscle's cross-sectional area at a specific longitudinal point, utilizing a range of methodologies [226]. Magnetic resonance imaging (MRI) represents a non-invasive imaging modality technology, which can produce relatively high-resolution images of the body's soft tissues. Computed tomography (CT) is an alternative non-invasive imaging technique that provides detailed cross-sectional images of the patient's body's soft tissues. Ultrasound imaging, another non-invasive approach, employs acoustic waves to generate visual representations of the body's soft tissue structures. Disadvantages of these methods include high cost, time-consuming process, low availability in all hospitals and clinics, bulky machines, low movability, inconvenient usage, and even high risk of exposing patients to radiation. In essence, these methods cannot provide wearable, easy-to-use, real-time measurement.

2.7. Summary and Statements of the Research Problems

This chapter reviews the historical development of compression therapies and traditional compression garments, and diverse application scenarios, such as chronic venous disease management, scar management, orthopedic application, body shaping application, sportswear application, and other applications. Although these requirements are different, traditional compression garments have obvious general shortcomings, such as that pressure ranges are not customized, it is impossible to real-time monitor the essential pressures or health status of users, users cannot receive spontaneous feedback, user compliance and follow-up care cannot be improved. Therefore, by reasonable inferring, a novel smart compression garment is highly demanding and precious.

For smart compression garments, wearable sensors to accurately and in real-time measure static pressure and dynamic pressure are pivotal. Current piezoelectric sensors and triboelectric sensors are inappropriate to measure static pressure. Optical sensors need complex supportive systems and are not suitable for the wearable. Piezoresistive sensors exhibit limited sensitivity in the low-pressure range and temperature change susceptibility. Capacitive sensors take advantage of moderate or high sensitivity, high durability, and fast response speed. However, increasing sensitivity and integration of smart compression garment systems need more research and experiments.

For wearable circuit systems design and implementation, more efforts are put into the physical layer design. Nonetheless, considering there exist no unanimous standards and guidelines for signal processing after wearable systems are established, this chapter in-depth reviews

mainstream general techniques and provides some intuitive guidance. In the beginning, signal preprocessing is highly desired, including signal conditioning, sampling and quantization, analog-to-digital conversion, digital filter, and denoise, where all these techniques are implemented on analog circuits or digital circuits to accelerate responsive speed and decrease power consumption. The main purposes are to amplify original physical signals, transform signals, digitalize signals, filter signals, and denoise signals so that final signals are digital numbers with higher power density and weaker background noise, interference, and other undesired signals. After signal preprocessing, a variety of kinds of signal-processing approaches are introduced to realize wearable systems functions. These approaches are computation and storage intensive. Hence, programmable and powerful hardware logic units are demanded to guarantee wearable systems performance. To deal with deterministic signals, it is commonly adopted time domain analysis, spatial domain analysis, frequency domain analysis where classic Fourier Transform is essential, including CTFS, CTFT, DTFS, DTFT, FFT. To deal with stochastic signals, it is commonly adopted MLE, MAP, and other nonparametric context estimations. Furthermore, to deal with signals with complex features, advanced approaches are inevitable, such as the time-frequency representation of STFT and Wavelet Transform (CWT, DWT), PSD analysis for stochastic processes and ARIMA. Lastly, to extract higher-level information from complex signals, Machine Learning and Deep Learning are recommended, where accuracy performance is increased at the cost of weak interpretability and computation complexity of models. This is worthwhile because models can automatically learn the latent patterns of signals without human intervention while human labor concentrates on quality data collection, model adjustment and model performance evaluation. Therefore, a

new architecture of signal processing for wearable systems is treasured, requiring more and deeper study.

Moreover, the gastrocnemius muscle is a vital muscle for many daily activities such as maintaining posture, walking, executing dynamic movements, and shock absorbing. Although there is a wide of applications of the EMG-related methods and the PCSA-related methods to detect gastrocnemius muscle status qualitatively and quantitatively, both methods face inherent obstacles to obtaining accurate and simultaneous data. Therefore, applying a novel smart compression garment system to monitor the gastrocnemius muscle is valuable, and promising, but also challenging.

To sum up, in this thesis the below problems will be addressed.

(1) Compression therapies and traditional compression garments applications, including chronic venous disease management, scar management, orthopedic application, body shaping application, sportswear application, and other applications, cannot monitor variation in pressure and provide accurate therapies accordingly. The imperceptible, multifunctional, long-term used, dedicated smart compression garments are highly desirable.

(2) To measure static pressure and dynamic pressure on the compression garments, compared with piezoelectric sensors and triboelectric sensors, which are suitable for dynamic pressure measurement, optical sensors and piezoresistive sensors, which are restricted by complex

configuration systems and temperature impact susceptibility respectively, capacitive sensors have advantages of simple design, low power consumption, stable output. However, to increase sensitivity below 50 mmHg and comprehensive integration with smart compression garments lack of study.

(3) After the electrical and mechanical integration of the smart compression garment system, the sensors' performance is deteriorated by parasitic capacitances caused by surrounding electromagnetic interference, proximity effects, and deformation on curved surfaces, which means frequency overlapped noise and non-stationary noise. The conventional signal processing methods, including deterministic signal processing, stochastic signal processing, and advanced signal processing techniques, cannot guarantee denoise performance uplift. A unified cost-effective, agile architecture should be studied.

(4) The gastrocnemius muscle force is vital for daily life activities. Traditional assessment methods, like electromyography and physiological cross-sectional area measurements, often struggle to provide precise real-time data while ensuring user comfort and practicality in both clinical and community settings. Hence, a smart compression garment system can be potentially applied. Nevertheless, the efficacy should be based on the dedicated clinical study and statistical analysis of a large cohort.

Chapter 3 Sensors Fabrication and Integrated Smart Compression Garment Systems

3.1. Introduction

In this chapter, it was proposed for a smart compression garment with embedded flexible sensors, edge control units, user interactive devices, and software applications. The components were all available off-the-shelf, commonly used, lower cost. The whole system possessed the advantages of flexibility, user-friendliness, modular design, rapid upgrades and repairs. configurable hardware and software. The textile capacitive pressure sensors fabrication and basic performance tests were conducted. Laboratory-fabricated textile capacitive pressure sensors utilizing a sandwich architecture demonstrate several advantageous characteristics for wearable monitoring applications. These sensors exhibit straightforward fabrication processes while maintaining satisfactory measurement accuracy and repeatability across multiple testing cycles. The sensors demonstrate enhanced sensitivity performance within the low-pressure range below 50 mmHg, which is particularly relevant for physiological monitoring applications. Additionally, the sensor design incorporates power-efficient operational characteristics and rapid response times, making them suitable for real-time continuous monitoring in wearable systems. The sensor's basic performance was tested considering sensitivity, hysteresis, repeatability, the effect of temperature, and the effect of humidity, which exhibits the fabricated

sensors working conditions meet the requirements of compression garments worn on human bodies. Moreover, the multi-sensor module design is theoretically analyzed. The established smart compression garment system's applications in MetaHealth were illustrated for the purpose of delivering healthcare service to anyone at anytime at anywhere and alleviating conflicts among patients/families, doctors/nurses, hospitals/communities.

Section 3.2 describes textile captative sensor fabrication, basic performance testing, and multi-sensor module design. Section 3.3 illustrates proposed smart compression garment systems with embedded flexible sensors, edge control units, user interactive devices, and software applications. Section 3.4 illustrates the basic concept of the proposed MetaHealth. Section 3.5 provides a quick summary.

3.2. Sensors Fabrication and Testing

3.2.1. Preparation of textile sensors

Pressure is essential for compression garments. Hence textile flexible pressure sensors are significant in detecting the desired pressure, with advantages of flexibility, comfort, sensitivity, and durability. In comparison with piezoelectric pressure sensors and piezoresistive pressure sensors, capacitive pressure sensors have the advantages of simple structure, easy fabrication process, superior sensitivity, lower hysteresis, better power consumption, and stable output under constant pressure [112, 227]. The capacitive pressure sensors were fabricated with conductive woven fabrics working as two electrodes, and PDMS working as the dielectric layer.

To further improve the relative permittivity of the dielectric layer, Carbon Black powder was mixed into PDMS, and the formed dielectric layer was additionally roughed by abrasive papers [109]. Finally, the sensors were encapsulated with protective layers of thermoplastic polyurethane (TPU) and polyamide fabric on the top and at the bottom. The textile flexible pressure sensor fabrication process is illustrated in Figure 3-1.

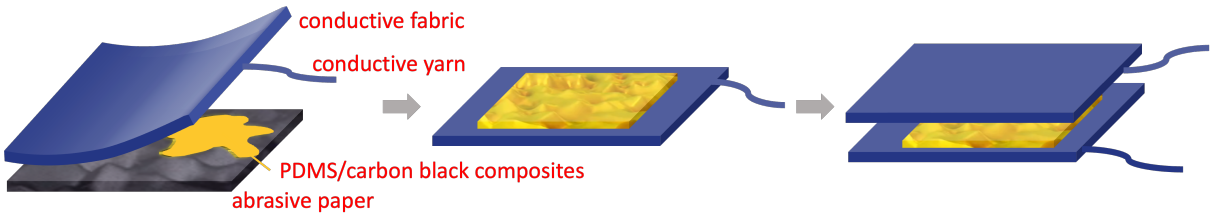

Figure 3-1 Textile capacitive pressure sensor fabrication process illustration [109].

3.2.2. Sensors performance basic testing

The performance of fabricated pressure sensors was tested through sensitivity, hysteresis, repeatability, effect of temperature, and effect of humidity, as shown in Figure 3-2. The testing machines include Instron 5944 testing machine (Instron, Norwood, USA), LCR meter (E4980A, Keysight Technologies, USA), a customized climate chamber, where under the condition of 65 % humidity, the temperature was configured to 8 different levels between 20 °C and 50 °C , with a step of 5 °C between two consecutive levels; or alternatively under the condition of 37 °C temperature, the relative humidity was configured to 6 different levels between 20 % and 100 %, with a step of 20 % between two consecutive levels.

Testing results concluded the sensitivity achieved 0.19 kPa^{-1} when the sensing ranges from 0 kPa to 10 kPa in Figure 3-2(a). The hysteresis achieved approximately 8 % when 4 kPa pressure was loaded in Figure 3-2(b). The capacitive values envelop curves were stable during 10000 cycles when 4 kPa loading pressure with the frequency of 0.1 Hz was provided in Figure 3-2(c). From 20 °C to 50 °C, the variation of the capacitive value was 11 % in Figure 3-2(d). From 20% RH to 100% RH, the capacitive values variation was 2.15 % in Figure 3-2(e). Therefore, the fabricated pressure sensors could be used on compression garments worn on human bodies [109].

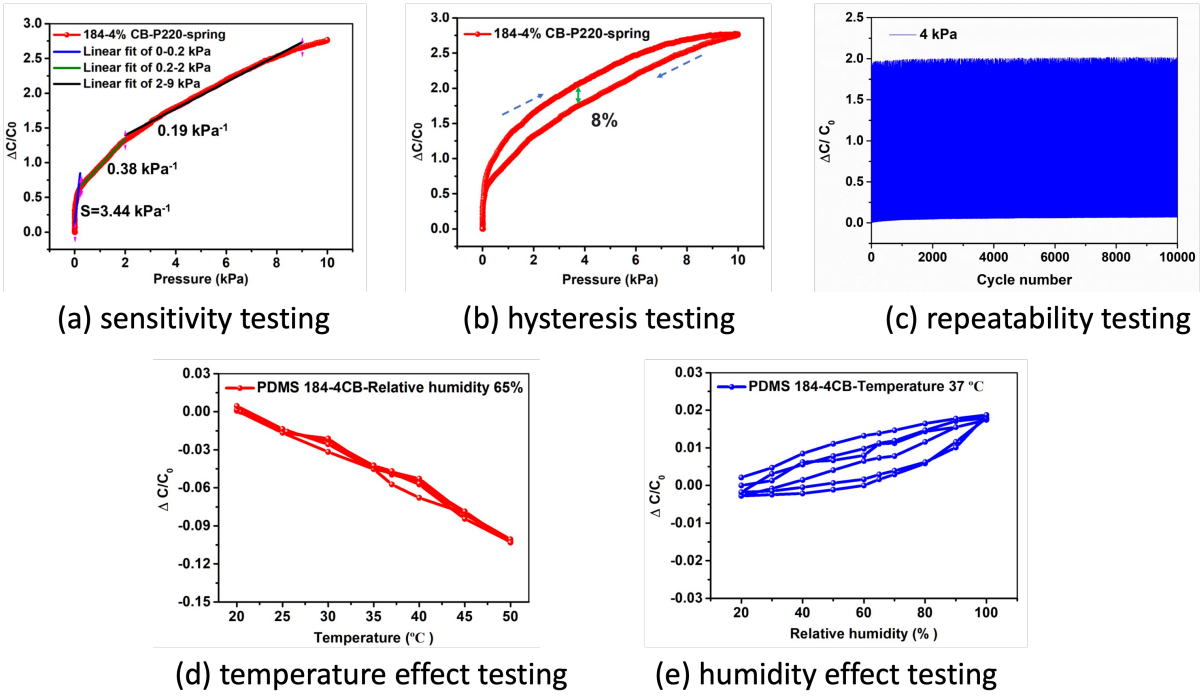

Figure 3-2 Fabricated pressure sensors performance basic testing [109].

3.2.3. Multi-sensor module design

As discussed before, the flexible pressure capacitive sensor is fabricated by using the sandwich structure, to enhance capacitive sensitivity to exerted pressure. However, different compression garments applications require different sensor sensitivity, in terms of applying on different body positions for chronic venous disease management, scar management, orthopedic application, body shaping application, sportswear application, or other applications. Instead of direct use of the small size and highly sensitive sensor named as a sensor cell, multi-sensor modules are designed, including Multi-Sensor Module A (connection in parallel), and Multi-Sensor Module B (connection in series), as illustrated in Figure 3-3.

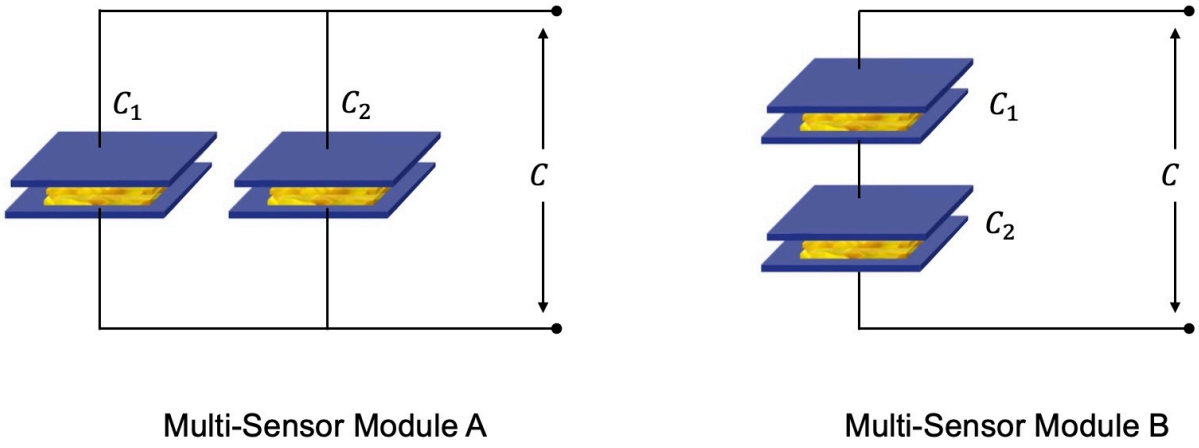

Figure 3-3 The diagram to illustrate different connection approaches for Multi-Sensor Module A and Multi-Sensor Module B.

Multi-Sensor Module A has the same sensitivity as the original capacitive sensor cell and can detect larger areas than only one sensor cell. Multi-Sensor Module B has lower sensitivity than any one sensor cell, which can attenuate pressure signals. For simplicity, it is discussed about

a module containing two original capacitive sensor cells. For Multi-Sensor Module A, the total capacitance is as

$$C = C_1 + C_2 \tag{3.1}$$

If C_1 is changed by the exerted pressure while C_2 is unchanged, the total capacitance is changed by the same value, i.e. the sensitivity is sustained.

$$\Delta C = \Delta C_1 \tag{3.2}$$

For Multi-Sensor Module B, the total capacitance is as

$$C = \frac{C_1 C_2}{C_1 + C_2} \tag{3.3}$$

Similarly, if C_1 is changed by the exerted pressure while C_2 is unchanged, the total capacitance is calculated as

$$\Delta C = \left(\frac{C_2}{C_1 + C_2}\right)^2 \Delta C_1 \tag{3.4}$$

let $C_1 = C_2$, because all sensor cells are the same, so that

$$\Delta C = \frac{1}{4}\Delta C_1 \tag{3.5}$$

which means the total capacitance is attenuated. Therefore, Multi-Sensor Module A is applied where high pressure sensitivity is desired, while Multi-Sensor Module B is applied where high pressure sensitivity is undesired.

3.3. Smart Compression Garment Systems

3.3.1. Smart compression garment systems introduction

To realize different functions of general functional compression garments intelligently and automatically, the smart compression garment system was proposed, consisting of compression garments, embedded flexible sensors, edge control units, user interactive devices, and software applications. The smart compression garment system aims to spontaneously attain pressure measures and pressure distribution for the desired positions of users. Based on the pressure information, more can be inferred, such as corresponding muscular movement, skeletal motion, human body movement, even exercise alerts and suggestions, disease treatment alerts and suggestions. Current studies focused more on fast processing and gaining direct inference on active muscular load, cruciate ligament forces, co-contraction of paired muscles, muscular and skeletal motions and positions [69-71]. However, user-centered application scenarios request more complicated hardware and software architecture and more sophisticated data processing algorithms.

With the rapid development of soft material, integration of flexible sensors and functional compression garments is feasible, achieving chemical and mechanical stability, air permeability, water washability, heat and moisture transmission, ultraviolet resistance, and even antibacterial and antivirus properties. With the dramatic advance of semiconductors and relevant electronic devices, portable, low-cost, computation-storage-intensive, low power consumption, widely compatible, easily integrative, flexibly customized hardware edge devices are available, such as customized Printed Circuit Board Assembly and personal mobile phones. With the recent decades of exploration research and implementation of machine learning, multiple tasks and modes learning, pruning, and distilling, few shots learning, domain transferring, and flexible deep neural networks can be adopted. Hence, smart compression garment systems can measure pressure data in situ conformally, store and transmit data simultaneously, and process and extract required information deeply.

3.3.2. Flexible capacitive pressure sensors integration

The pressure sensors were fabricated by the conductive elastic yarns coated with PDMS. Stacked two PDMS-coated conductive elastic yarns in cross formed a capacitive sensor, in which the conductive yarns work as electrodes and the PDMS acted as the dielectric layer. Multi-sensor modules can be utilized to change the initial capacitance and overall sensitivity. The fabricated capacitive pressure sensors exhibited a baseline capacitance measurement of approximately 16 pF under unloaded conditions. To enhance mechanical durability and operational longevity, the sensors were encapsulated using protective layers of TPU and

polyamide fabric positioned on both the upper and lower surfaces, providing improved resistance to external friction forces and mechanical strain during use.

The flexible capacitive pressure sensors, manufactured with a standardized diameter of 3 centimeters, were strategically integrated into predetermined locations within the medical compression stocking at points B, B1, and C, which were selected according to established medical compression hosiery standards, specifically following the RAL-GZ 387/1 German quality assurance guidelines for medical compression garments [228], as shown in Figure 3-4. This standardized positioning ensures consistent sensor placement and enables reliable pressure measurements at clinically significant anatomical locations.

Figure 3-4 The compression garment with a flexible pressure capacitive sensor.

3.3.3. Edge control unit

After successfully fabricating compression garments embedded with flexible capacitive pressure sensors, the development of a dedicated edge control unit became crucial to enable real-time capacitance measurement and wireless data transmission. The design process focused on key criteria, including operational safety, low power consumption, cost-effectiveness, long-term reliability, and portability.

To address these requirements, the system architecture was based on commercially available components, ensuring both reliability and ease of large-scale manufacturing. At the core of the control unit, an STM32 microcontroller was selected to coordinate system operations and manage data processing. Capacitance measurements were digitized using a PCap01 analog-to-digital converter, which is optimized for capacitive sensing applications. For wireless communication, the system integrated an nRF51802 Bluetooth low-energy processor, facilitating efficient and reliable data transfer to external monitoring devices. Power management was achieved through a TP4059 charging controller paired with a 2400mAh lithium-ion battery, supporting extended operational periods.

This integrated hardware design offers a robust and scalable platform for continuous monitoring of compression garment performance in real-world settings. The complete system architecture and technical specifications are detailed in Figure 3-5 and Table 3-1.

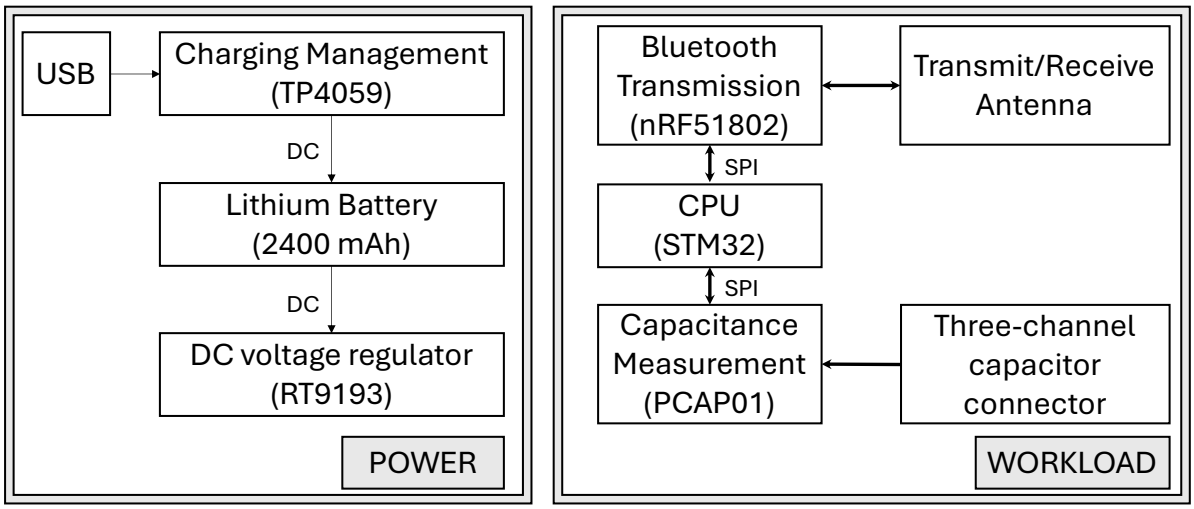

Figure 3-5 Edge control unit schematic diagram.

Table 3-1 Edge control unit circuit specification.

Module	**Specification**
Interface	USB (Power Supply/wired data communication)
	Switch On/Off
	Reset
	SWD (Debug)
	LED lights (Charging indicator)
	Capacity Measure Interface (3 channels)
Housing	3D printing (68.5*51*21.7mm)
Battery	Lithium Battery Pack (2400 mAh)
Printed Circuit Board	PCB (63*45mm, 2 layers)
USB convert to serial interface	CH340
Main Controller	STM32
Capacity Measure	PCap01
Bluetooth	nRF51802
Charging Controller	TP4059
Low-Dropout Regulator	RT9193

The proposed approach utilized PCap01Ax-0301 chips for capacitance measurement due to the capacitance values of textile sensors falling within the range of 0 to 100pF. PCap01 is a

dedicated Capacitance-to-Digital Conversion Digital Signal Processor based on complementary metal-oxide-semiconductor (CMOS) technology. This conversion principle enables high-resolution measurements with conversion times as short as 2μs. The processors offer impressive resolution capabilities, such as up to 6aF or 17-bit resolution at 5Hz. Additionally, they support a high measurement rate of up to 500kHz. The PCap01 chips provide exceptional flexibility for optimizing power consumption, delivering high resolution and fast speed. Furthermore, they are available free of charge within the chip. Data transmission can be achieved through either the serial peripheral interface (SPI) or inter-integrated circuit (I2C) connections. Notably, each PCap01 chip can simultaneously support the measurement of capacitance in three channels.

For wireless data transmission to user interactive devices, the nRF51802 module was employed, utilizing the Bluetooth Low Energy protocol. Simultaneously, it receives wired data from the STM32 microcontroller through SPI communication. The nRF51802 is a System on Chip (SoC) designed for wireless communication at an ultra-low power level of 2.4 GHz. This versatile chip offers comprehensive support for Bluetooth Low Energy and a range of proprietary 2.4 GHz protocols, such as Gazell by Nordic Semiconductor. Additionally, the nRF51802 module is equipped with communication interfaces including SPI, I2C, and universal asynchronous receiver-transmitter (UART), enabling seamless data exchange through these widely-used protocols.

The STM32F103C8T6 microcontroller serves as the main controller responsible for power supply management and data transmission management. Data flows from the PCap01 chips to

the STM32 microcontroller through SPI, and from the STM32 to the nRF51802 module also via SPI. The STM32 microcontroller integrates a robust ARM® Cortex®-M3 32-bit RISC core, delivering exceptional performance at a clock frequency of 72 MHz. Its architecture encompasses high-speed embedded memories, including a flash memory capacity of up to 128 Kbytes and a static random access memory capacity of up to 20 Kbytes. Furthermore, this microcontroller benefits a wide range of enhanced I/Os and peripherals that are interconnected via two advanced peripheral bus (APB) buses. With regards to communication capabilities, the STM32 microcontroller offers versatile interfaces, including up to two I2Cs and SPIs for serial communication, three USARTs for asynchronous serial communication, a universal serial bus (USB) interface for universal connectivity, and a CAN interface for Controller Area Network applications. These comprehensive communication interfaces empower the STM32 microcontroller to seamlessly interact with various external devices and facilitate efficient data transfer.

For power supply management, a TP4059 chip was used which can charge the chargeable lithium battery via an external USB connection. TP4059 supports maximum 600mA charging current, has positive and negative reverse connection protection, overcharging protection when the lithium battery is fully charged to 4.2V, and peripheral light emitting diode (LED) indication where green LED is on when charging and red LED is on when being charged. During the circuit working, the current for the lithium battery is regulated DC-DC to 3.3V by a low-dropout regulator RT9193, to supply power to the connected circuit. Here 2400mAh lithium battery pack was determined to satisfy the user's daily use, i.e. over 8 hours of continuous whole circuit

working and over 3 days of nonstop use. 63*45mm 2-layer printed circuit board (PCB) was utilized for its small size, low cost, reasonable layout, and good resilience to interference, as displayed in Figure 3-6.

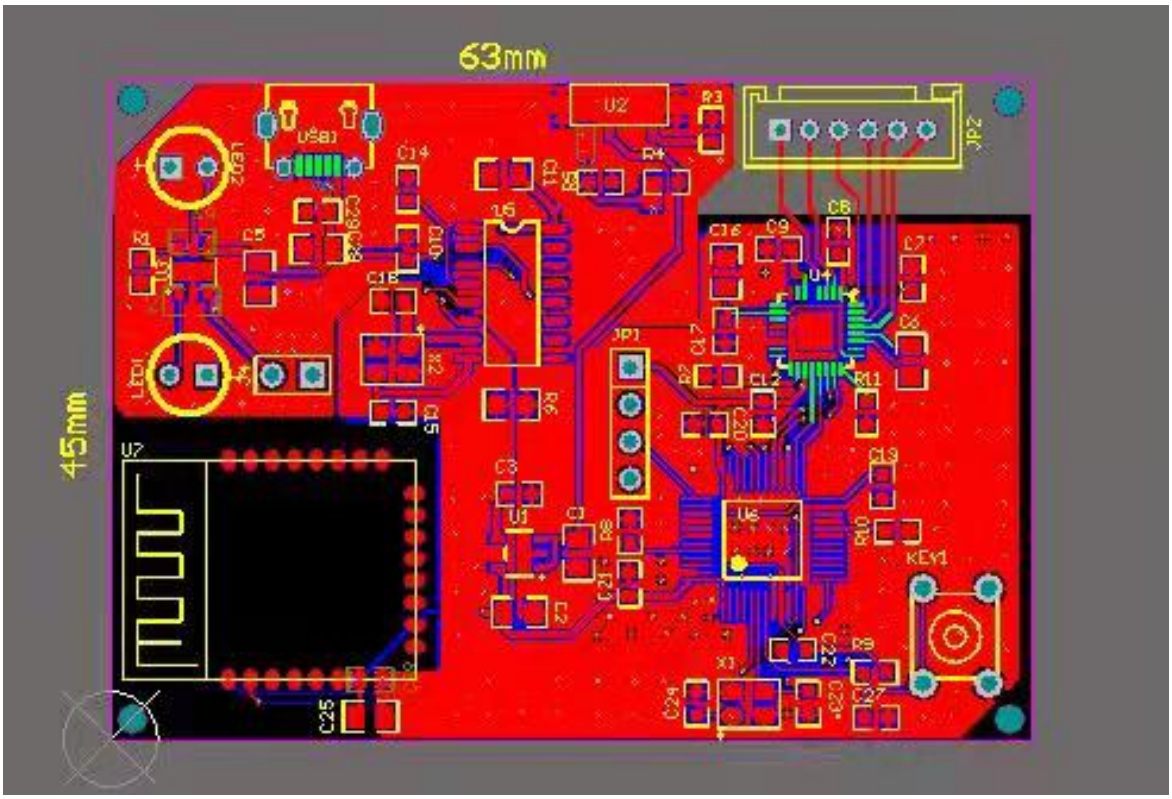

Figure 3-6 PCB layout diagram.

The housing was accordingly formed by advanced 3D printing, where chamfering was totally utilized to avoid sharp corners and minimize potential damage to wearers, as shown in Figure 3-7. The final housing case was 68.50*21.70*51.05mm with commonly used material of acrylonitrile butadiene styrene (ABS), as shown in Figure 3-8 and Figure 3-9.

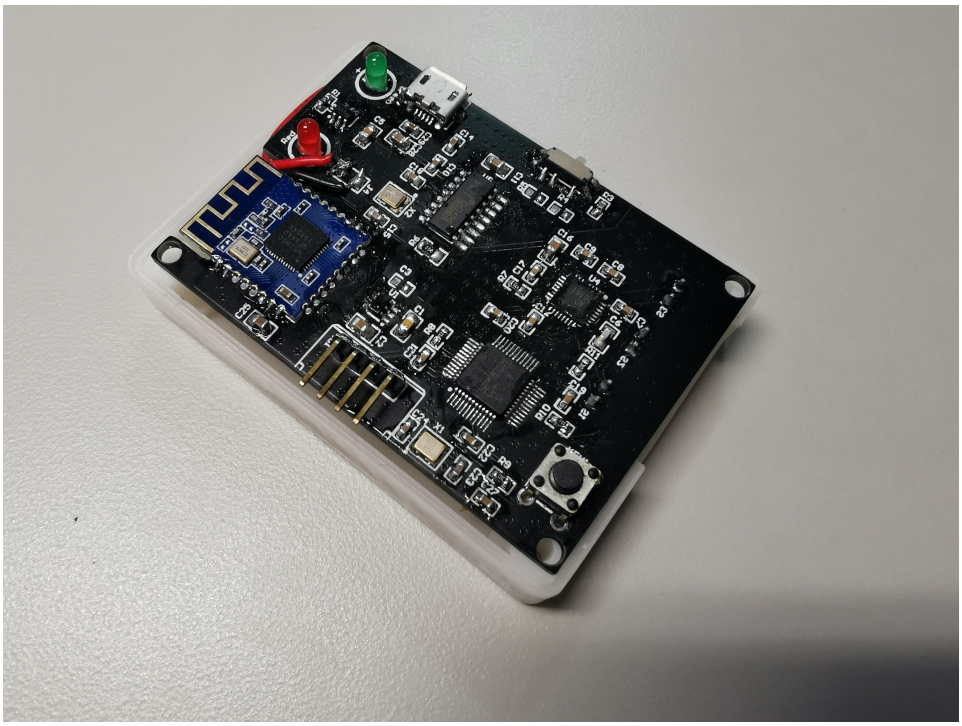

Figure 3-7 Printed circuit board assembly prototype.

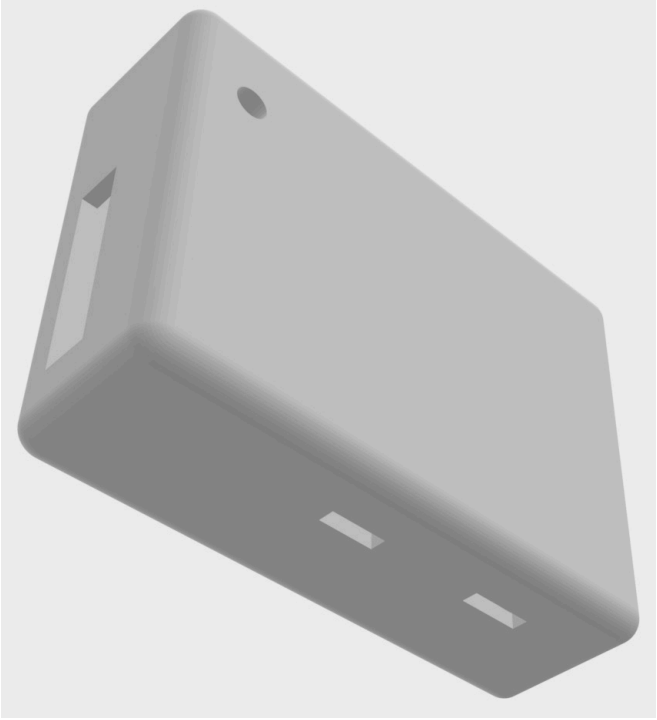

Figure 3-8 3D model housing for the edge control unit.

Figure 3-9 Final edge control unit device.

3.3.4. User interactive device and software application

As smart mobile phones are widely used in everyone's daily life, they present a powerful competition force when combining computation, storage, mobile operation system, functional applications, multimedia functionalities (music, video, camera, gaming), wireless communication, traditional phone functions (voice call, text messaging). Hence, commercial smart mobile phones were properly chosen to be user-interactive devices, which means all human interactions take place on smart phones, including information display, information extraction, danger alarm, message notification, and practice recommendation. Capacitance values captured at the frequency of 0.6667Hz by the edge control unit would be continuously wireless peer-to-peer transmitted by Bluetooth Low Energy (BLE) Bluetooth at the frequency

of 0.0167Hz to user smart phones, in order to cut down power consumption. The received data was stored in the SQLite database. Heavy computation loads, such as mapping capacitance values to pressure values, and storage were assigned to smart phones so that the edge control unit consumed less relevant resources and power. The whole system architecture is more flexible and easier to adapt, which meets the golden rules of DevOps practices and agile development. Users could conveniently read pressure values in real-time and receive healthcare notifications after the historic pressure values were analyzed on smart phones.

As Android mobile phones have rather high penetration in the consumer market, therefore, Android applications were fast developed, based on Android 8.0 architecture and compatible with above 8.0 architectures. The application, named Smart Compression Stocking Utility, was developed using Android Studio 4.1, utilizing the Java programming language for coding purposes, as shown Figure 3-10. Native mobile app development offers numerous distinct advantages. Firstly, it features superior performance. Native mobile applications directly interact with native application programming interfaces (API), eliminating the need for intermediaries like plugins and WebViews. This streamlined approach results in faster and more responsive apps compared to hybrid alternatives. Additionally, native mobile apps enjoy seamless access to essential hardware sensors such as the camera, screen, and Bluetooth.

Secondly, native mobile app development ensures a consistent look and feel. By leveraging native software development kits (SDK), developers create apps with user interfaces (UI) that

align with the platform's native design principles. This coherence enhances the user experience by eliminating any discrepancies between the operating system and application design.

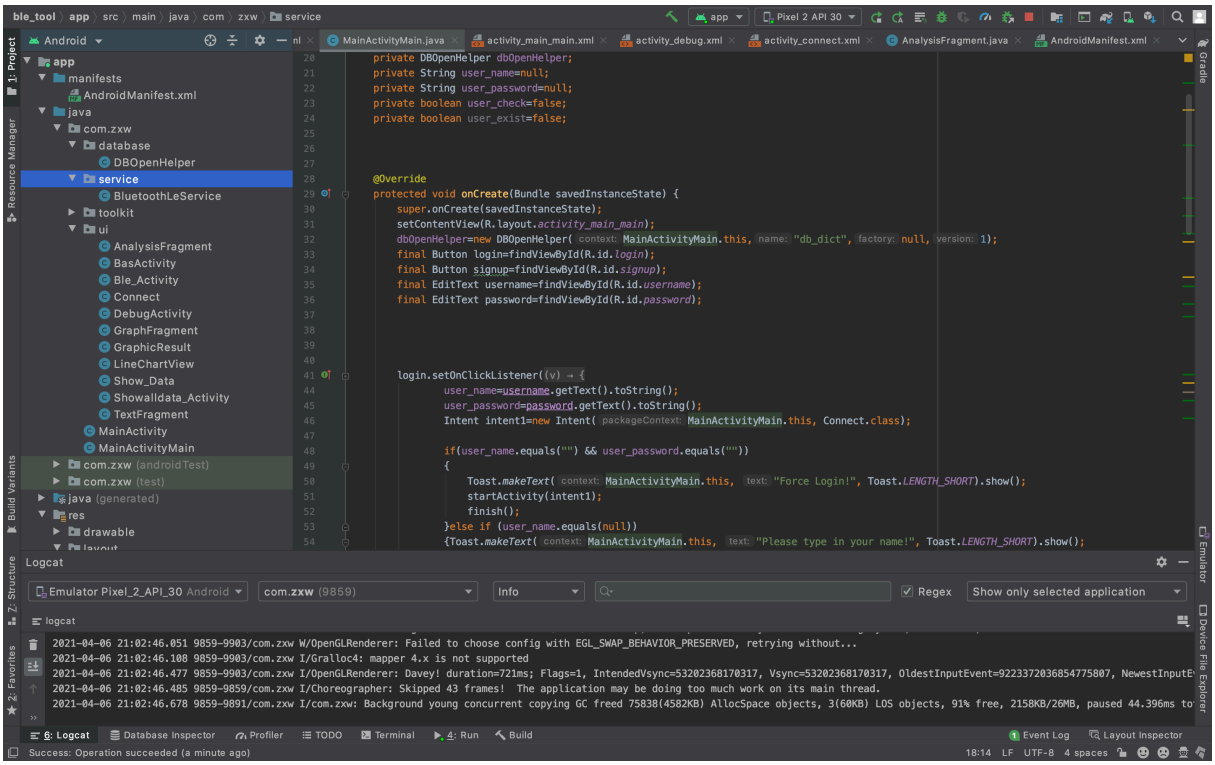

Figure 3-10 The project was developed on Android Studio.

Thirdly, native mobile apps have immediate access to new features. They can promptly leverage the latest features introduced in the Android ecosystem. On the other hand, hybrid apps reliant on web technologies must wait for plugin support to incorporate new functionalities, causing potential delays in feature adoption.

Lastly, native mobile apps exhibit better compliance with app store guidelines due to their inherent architectural properties. Given the likelihood of app stores tightening regulations on

hybrid apps, opting for native mobile app development appears more future-proof and aligned with industry trends.

User experience flew from login, scanning and finding Bluetooth devices, pairing to desired devices, and data visualization, as illustrated in Figure 3-11. Users register or login through used username and password to access the next page, as shown in Figure 3-12. Then clicking the scan button would trigger the detection of nearby Bluetooth devices, as shown in Figure 3-13. After users choose the one matching their smart compression garment system, the status would change to “connected”. Based on Android 8.0 architecture and Bluetooth protocol stack, and socket method was determined to be used to build a solid connection between mobile and Bluetooth Low Energy devices, and to use the Android native binder to implement data communication between received Bluetooth data and upper applications. Ultimately, three channels of capacitance data were converted to pressure data by the proposed algorithm and presented in graphs, texts, and analysis reports, as shown in Figure 3-14. In this way, the user could easily, clearly, and intuitively access the pressure data at B point, B1 point, C point respectively [228]. More added functions were being developed according to new emerging requirements from practical diverse users.

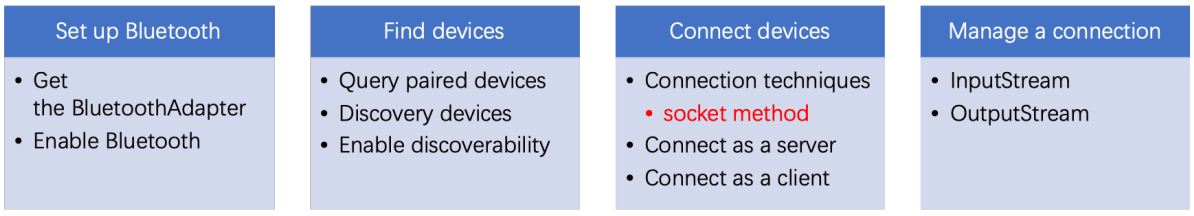

Figure 3-11 Bluetooth implementation flows on Android.

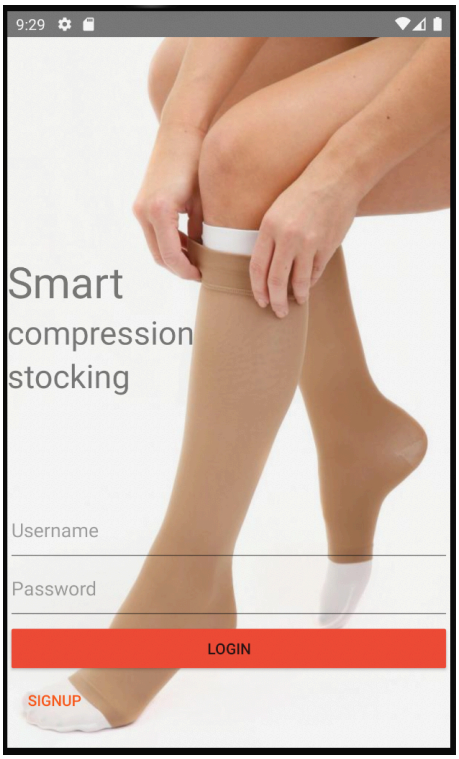

Figure 3-12 Login page of the smart compression stocking utility.

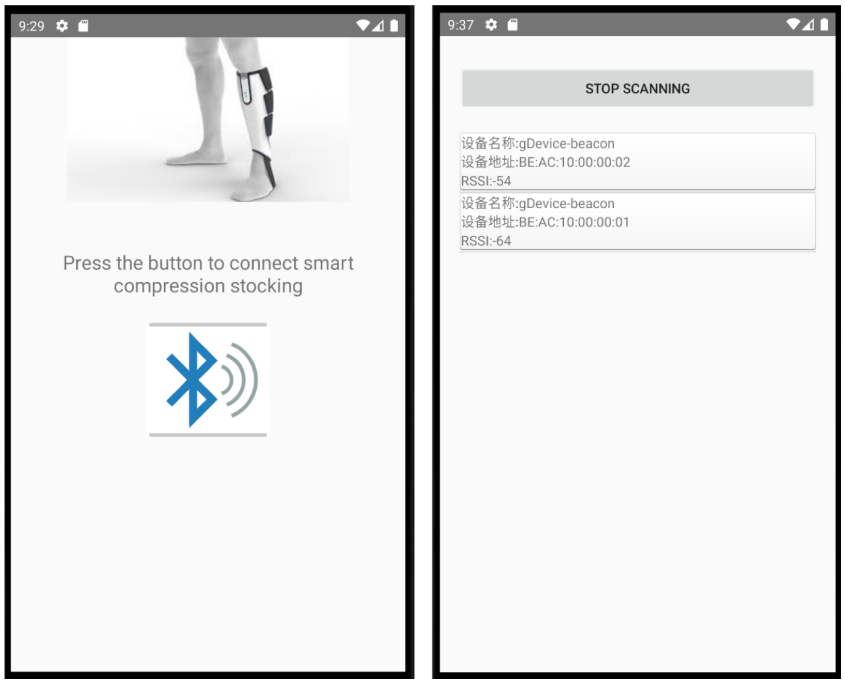

Figure 3-13 Bluetooth connection pages of the smart compression stocking utility.

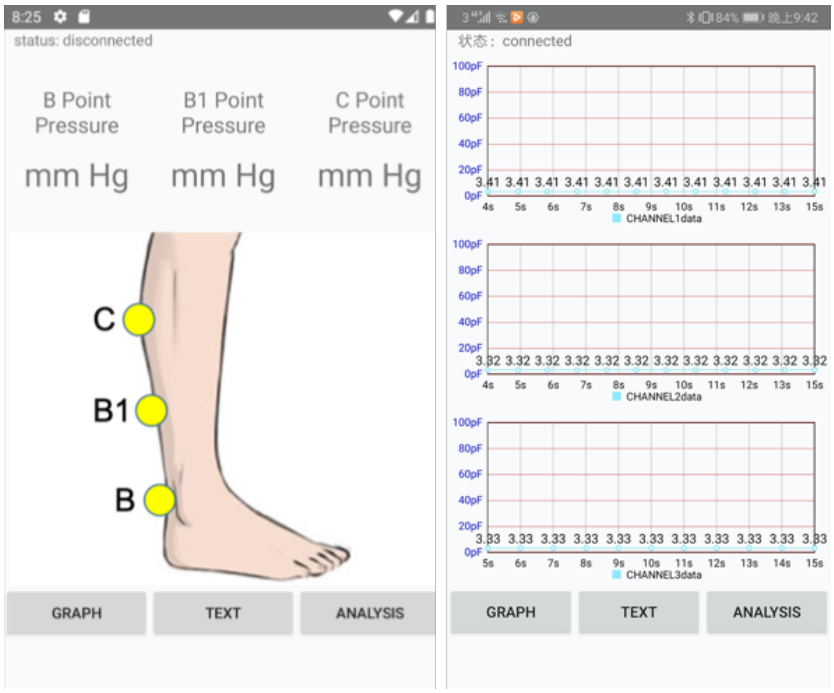

Figure 3-14 Data visualization pages of the smart compression stocking utility.

3.3.5. Data communication technologies

The progressive evolution of Internet of Things (IoT) technology has led to the emergence of numerous wireless communication technologies, particularly in recent years, owing to the extensive integration of IoT into civil and industrial domains. Presently, the predominant wireless communication technologies encompass Long Range Wide Area Network (LoRaWAN), Zigbee, WiFi, NarrowBand-Internet of Things (NB-IoT), and Bluetooth [229-231]. Each wireless communication method exhibits unique differentiations in terms of frequency band, maximum transmission distance, maximum transfer rate, network topology, security, and safety, as illustrated in Table 3-2.

Table 3-2 Comparison of different wireless communication protocols.

Communication Technology	Frequency Band	Maximum Transmission Distance	Maximum Transfer Rate	Network Topology	Safety
LoRaWAN	868MHz or 915MHz	10 kilometers	300bps to 5.5kbps	Star or Mix	AES-128
Zigbee	2.4GHz	100 meters	250kbps	Mesh	AES-128
WiFi	2.4GHz or 5GHz	100 meters	10Mbps to 1Gbps	Infrastructure or P2P	WPA2
NB-IoT	800MHz to 2.2GHz	10 kilometers	250kbps	Star	AES
Bluetooth (BLE)	2.4GHz	10 meters	1Mbps	Piconet	AES-CCM

LoRaWAN offers several noteworthy advantages. Firstly, it excels in long-distance communication, with a maximum transmission distance of up to 10 kilometers. Secondly, it demonstrates low power consumption, enabling prolonged equipment operation. Lastly, it presents a cost-effective solution, contributing to reduced manufacturing expenses for associated equipment. However, it is important to acknowledge certain limitations of LoRaWAN. Firstly, its data transmission rate is relatively low, with a maximum transmission rate of only 5.5kbps. Secondly, it lacks support for high-speed data transmission and real-time applications, thereby rendering it unsuitable for scenarios necessitating real-time response.

Zigbee exhibits several advantageous features. Firstly, it boasts low power consumption, ensuring energy-efficient operation. Secondly, it offers a substantial network capacity, accommodating a large number of connected devices. Thirdly, Zigbee enables flexible utilization of working frequency bands, enhancing adaptability in various environments. However, certain limitations are associated with Zigbee. Firstly, it presents a relatively low data transmission rate, with a maximum transmission rate of 250 kbps. Secondly, its effective range is comparatively small, accompanied by limited resistance to interference. Lastly, the Zigbee

protocol is not open source, resulting in increased complexity when integrating with the IP protocol.

WiFi presents several advantageous attributes. Firstly, it offers cost reduction as it eliminates the need for wired infrastructure during local area network (LAN) deployment. Secondly, the "Wi-Fi Certification" ensures backward compatibility, guaranteeing seamless operation of Wi-Fi standard devices across the globe. Thirdly, Wi-Fi can achieve a rather high data transmission rate, with a maximum transmission rate of 1 Gbps, which is suitable for high-volume transmission throughput applications, such as multi-media transmission. However, certain limitations should be noted with regard to WiFi. Firstly, it exhibits a limited communication distance, constraining its coverage area. Secondly, WiFi may encounter challenges related to stability and security, potentially compromising the reliability of the network. Lastly, WiFi tends to consume higher levels of power compared to other wireless communication technologies.

NB-IoT offers several notable advantages. Firstly, it provides wide coverage, allowing for communication over vast areas. Secondly, it demonstrates long battery life, enabling prolonged operation of IoT devices without frequent recharging. Thirdly, NB-IoT boasts high connection density, facilitating simultaneous connectivity of a large number of IoT devices. Lastly, it incorporates end-to-end encryption technology to ensure the secure transmission of data, safeguarding the integrity and confidentiality of information. Nevertheless, certain limitations accompany NB-IoT. Firstly, it exhibits high latency and a limited number of channels,

potentially impacting real-time communication and the capacity for concurrent data transmissions. Secondly, NB-IoT relies on existing infrastructure, which may pose challenges in remote areas or regions with limited resources and infrastructure development. Thirdly, it usually increases the operation cost, because of the data transmission charge by the Internet Service Providers.

Bluetooth possesses several advantageous features. Firstly, the manufacturing cost of Bluetooth chips and modules is relatively low, ensuring affordability and widespread integration into various electronic devices. Secondly, Bluetooth enjoys extensive support across a wide range of electronic devices, further enhancing its accessibility and compatibility. Thirdly, Bluetooth devices can be easily paired and connected without the need for intricate configurations, simplifying the user experience. Moreover, Bluetooth technology standards undergo continuous development and upgrades to optimize performance, and efficiency, and introduce new features. Lastly, Bluetooth wireless technology enables the simultaneous connection of multiple digital devices, establishing a versatile and convenient network. However, it is important to acknowledge certain drawbacks of Bluetooth. Firstly, Bluetooth wireless technologies are not as secure as some other wireless technologies, such as Wi-Fi. Secondly, Bluetooth devices are limited in terms of communication range and can only interact within a short Bluetooth range. Although Bluetooth version 5.0 offers a maximum range of approximately 100 meters, this range can be diminished by obstacles like walls or other objects. Lastly, the use of Bluetooth technology in electronic or smart devices leads to increased battery consumption due to the significant power requirements for transmitting data over short Bluetooth distances.

Compared with other IoT wireless communication protocols, BLE was ultimately determined as the main data transmission protocol between the edge control units and mobile phones, which was considered for the following reasons. Firstly, there is more than one edge control unit needed to connect a mobile phone, since plenty of smart compression garment subsystems are utilized on one person, and data from more points of interest are collected. Secondly, the communication chips or modules should be available and low cost on the market, which reduces the total research and development cost and makes it feasible to easily replace the different chips or modules. Thirdly, the communication protocol should be popular among normal people. This lowers the threshold to use the protocol, establish a network, form user habits, and complete further software application development. Fourthly, the communication cost should be as low as possible for mass population use. Finally, the data transmission rate should cover the total requirement of multi-channel smart compression garment subsystems for one person's use.

3.3.6. Cost control

One of the main hindrances of smart compression garment wide usage is that users are sensitive to the product price. On one hand, it is desired to largely improve user-friendly interfaces so that all users, especially elderly and long-term struggling patients, can naturally access functions without any obstacles, on the other hand, price-sensitive components should be replaced by off-the-shelf mass production components to reduce cost and robust supply chain in case that some components face the risk of out of stock and can be easily replaced with other

components with the same packaging. Therefore, the Android native application was developed to enhance user interactions while the hardware edge control unit was designed based on popularly used and low-cost components, and data processing algorithms by deep neural networks were adopted to complement the low performance of hardware to achieve comparative high accuracy and fast response.

According to average common prices listed on the e-commerce platform Taobao, all material costs of the edge control unit were less than 234 RMB, equivalently less than 33 USD, as shown in the bill of material cost Table 3-3. The price would definitely go down if it came to the mass production phase when the highly demanding quantity and shorter supplier chain made nonnegligible contributions.

Table 3-3 Edge control unit bill of material cost list.

Item	**Number**	**Cost (RMB)**
STM32	1	50
PCap01	1	32
nRF51802	1	30
TP4059	1	4
RT9193	1	2
CH340	1	3
2-layer PCB board	1	15
Lithium Battery (2400 mAh)	1	50
others components	1	13
Total Cost		199

3.4. Proposition of MetaHealth Applications

The information revolution brings us a digital world and leads us to enter the Metaverse era, which was recently accelerated by the COVID-19 pandemic. The pandemic consequent challenges and opportunities are enormous in terms of traditional healthcare and medical services. Health resource disparities between regions and hospitals are readily apparent and contribute to a range of challenges. These disparities manifest as inadequate equipment coverage, insufficient technical expertise, lower levels of patient satisfaction, difficulties in registration and hospitalization processes, as well as limitations in the distribution of services related to prevention, healthcare delivery, disease management, and rehabilitation. It is important to note that these disparities are particularly pronounced in underdeveloped or undeveloped regions [232]. The pandemic overwhelmingly burdened current health resources considering the outbreak of epidemic waves, lockdown at large scale, regular COVID-19 nucleic acid testing, border control and quarantine, etc. Therefore, conventional healthcare systems should embrace innovative technologies to reengineer infrastructures and procedures, with the objective of rebuilding next-generation healthcare service delivered for anyone at anytime at anywhere.

Based on emerging technologies including Virtual Reality, Augmented Reality, Mixed Reality, Extended Reality, Internet of Things, 5G, Cloud Computing, Artificial Intelligence, Blockchain, Non-Fungible Tokens, etc. the Metaverse is a complicated eco-system that is widely regarded as the potential invaluable asset but lacks in-depth academic research and real implementation. MeatHealth concentrates on applying the Metaverse to healthcare and medical services, in order to meet requirements from virtual consultation, collaborative working, surgical and

interventional cure, clinic care, medical visits, medical education, wellness and fitness, monetization through gamification, follow-up, etc. [233-236] By taking advantages of digital twin of hospitals, 3D avatars of patients/doctors/nurses, flexible sensors networks, this work proposed cost-effective MetaHealth architecture design and demonstrated some cases, in order to fulfil the golden triangle, that is to benefit patients/families, doctors/nurses, hospitals/communities, as displayed in Figure 3-15.

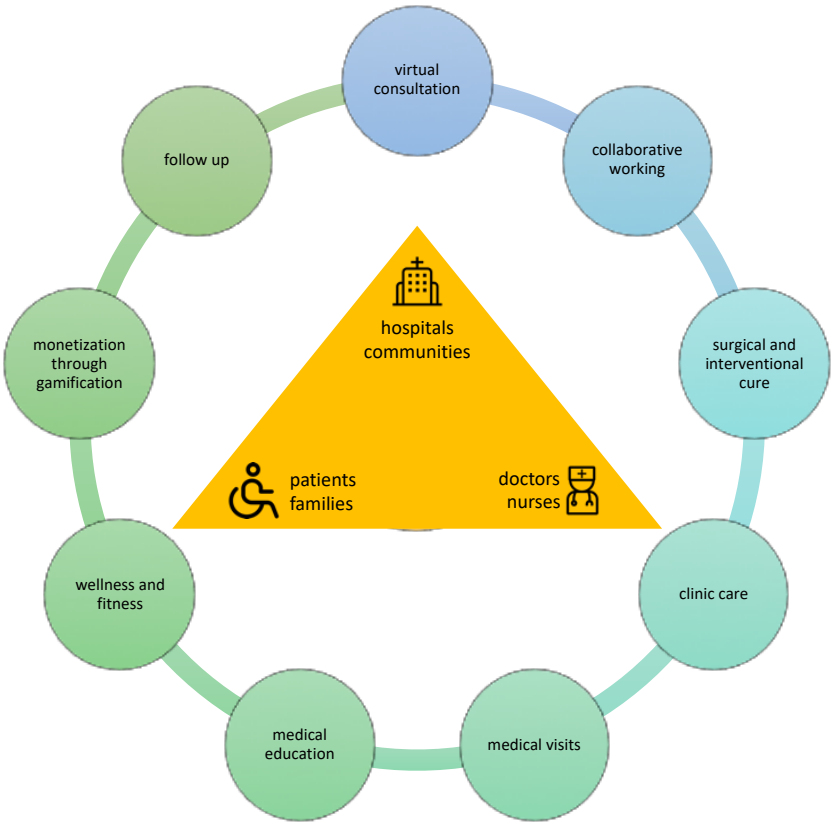

Figure 3-15 MetaHealth architecture diagram illustration.

With the fast development of deep learning, there is an obvious trend of paradigm transferring from hand-crafted features and models designed by classical signal processing, into hand-

crafted features and automatic learned models by machine learning approaches, further into completely automatic learned features and models by deep learning approaches [164]. Moreover, merging deep learning, edge computing, and flexible sensing together can lead to ubiquitous perception, ubiquitous connectivity, and ubiquitous intelligence, which makes it feasible to deliver cost-effective ubiquitous healthcare services in MetaHealth. On the one hand, flexible sensing and edge computing contribute to the easy capture of patients' biometric data with low processing latency, low network traffic load, high data security, and high personal privacy protection. On the other hand, deep learning's powerful capabilities, including automatic machine learning, high-level feature extraction, and high-level decision-making, contribute to efficient and intelligent operations around patients. Therefore, DL for Edge (Deep Learning for Optimizing Edge), DL on Edge (Deep Learning Application on Edge), DL in Edge (Deep Inference in Edge), DL at Edge (Deep Learning Training at Edge), Edge for DL (Edge Computing for Deep Learning Services) attract more and more attention from the academic and the industrial [237].

Lastly, smart textile-integrated microelectronic systems (STIMES) are utilized to realize physical person and MetaHealth interaction, which generally describes fibers based or fiber assemblies based sensors, shape actuators, displays, antennas, energy harvesters or storage devices, flexible circuit boards, memory devices, and other peripheral supportive components [238, 239]. Textile-based devices can be manufactured in various forms, including headgear, clothing, footwear, and other wearable items. These sensors possess the advantageous characteristic of easy attachment and detachment from the human body. Furthermore, they

exhibit remarkable flexibility, allowing for substantial extension, double-curvature bending, and in-plane shear simultaneously. This exceptional flexibility enables efficient structural transformation, minimizing fiber strain even when the fabric undergoes significant deformation. Moreover, these sensors demonstrate high damage tolerance, making them highly resilient and durable. Combining existing mature fabric process procedures and technologies, the above characteristics favor mass production to cut down costs and new avant-garde fashion to lead people to live in daily MetaHealth.

The established smart compression garment system would be applied to the MetaHealth's various applications. This demonstrated the feasibility of the MetaHealth platform and motivated continuous iterative improvements to deliver health service to anyone at anytime at anywhere.

3.5. Summary

In this chapter, textile capacitive pressure sensors were fabricated by using a sandwich structure, and the sensors' basic performance was tested, including sensitivity, hysteresis, repeatability, the effect of temperature, and the effect of humidity, which meet the requirements of compression garments worn on human bodies. Multi-sensor modules are designed according to different requirements from application scenarios.

The smart compression garment systems were proposed, including compression garments, embedded flexible sensors, edge control units, user interactive devices, and software applications. All electronic components were available off-the-shelf, commonly used, lower cost, including the main controller chip STM32, capacitance ADC processor PCap01, Bluetooth processor nRF51802, charging controller chip TP4059, 2400mAh lithium battery pack, so that edge control units had the bill of material (BOM) cost of 33 USD which was affordable to most potential users and can be conveniently substituted by the same packaging components. To improve user experience, Android mobiles with the developed application were recommended. Native Android application development for smart compression garment systems usage was illustrated, which could demonstrate dynamic graphs, texts, and analysis reports of real-time pressure status.

The system architecture addresses key limitations of current wearable pressure monitoring technologies by offering several technical advancements. The system exhibits heightened sensitivity for low-pressure detection, enabling precise measurement of subtle pressure variations that typically fall below the detection threshold of conventional devices. Its integrated design ensures measurement accuracy while maintaining the mechanical flexibility necessary for comfortable, long-term wear, even during dynamic movements. User experience is enhanced through intuitive interface design, facilitating seamless interaction between users and the monitoring technology. The modular architecture allows for straightforward integration with external systems, supporting compatibility with existing healthcare infrastructure and research equipment. Furthermore, the design emphasizes maintainability, enabling rapid

internal component upgrades and simplified repairs, which reduce operational costs and minimize system downtime. The system's versatile architecture supports adaptability across a range of application environments, including clinical rehabilitation, sports performance monitoring, and research. This flexibility is achieved through configurable software parameters and modular hardware components, allowing customization to meet specific measurement requirements and operational constraints in diverse use cases. These advantages will be evaluated in the following chapters to discuss about applications of proposed smart compression garment systems, for the target of realizing the proposed MetaHealth long-term platform and delivering healthcare service to anyone at anytime at anywhere.

Chapter 4 Unsupervised Encoder-Decoder for Edge Signal Processing

4.1. Introduction

This chapter introduces the signal processing challenges for the smart compression garment systems and proposes an encoder-decoder architecture to cope with them. The Laboratory-fabricated textile capacitive pressure sensors' performance is deteriorated by parasitic capacitances caused by surrounding electromagnetic interference, proximity effects, and deformation on curved surfaces. The acquired weak signals of 10^{-12} level (pF) with frequency overlapped noise and non-stationary noise in real applications. Therefore, traditional frequency filters or time-frequency analysis cannot guarantee denoise performance improvement on a large scale. Nevertheless, deep neural networks reveal a powerful capacity to deal with complex signal-processing issues. Hence, deep neural networks based encoder-decoder architecture was proposed to realize end-to-end learning and to accurately calculate corresponding pressures from fabricated capacitive sensors. Based on the experiments of flat surface pressure and curved surface pressure, resolution accuracy is largely improved, and the proposed architecture is suitable for edge computing deployment.

Section 4.2 describes traditional signal processing methods' challenges in dealing with flexible sensors and proposes a specific encoder-decoder architecture. Section 4.3 describes autoencoder design for denoise and data suppression. Section 4.4 describes the decoder design to calculate the corresponding pressure exerted on flexible sensors. Section 4.5 illustrates for curved surface situations the fabric capacitive pressure sensors demonstrate special characteristics and the proposed encoder-decoder architecture can work well to denoise and improve accuracy. Section 4.6 offers a summary of this chapter's content.

4.2. Encoder-Decoder Architecture

4.2.1. Signal processing for flexible sensors

With the fast development and research of varieties of flexible sensors, signal processing of flexible sensors should be addressed, as flexible sensors are prone to limited sensitivity, stability, and reliability which cause acquired weak signals can be easily deteriorated by contact conformal surfaces, various noise sources, motions of subjects, and other artifacts [240, 241]. Based on flexible material response properties, the signals acquired directly by flexible sensors are mostly quite tiny values smaller than 10^{-6} level or even 10^{-12} level, which therefore need integrated signal amplifiers and complicated electronic circuit design. However, this may bring more electrical noises and interferences, resulting in distorted received low SNR signals.

Filtering is widely used for its high maturity and high interpretability. It can remove low, high, band frequency noise and dense power interference in the frequency domain, resulting in limiting the processed signals to the desired bandwidth of interest. However, it requires prior

knowledge about noise and interference spectrum distribution. Moreover, if the desired signals and noise overlap in the same frequency band or noise is non-stationary, the performance of the filter will drop drastically. Traditional fast response filters, such as Wiener filters, least mean square filters (LMS), recursive least square filters (RLS), and Kalman filters, show little performance improvement on noise reduction in real applications [242, 243], because acquired signals consist of varieties of noise and interference sources which have different statistical characteristics and non-stationary properties. Moreover, well-defined synthetic noise reference signals are difficult to acquire. Hence some studies focus on complicated algorithms to deal with noise reduction. To alleviate the frequency overlap issue, some researchers used an adaptive de-noising strategy by constructing a noise generator from another noise-correlated reference signal to remove undesired artifact noise [244, 245]. This burdens the whole system's complexity and final performance is heavily dependent on the reference noise generator which also brings more noise of unknown characteristics. To alleviate the non-stationary noise, some researchers used wavelet transform and empirical mode decomposition (EMD) to perform time-frequency analysis [246-250]. However, it is difficult to select the best wavelet basis functions and EMD requires a heavy computational workload to find intrinsic mode functions.

4.2.2. Encoder decoder architecture introduction

With the development of a deep neural network, more sophisticated problems hardly solved before can be dealt with by using end-to-end learning to achieve desired accuracy. Deep learning is widely used in computer vision and natural language processing, while there is an apparent trend to penetrate more traditional physical fields, especially for basic signal

processing. There is also an obvious paradigm transferring from hand-crafted complicated data processing algorithms to general deep learning approaches which consist of data collection, data cleaning, data aggregation, model training, model testing, and model implementation. Instead of intensive labor on deriving close expressions of formula, which sometimes never explicitly exist, the current focus is to collect high-quality data and annotate large volume data. Nevertheless, considering that data annotation is costly, physical signal data is always with noise, and deep neural networks are difficult to interpret, there is still a huge gap to fuse deep learning with conventional signal processing.

Encoder decoder architecture has attracted more research attention recently. The architecture can be utilized in unsupervised learning, and sequence-to-sequence tasks, and has better interpretability and fast module adaption.

Encoder decoder architecture contains two components [164], as shown in Figure 4-1. The initial component is the encoder, responsible for receiving a variable-length sequence as input and transforming it into a fixed-shaped state representation. The subsequent component is the decoder, consisting of a stacked structure that translates the encoded state, with its fixed shape, back into a variable-length sequence. The encoder component is interchangeable with other encoders, while the decoder component is interchangeable with other decoders, only by fine-tuning the rest components.

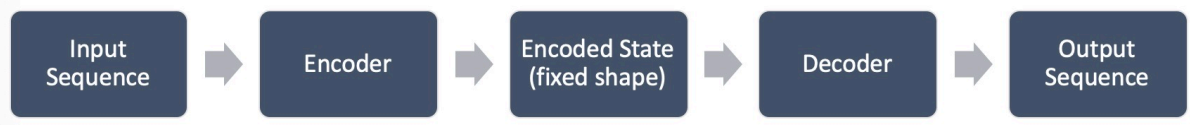

Figure 4-1 Encoder decoder architecture diagram.

It is worth noticing, that an interconnected encoded state has a predefined fixed shape (shape of vectors, size of dimensions), nonetheless input and output can be variable-length sequences, which is powerful to deal with time-series sequences. This is end-to-end learning while furthermore, the architecture allows different modules separate learning, and multi-modalities, multi-tasks, and multi-domains training of encoder or decoders which will benefit its representativeness and deeper features extraction.

The selection of appropriate encoder and decoder architectures depends fundamentally on the specific computational objectives and data characteristics of the target application. Contemporary neural network implementations commonly employ several established architectural paradigms, including Multilayer Perceptrons (MLPs) for basic nonlinear mapping tasks, Convolutional Neural Networks (CNNs) for spatial feature extraction, and recurrent architectures such as Recurrent Neural Networks (RNNs), Long Short-Term Memory (LSTM) networks, and Gated Recurrent Units (GRUs) for temporal sequence modeling.

These architectural components demonstrate versatility across diverse data modalities, supporting both unimodal and multimodal processing scenarios. The framework accommodates various input formats including textual data, audio signals, visual imagery, video sequences,

and heterogeneous physical sensor measurements. This flexibility enables the encoder-decoder paradigm to address complex cross-modal translation tasks and facilitate comprehensive representation learning across multiple domains simultaneously. The architecture has been successfully applied to complex problems in recent decades, such as image captioning [251-254], machine translation [255-258], abstract extraction [259-262], and question answering [263-266].

4.2.3. Encoder decoder architecture design

As discussed in the previous chapter, the smart compression garment system contains essential components, including compression garments, embedded flexible sensors, edge control units, user interactive devices, and software applications. The purposes are to spontaneously measure flexible pressure capacitance values and calculate corresponding pressure values and extract more information, such as users' muscular contraction and relaxation, so as to set an alarm or send recommendations.

Calculating pressure based on measured capacitance is not direct, because of the complex properties of flexible pressure capacitive sensors, such as nonlinear response, background noise, viscosity, and hysteresis. Conventional approaches are to utilize the parallel plate capacitor model.

$$\mathrm{C} = \frac{\varepsilon A}{d} \tag{4.1}$$

where C is the capacitance value, A is the contact area of two parallel conductive plates, d is the distance between the two plates, ε is the permittivity of the dielectric filled into space between the two plates. As the pressure P is exerted on the flexible sensor, ε, A, d will change accordingly. Theoretically, there are two working mechanism functions, one is to map the C space to the ε, A, d space, and the other is to map the ε, A, d space to the P space. Furthermore, considering any function can be replaced by a neural network accurately [165-168], these two functions can be equivalent to two neural networks. One neural network is named the encoder, whose job is to map input data (the C space) to codings (the implicit or explicit ε, A, d space), while the other neural network is named the decoder, whose job is to map the codings to output data (the P space).

Several aspects related to the encoder-decoder design are noteworthy. Firstly, to take advantage of temporal information because of sampling, the input of the encoder could be a time series sequence. To take advantage of spatial information because of multiple sensors, the input of the encoder could be also a sequence. Therefore, accounting for spatiotemporal information, the input is multi-dimensional vectors. Secondly, codings are at least three dimensions including ε -dimension, A-dimension, d-dimension. To enhance compatibility, encoders are interchangeable. One encoder can be trained to get the explicit ε, A, d space if possible. Other encoders can be trained to get the implicit ε, A, d space when the encoders automatically learn to extract latent representatives, such as autoencoder. Hence, codings should be a fixed shape, for instance 3-dimension vector. After the encoder is substituted, the rest decoder needs little fine-tuning work to achieve the desired results. Thirdly, the human body can be modeled as an

additive complex capacitor. Moreover, shape-changing induced by wearing compression stockings on the human body can lead to ε, A, d changing. Hence, human wearing can lead to sensors' capacitance values changing. The mechanism is more complex during human movement. Furthermore, environmental temperature and humidity have an indirect impact on sensors' capacitance values. Therefore, codings can have more dimensions to describe impact factors. Fourthly, more decoders can be used to cope with multi-task and help to enhance the learning capability of the encoder. For example, one decoder is to produce corresponding pressure values. One decoder is to classify users' posture or movement. One decoder is to detect environmental temperature and humidity.

4.3. Autoencoder

4.3.1. Autoencoder introduction

Autoencoders are widespread unsupervised machine learning approaches, that can automatically learn dense representations of input data, named as latent representations or codings compared to conventional hand-crafted features. A typical neural network contains at least three layers: an input layer, a hidden layer (encoding layer), and a decoding layer, as illustrated in Figure 4-2. The purpose of this network is to reconstruct its input, which means output data is as same as possible compared with input data so that its hidden layers learn a good representation of that input. The codings always have lower dimension representation, so autoencoders can be utilized for dimensionality reduction or data suppression. Autoencoders can automatically learn feature representation and properties with noise background so that they

are used as unsupervised pretraining of deep neural networks or data denoise. Some autoencoders are with generative models based on probability methods so that they have the capability to generate new data which is similar to the training input data with the same probability distribution.

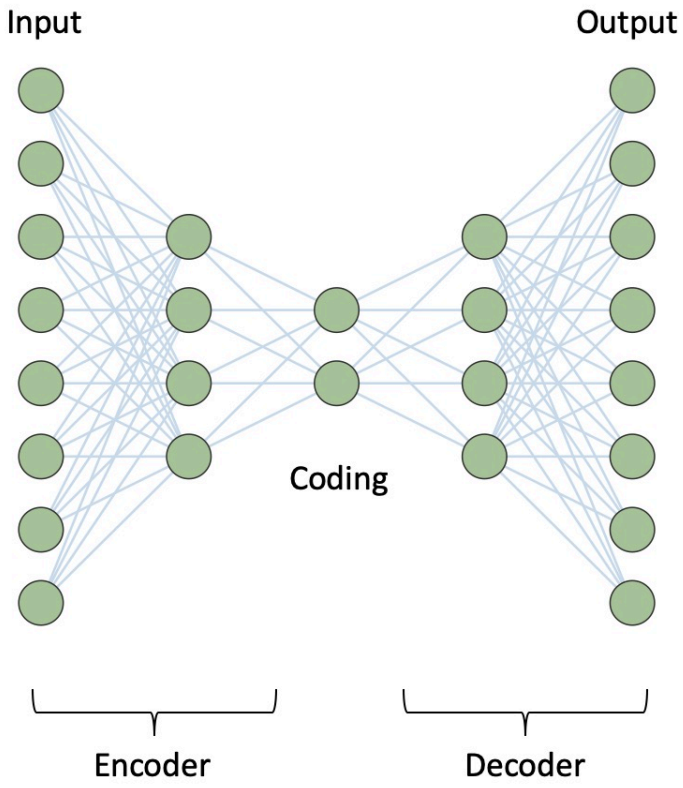

Figure 4-2 Autoencoder diagram illustration.

There are some typical autoencoder implementations [163]. If the undercomplete linear autoencoder only involves linear transformation to convert high-dimension input to lower-dimension coding and the loss function of Mean Square Error (MSE), it implements Principal Component Analysis (PCA). The stacked autoencoder involves multiple hidden layers to learn

complicated and deep features of the input data. Meanwhile, it is capable of working as unsupervised pretraining for downstream tasks such as classification, considering that data annotation is expensive and sometimes impossible. Symmetrical sandwich structures are commonly used, and furthermore tying the weights of encoder layers to symmetric decoder layers benefits training speed, parameter storage, and overcoming overfitting problems. It is also useful to train one shallow autoencoder at a time and gradually stack them to realize greedy layerwise training [267, 268]. Convolutional Autoencoders generally cope with spatial input, such as images, in order to reduce the spatial dimensionality of the inputs (height and width) and increase the depth (the number of feature maps) [269], while Recurrent Autoencoders generally cope with sequences input, such as time series or texts, in order to map variant length sequences to a fixed shape vector [270, 271]. Denoising Autoencoders (DAE) are good at denoising, by training models to recover original inputs after worsening inputs with additive noise [272, 273]. Contractive Autoencoders (CAE) are also robust to noise, by penalizing the Frobenius norm of the Jacobian matrix of the encoder with respect to the input [274]. Sparse Autoencoders (SAE) can be effectively learned by decreasing the total number of active neurons in the coding layers, which is similar to the model parameters regularization [275, 276]. In addition, Variational Autoencoders (VAE) are based on probabilistic autoencoders, which firstly map input data to codings random variables space, such as Gaussian distribution variables, and secondly reconstruct variables samples to recover original input data [277]. VAE is also based on generative autoencoders so that new samples can be generated sharing the same statistical properties of original data. Furthermore, Adversarial Autoencoders (AAE) utilize

probabilistic autoencoders and generative autoencoders, while the generative adversarial networks (GAN) method is introduced to train a discriminator [278].

4.3.2. Autoencoder design

It is difficult to directly derive a close expression to map capacitance values (the C space) to permittivity, contact area, and distance values (the ε, A, d space). One alternatively feasible solution is to utilize machine learning to automatically extract deep features of capacitance values. The deep features can be regarded as latent representatives of desired permittivity, contact area, and distance values. Furthermore, to largely reduce data annotation, autoencoders are adopted as unsupervised learning considering the input and output of autoencoders are the same raw capacitance data during training and these raw capacitance data can be easily collected under different situations, such as various pressures, wearing on human legs, human movement.

The smart compression garment system can measure the capacitance of flexible sensors with a sampling interval of 2s. The sampling rate is not high, but this meets the demands of long-term and slowly changing pressure detection of medical compression stockings, and meanwhile low sampling rate decreases hardware power consumption so that patients can conveniently use it without worrisome of frequent charging battery. To attain robust autoencoders against background noise and interference, a time series sequence of 30 elements is constructed as input data. The sequence stands for one-minute measure data. All of the input data is normalized to

achieve zero-centered and ranging from -1 to 1 so that autoencoders can converge at a small number of iterations.

$$x' = \frac{x - \frac{x_{max} + x_{min}}{2}}{\frac{x_{max} - x_{min}}{2}} \tag{4.2}$$

where x is raw data, x' is preprocessed data, x_{max} is the maximum number out of the raw data, x_{min} is the minimum number out of the raw data.

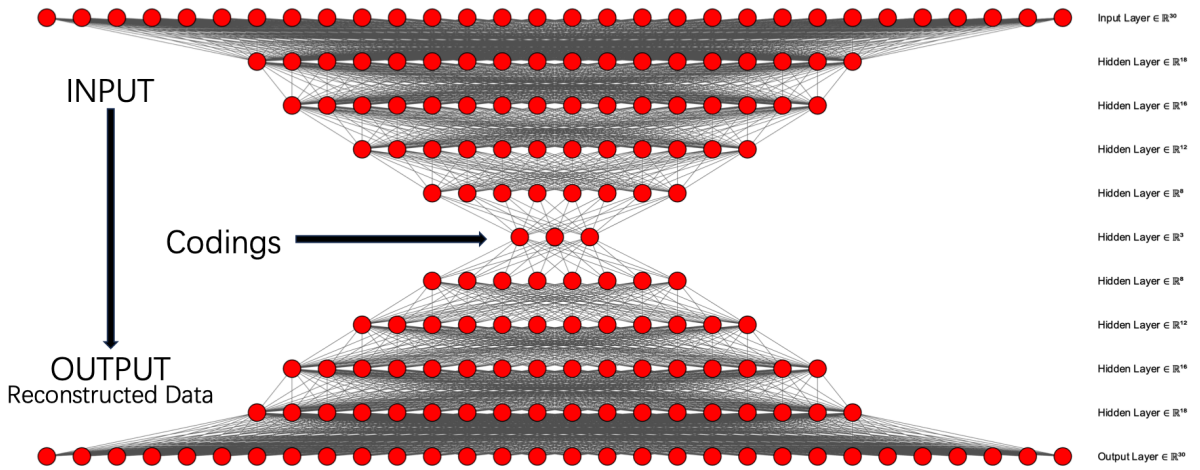

Figure 4-3 One typical autoencoder structure.

To cut down the computation load, a typical architecture of the autoencoder is stacked fully connected layers (weight matrix multiplication and with activation of the hyperbolic tangent function), with gradually decreasing encoder part neurons layer by layer until the coding layer,

and symmetrical regarding the central coding layer. It has a sandwich structure, as shown in Figure 4-3.

In the context of autoencoder models, the loss function employed is the Mean Squared Error (MSE) augmented by an L2 regularization term. This regularization term serves as a constraint on the energy of the codings, thereby influencing the model's learning process. L2 regularization, commonly referred to as Ridge regression, introduces a penalty to the loss function proportional to the square of the magnitude of the autoencoder's coding coefficients. Unlike L1 regularization, which can drive coefficients to zero, L2 regularization uniformly reduces all coefficients towards zero without necessarily nullifying them. This approach promotes a balanced contribution from each feature, mitigating the risk of any single feature disproportionately affecting the model. Such disproportionate influence can lead to overfitting, especially in scenarios where the dataset is limited and certain features may exhibit a misleadingly strong correlation with the target variable.

$$Loss = MSE + Regulation\ term = \frac{1}{n}\sum_{i=0}^{n}(y_i - \hat{y}_i)^2 + \lambda\sum_{i=0}^{m}(c_i)^2 \qquad (4.3)$$

where y_i is the output of the autoencoder. $\hat{y}_i$ is the corresponding ground truth value. n is the number of sample sizes, setting $n = 30$, because the desired input or output sequence is of 30 elements of data. c_i is the coding of the autoencoder. m is the coding dimensionality, setting

$m = 3$. λ is the weight ratio that determines the penalty impact of coding energy, so that all codings should be minimal energy. Empirically it is set $\lambda = 0.0001$.

A typical autoencoder consists of *K* layers, each layer is the fully connected layer to realize dimensional transformation with activation function:

$$y = f(Wx) \tag{4.4}$$

where $y \in R^m$, $x \in R^n$, $W \in R^m \times R^n$, $f(*)$ is the hyperbolic tangent function, which transforms input values into outputs constrained within the range of -1 to 1. This bounded output range is particularly advantageous in neural network applications, as it helps maintain stability and ensures that the activations remain within a manageable scale. To facilitate deployment on edge devices, where computational resources may be limited, the hyperbolic tangent function can be approximated using its Taylor expansion, as $\tanh(x) \approx x - \frac{x^3}{3}$. This approximation significantly reduces computational complexity, making it more feasible for real-time inference on edge control units. By employing this simplified representation, the computational burden is alleviated, allowing for efficient processing without compromising the overall performance of the model. Furthermore the layer is written as FC(n,m). A typical autoencoder is the sequential layers sandwich network including FC(30,18), FC(18,16), FC(16,12), FC(12,8), FC(8,3), FC(3,8), FC(8,12), FC(12,16), FC(16,18), FC(18,30), as depicted in Figure 4-3.

In the training of neural networks, the optimization process employed was stochastic gradient descent (SGD) [164] with a fixed learning rate of 0.001. This learning rate was intentionally chosen to enhance the model's generalization capabilities rather than merely minimizing the training loss. The stochastic nature of this optimization method arises from the random selection of mini-batches at each iteration, where the gradient of the loss function is calculated on a subset of the training data instead of the entire dataset. This randomness introduces a beneficial exploration-exploitation dynamic within the parameter space, allowing the optimizer to explore new weight configurations while simultaneously refining parameters that show promising performance.

The stochastic characteristic of mini-batch SGD sets it apart from deterministic full-batch gradient descent. Unlike full-batch methods, which follow a fixed trajectory toward a single convergence point, mini-batch SGD allows for parameter wandering within regions of low loss due to the perturbations introduced by varying mini-batch compositions. This behavior is advantageous for generalization, as averaging gradients across mini-batches reduces update variance and promotes smoother convergence dynamics. Additionally, the residual noise inherent in this process facilitates escape from sharp local minima and provides implicit regularization against overfitting.

The use of mini-batch SGD creates a training environment that exposes the network to numerous hypothetical variations of the underlying data distribution. Given that any specific training dataset represents only one realization of the true underlying distribution, these

stochastic perturbations effectively simulate exposure to alternative data manifestations, thereby enhancing the model's robustness to sampling variability.

Mathematically, the training process involves accumulating a sequence of stochastic gradient updates. After *T* optimization steps, the final parameter vector is expressed as:

$$\theta_T = \theta_0 - \eta \sum_{t=0}^{T-1} \nabla_\theta Loss(\theta_t; B_t) \tag{4.5}$$

where $\eta = 0.001$ and each gradient $\nabla_\theta \mathrm{Loss}(\theta_t; \mathrm{B_t})$ is computed on a randomly sampled mini-batch $\mathrm{B_t}$. A critical observation is that each gradient term is derived from different data subsets, leading to a sequence of parameter iterates $\{\theta_t\}$ that do not converge to a single optimum in the traditional sense. Instead, the parameters exhibit controlled oscillation within a neighborhood surrounding optima that demonstrate robustness to data variation.

This analysis suggests a fundamental reframing of neural network training. Rather than viewing training as a rigid optimization problem seeking a single optimal solution, the process is more accurately characterized as a stochastic exploration of parameter space, specifically designed to achieve robust generalization to unseen data. This perspective highlights that the apparent "noise" in stochastic training methods serves a crucial regularization function, preventing overfitting and promoting the discovery of parameter configurations that generalize effectively beyond the training distribution.

In the empirical study, firstly, it was explored the impact of hyperparameter *K*, the number of total layers, i.e. the depth of the autoencoder. Secondly, it was explored the impact of the dimensionality of coding. i.e. the width of the autoencoder.

4.3.3. Dataset preparation

A smart compression garment system was realized with embedded flexible sensors, edge control units, user interactive devices, and software applications, which are all available off-the-shelf, commonly used, lower-cost components. Then a series of standard procedures to collect data were conducted, as shown in Figure 4-4. Standard normal weights, including 0g, 1g, 2g, 5g, 10g, 20g, 50g, were put on the one fabricated flexible sensor, and corresponding pressures were recorded by using Equation (4.6).

Figure 4-4 Flat surface experiments to collect data.

$$P = \frac{mg}{s} \tag{4.6}$$

where m is the mass of the standard normal weight, $g = 9.8\,N/Kg$ is the acceleration of gravity, s is the contact area. Moreover, P is transformed into millimeters of mercury, which can match standard metrics in commercial medical compression stockings according to RAL-GZ 387/1. For each constant standard normal weight, continuous data readout for 100 minutes was recorded, considering the data fluctuation for a period. Therefore, the whole dataset consisted of 22,498 pairs of data, as depicted in Figure 4-5.

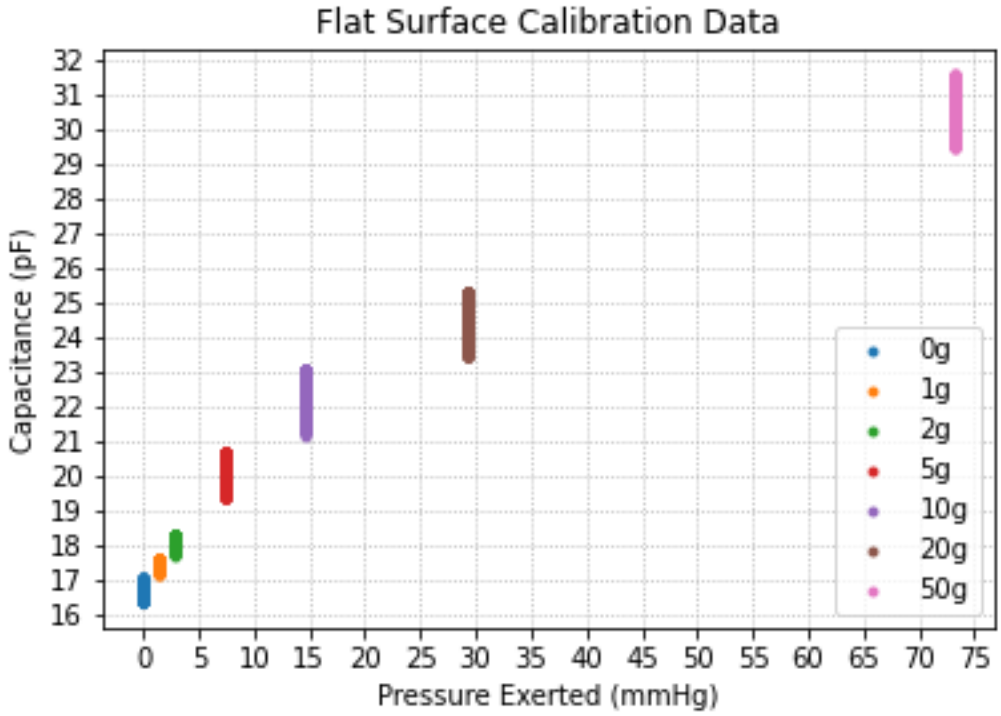

Figure 4-5 Flat surface calibration data distribution.

4.3.4. Autoencoders experiments

Each time the 30 sequential data were fed into the autoencoder for training. The autoencoder loss function was the MSE with the regulation term. The autoencoder optimization method was SGD with a learning rate of 0.001. After all of the data in the dataset were fed into the autoencoder, one epoch was finished. After 400000 epochs, the training model stops. The Root Mean Square Error (RMSE) of the output of the autoencoder and the ground truth for all of the data in the dataset was calculated, in order to measure performances of various model structures.

$$RMSE = \sqrt{\frac{1}{m}\sum_{i=0}^{m}(y_i - \hat{y}_i)^2} \tag{4.7}$$

where $m = 22{,}498$ is the total number of the whole dataset, y_i is the output of the autoencoder, $\hat{y}_i$ is the corresponding ground truth value in the dataset.

The performance of different numbers of layers for autoencoders is presented in Table 4-1 and Figure 4-6. There are some interesting findings. Firstly, as the model becomes deeper, the corresponding RMSE goes down dramatically, indicating better accuracy for data reconstruction. This proves the deeper model will learn better and extract deeper features. Secondly, as the model becomes deeper, the computation load for the model training and model inference increases, which is indicated by the number of neurons and floating point operations (FLOPs). As the model will be deployed in the embedded system on the edge control units, there is quite limited computation and memory storage in the microcontroller unit, especially

for selected cost-effective STM32. Therefore, a tradeoff between high accuracy and low model complexity is needed. Thirdly, as the model becomes deeper, the learning time becomes larger. For model 1, it takes about 150000 epochs to converge, while it takes about 340000 epochs to converge for model 4. Therefore, a tradeoff between short learning time and high model complexity is needed.

Table 4-1 Performance of different number of layers for autoencoders.

Model Name	**Model 1**	**Model 2**	**Model 3**	**Model 4**
Model Structure	FC(30,16) FC(16,3) FC(3,16) FC(16,30)	FC(30,16) FC(16,12) FC(12,3) FC(3,12) FC(12,16) FC(16,30)	FC(30,16) FC(16,12) FC(12,8) FC(8,3) FC(3,8) FC(8,12) FC(12,16) FC(16,30)	FC(30,18) FC(18,16) FC(16,12) FC(12,8) FC(8,3) FC(3,8) FC(8,12) FC(12,16) FC(16,18) FC(18,30)
Number of Neurons	95	119	135	171
Number of Layers	4	6	8	10
FLOPs	2632	3544	4008	5688
RMSE	0.5184	0.4540	0.4437	0.3956

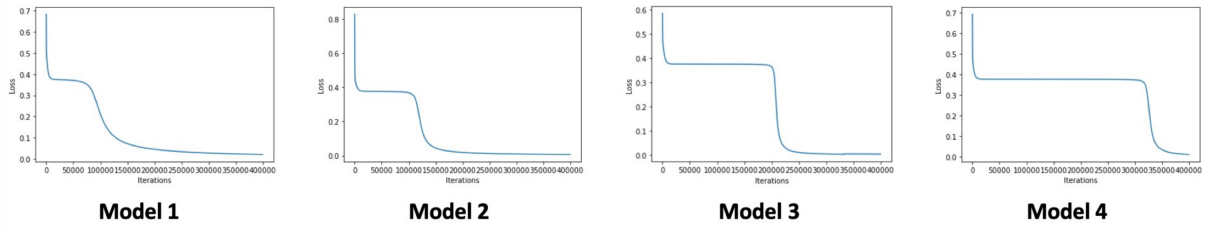

Figure 4-6 Learning curves for different number of layers for autoencoders.

Furthermore, it is important to explore the impact of the width of the model, i.e. the coding dimensionality. For simplicity, the 4 fully connected layers autoencoder models were selected to be tested and coding dimensions varied from 1 to 7, while other parts remained the same. The autoencoder loss function was the MSE with the regulation term. The autoencoder optimization was SGD with a learning rate of 0.001. After all of the data in the dataset were fed into the autoencoder, one epoch was finished. After 400000 epochs, the training model stopped. The RMSE of the output of the autoencoder and the ground truth for all of the data in the dataset was calculated, to measure performances of various model structures.

Table 4-2 Performance of different dimensions of codings for autoencoders.

Model Name	**Model a**	**Model b**	**Model c**	**Model d**	**Model e**	**Model f**
Model Structure	FC(30,16) FC(16,1) FC(1,16) FC(16,30)	FC(30,16) FC(16,2) FC(2,16) FC(16,30)	FC(30,16) FC(16,3) FC(3,16) FC(16,30)	FC(30,16) FC(16,4) FC(4,16) FC(16,30)	FC(30,16) FC(16,5) FC(5,16) FC(16,30)	FC(30,16) FC(16,6) FC(6,16) FC(16,30)
Number of Neurons	93	94	95	96	97	98
Number of Coding Dimensions	1	2	3	4	5	6
FLOPs	2488	2560	2632	2704	2776	2848
RMSE	0.5191	0.5194	0.5184	0.5111	0.5104	0.5078

The performance of different dimensions of coding for autoencoders is presented in Table 4-2 and Figure 4-7. There are some intuitive findings. Firstly, as the model becomes wider, that is coding dimensions are larger, the accuracy goes up. Secondly, the difference in accuracy increments is not obviously large, but the computation load goes up. Hence, it is reasonable to

determine coding dimensions of three, considering acceptable accuracy, high combability, and high interpretability (the latent ε, A, d space). Thirdly, learning curves for differently wide models are similar.

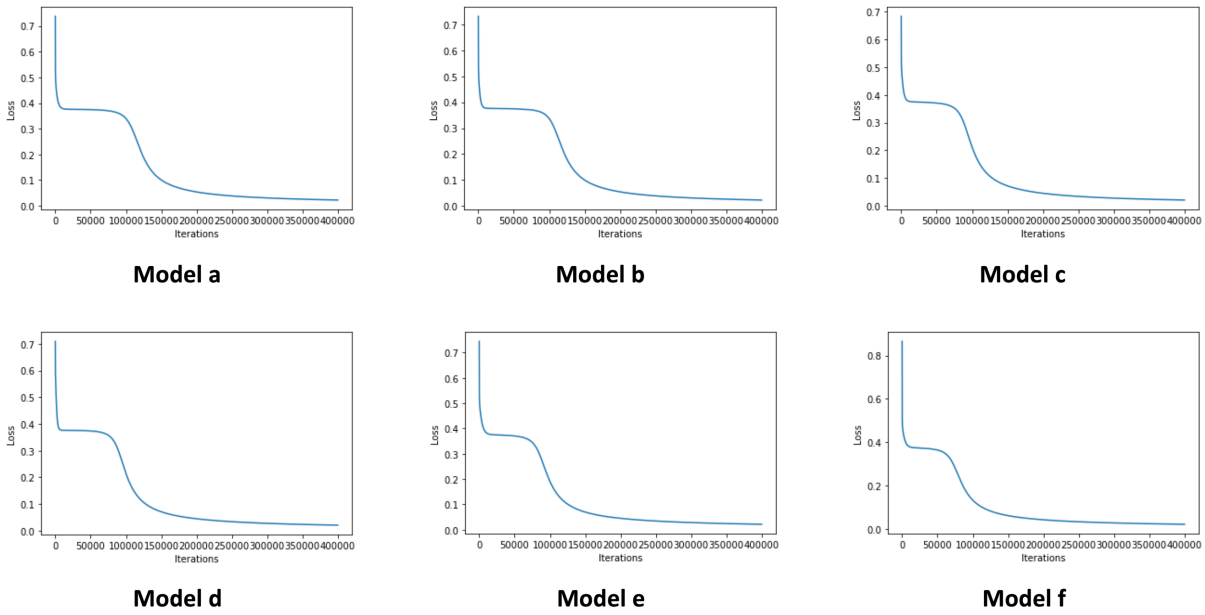

Figure 4-7 Learning curves for different dimensions of codings for autoencoders.

Moreover, the model's accuracy is impacted by the learning rates and optimization methods. Although dynamic learning rates and complex optimization methods, such as Momentum [177, 178], AdaGrad [179, 180], RMSProp [181], AdaDelta [182], and Adam [183, 184], will achieve better accuracy, the proposed method is direct and fast and can achieve robust generalization. As the performance largely relies on parameters initialization, the trained autoencoder model can work as parameters initialization and save plenty of training time.

4.4. Decoder

4.4.1. Decoder design

As the encoder-decoder architecture has been adopted and the encoder has been realized through the autoencoder approach, it is significant to design diverse decoders to realize various downstream tasks, such as to get corresponding pressure values, to detect users' posture or movement, to set an alarm or send recommendations for special situations. For simplicity, it is illustrated for the decoder to obtain spontaneous corresponding pressure.

Similarly, MLP is chosen as decoders containing sequential fully connected layers. As the codings of the autoencoder are of three dimensions, i.e. $\mathsf{C} \in R^3$, the input of the decoder is a three dimensions vector. A typical decoder contains FC(3,8), FC(8,16), FC(16,32), FC(32,64), FC(64,64), FC(64,64), FC(64,1), as depicted in Figure 4-8. Whereas the activation function was determined as Rectified Linear Unit (ReLU), mathematically defined as the maximum of zero and the input value, effectively allowing only positive inputs to pass through while setting negative inputs to zero. This choice of activation function is particularly advantageous for deployment on edge devices, where computational resources are often limited. The simplicity of the ReLU function contributes to reduced computational complexity, making it highly suitable for real-time inference on edge control units. In hardware implementations, ReLU can be efficiently realized as a comparator, which further enhances its appeal for such applications. By leveraging the straightforward nature of ReLU, the decoder can maintain high performance while minimizing the computational overhead, thereby facilitating efficient processing in

resource-constrained environments. This strategic selection underscores the importance of optimizing neural network components for specific deployment contexts, ensuring both functionality and efficiency are achieved.

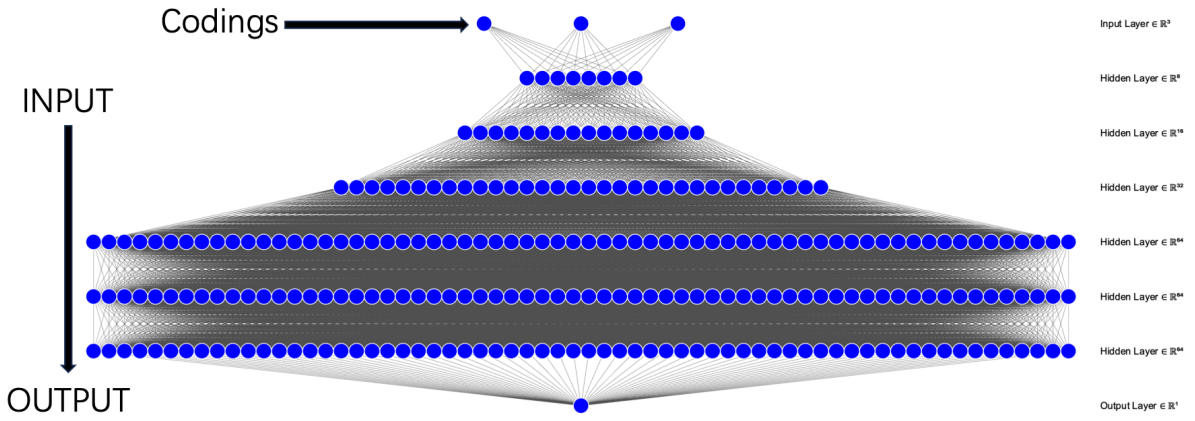

Figure 4-8 The proposed decoder structure.

Traditional polynomial calibration fits Capacitance-Pressure curves using known pressure-capacitance pairs to derive correction coefficients [279]. While higher-order polynomials and dense calibration points improve accuracy, limitations such as the Runge phenomenon and poor extrapolation hinder reliability and scalability, increasing cost and complexity. To overcome these issues, advanced techniques like Progressive Polynomial Calibration (PPC) and segmented fitting have been developed. PPC reduces computational load by updating coefficients incrementally, while segmented calibration enhances local accuracy using low-order polynomials within defined input ranges. Two-dimensional polynomial compensation further improves performance by correcting cross-sensitivity to factors such as temperature. The various polynomial calibration methods are summarized in Table 4-3. For this research,

traditional polynomial methods were adopted as benchmarks, for their balanced simplicity and flexibility, expedited computations with reduced memory demands, and extensive utilization.

Table 4-3 Illustrations of polynomial calibration methods.

Method	Description	Benefits	Limitations
Traditional Polynomial Fitting	Applying polynomial functions directly to measured capacitance-pressure (C-P) data points.	Simplicity, flexibility, relatively faster computation, smaller memory requirements.	Runge interpolation phenomenon (large errors at outer points), high number of calibration points (NCP) needed for accuracy, erroneous extrapolation.
Progressive Polynomial Calibration (PPC)	Gradually adding polynomials to compute calibration function, preserving previously evaluated coefficients.	Reduced computational load (preserves coefficients), reduced NCP, small memory footprint, simple algorithmic evaluation.	Polynomial degree can increase exponentially with steps, leading to greater computational complexity and longer processing times.
Segmented Calibration	Dividing input range into multiple sections and calculating optimized calibration functions for each.	Significantly lower overall error rate, improved accuracy by isolating distinctive regions, maintains accuracy with fewer calibration points, reduces computational complexity by allowing lower polynomial degrees within segments.	Requires careful definition of segments and handling of boundaries.
Two-Dimensional Polynomial Compensation	Extending polynomial function to two dimensions to compensate for environmental factors (e.g., temperature).	Compensates for cross-sensitivity, reduces errors due to environmental factors, enhances overall sensor system accuracy.	Increased complexity in modeling and data acquisition for multiple variables.

4.4.2. Decoder experiments

Each time the 30 sequential data were fed into the autoencoder Model 4 to obtain the codings. The codings were then fed into the decoder for training. The decoder loss function was the MSE. The decoder optimization method was SGD with a learning rate of 0.001. The dataset was shuffled and split into a training dataset with 80% of the total data and a testing dataset with 20% of the total data. After all of the data in the training dataset are fed, one epoch is finished. After 400000 epochs, the training model stopped. The RMSE of the output of the decoder and the corresponding ground truth values in the testing dataset were calculated.

For comparison, polynomial approaches were selected as baselines. Assuming the relationship between capacitance values and pressure values can be expressed as the Taylor series, it is reasonable to utilize the first-order polynomial model, second-order polynomial, third-order polynomial, fourth-order polynomial, and fifth-order polynomial. The parameters were obtained by the least squares method using a training dataset. The RMSE of distinct polynomial models produced values and the corresponding ground truth values in the testing dataset were calculated.

Table 4-4 Performance of the proposed decoder and polynomial models.

Model Name	**Encoder**	**Decoder**	**Polynomial Degree 1**	**Polynomial Degree 2**	**Polynomial Degree 3**	**Polynomial Degree 4**	**Polynomial Degree 5**
Model Structure	FC(30,18) FC(18,16) FC(16,12) FC(12,8) FC(8,3)	FC(3,8) FC(8,16) FC(16,32) FC(32,64) FC(64,64) FC(64,64) FC(64,1)	$y = ax + b$	$y = ax^2 + bx + c$	$y = ax^3 + bx^2 + cx + d$	$y = ax^4 + bx^3 + cx^2 + dx + e$	$y = ax^5 + bx^4 + cx^3 + dx^2 + ex + f$
Number of Neurons	336		2	3	4	5	6
FLOPs	24920		2	5	8	11	14
RMSE	0.7891		6.4231	1.895	1.8081	1.2754	1.9224

The performance comparisons of different approaches are summarized in Table 4-4. There are some intuitive findings. Firstly, the higher the order of polynomial models, the higher the accuracy of the model. Nonetheless, the best accuracy model is the fourth-order polynomial model. After that, the higher the order of polynomial models, the lower the accuracy of the model. There is a plausible reason that a much higher-order polynomial model is overfitted to the training dataset. Secondly, the accuracy of the neural network decoder outperforms all

polynomial models. Thirdly, the high accuracy of the neural network decoder is at the cost of higher model complexity, indicated by the total number of parameters and computation complexity (FLOPs).

Table 4-5 Performance of different fine-tuning models.

Model Name	**Encoder (Model 1) + Decoder**	**Encoder (Model 2) + Decoder**	**Encoder (Model 3) + Decoder**	**Encoder (Model 4) + Decoder**	**Polynomial Degree 4**
Model Structure	FC(30,16) FC(16,3) FC(3,8) FC(8,16) FC(16,32) FC(32,64) FC(64,64) FC(64,64) FC(64,1)	FC(30,16) FC(16,12) FC(12,3) FC(3,8) FC(8,16) FC(16,32) FC(32,64) FC(64,64) FC(64,64) FC(64,1)	FC(30,16) FC(16,12) FC(12,8) FC(8,3) FC(3,8) FC(8,16) FC(16,32) FC(32,64) FC(64,64) FC(64,64) FC(64,1)	FC(30,18) FC(18,16) FC(16,12) FC(12,8) FC(8,3) FC(3,8) FC(8,16) FC(16,32) FC(32,64) FC(64,64) FC(64,64) FC(64,1)	$y = ax^4 + bx^3 + cx^2 + dx + e$
Number of Neurons	298	310	318	336	5
FLOPs	23392	23848	24080	24920	11
RMSE	0.9266	0.9024	0.9149	0.7891	1.2754

Furthermore, it is valuable to explore the generalization capability of the proposed decoder. The autoencoder part was substituted by frozen Model 1, Model 2, Model 3, respectively, when the decoder structure remained the same and parameters initialization was from the trained decoder. The learning rate was changed to 0.1. After 1000 epochs, the training model stopped. The RMSE for the testing dataset was calculated. The performances of the fine-tuning with little computation loads are summarized in Table 4-5. All the fine-tuned models' accuracies

outperform the best of the polynomial models, which proves that the trained model is capable of generalization for different autoencoders and offers well parameters initialization which can largely cut down the fine-tuning relearning time.

4.5. Encoder-Decoder for Curve Surface Calibration

4.5.1. Curve surface experiments design

For the purpose of applying the flexible capacitive pressure sensors to human bodies, where conformable contact is achieved, it is important to do calibration on curved surfaces. The calibration experiment was designed as the following.

Firstly one medium-sized wooden mannequin leg was adopted, Secondly, the flexible sensor sample was attached to the B position, B1 position, C position on the wooden leg, where the B position is related to a circle surface with a diameter of 72mm, B1 position is related to circle surface with a diameter of 91mm, C position is related to circle surface with a diameter of 115mm. Thirdly, one sphygmomanometer (type A mercury sphygmomanometer, Yuwell, China) was used to tightly wrap the sensor on the leg and to exert different pressure levels, including no pressure, 10 mmHg, 20 mmHg, 30 mmHg, 40 mmHg, 50 mmHg, 60 mmHg pressure respectively. Fourthly, under each pressure level, the capacitance values are recorded for continuous 12 minutes, as shown in Figure 4-9.

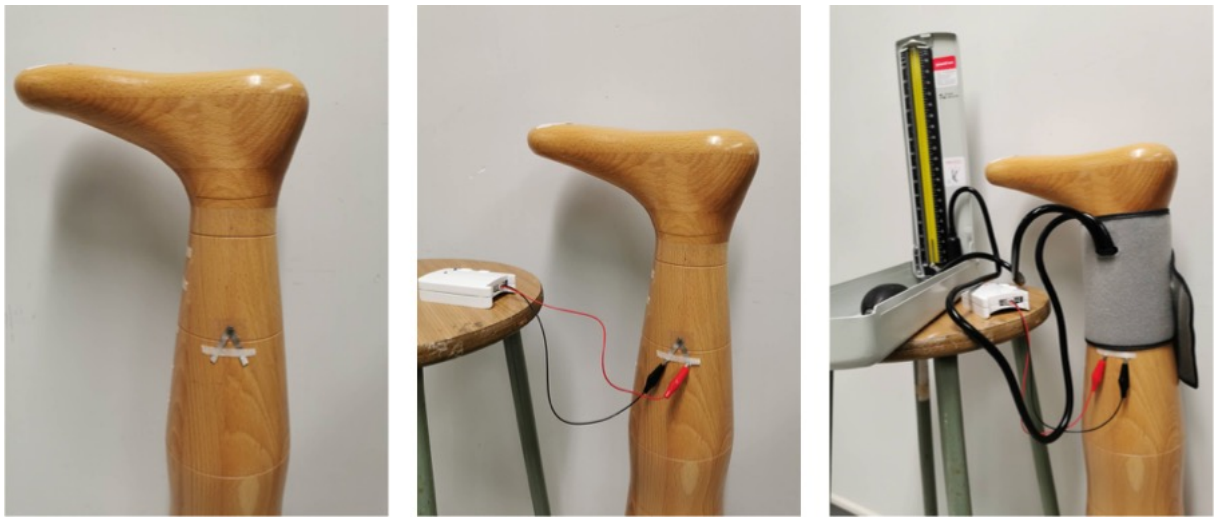

Figure 4-9 Curve surface experiment procedures (on the B1 position).

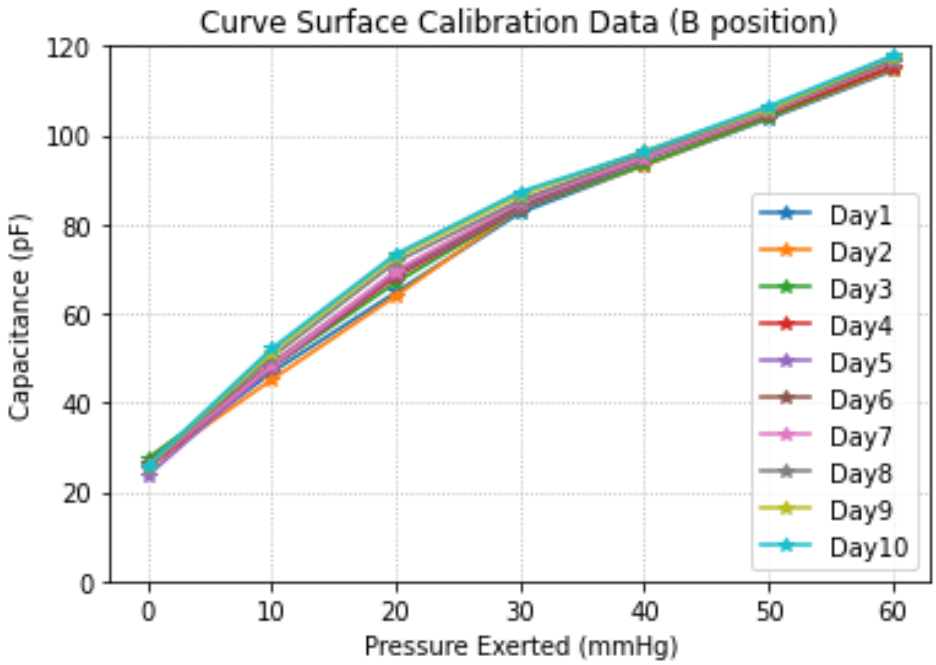

Figure 4-10 Curve surface calibration data distribution (B position).

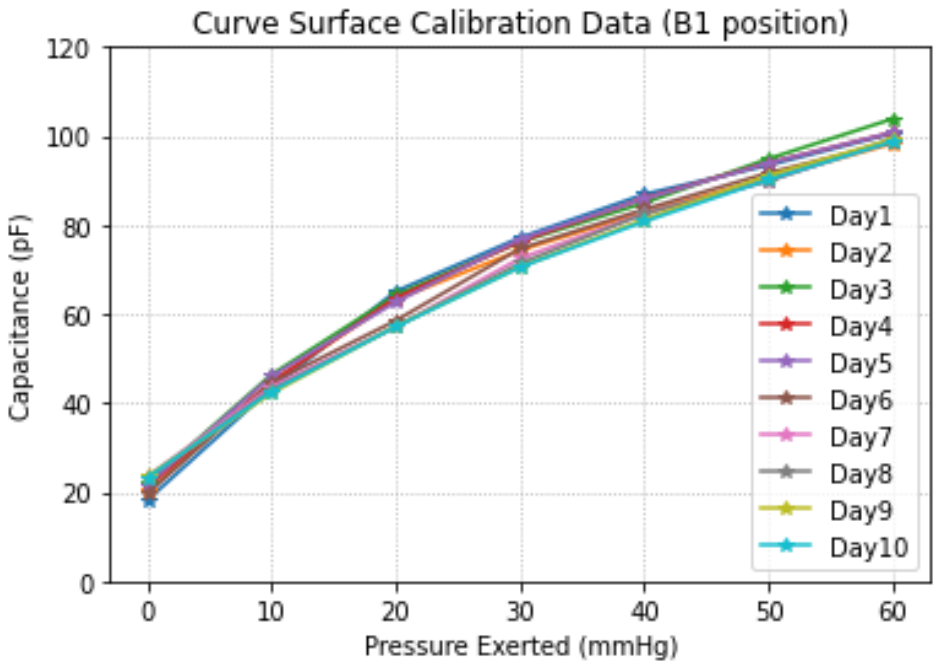

Figure 4-11 Curve surface calibration data distribution (B1 position).

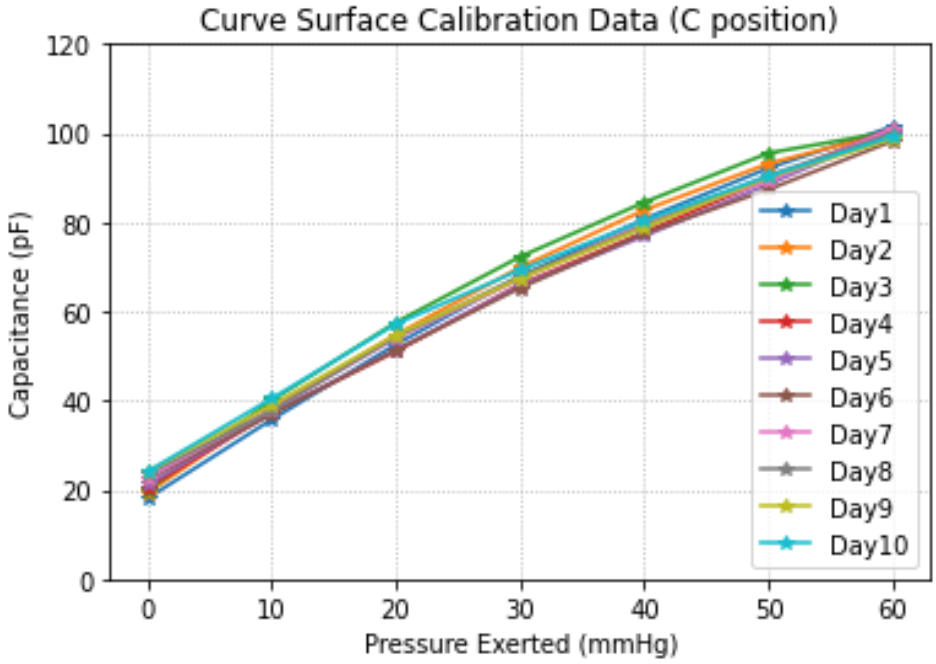

Figure 4-12 Curve surface calibration data distribution (C position).

A flexible sensor sample was used to conduct 10 days of curve surface experiments. Hence, the dataset of 75,888 pairs (capacitance vs pressure) was collected. Under each pressure level in a day, the average capacitance value was calculated. The final different curve surface calibration data was plotted in Figure 4-10, Figure 4-11 and Figure 4-12. There are interesting findings. Firstly, without pressure exerted, the initial capacitance value remains approximately 20 pF for different curvature surfaces. Secondly, under the same pressure exerted and on the same curvature surface, the capacitance values have little fluctuation and keep a good consistency. Thirdly, under the same pressure exerted, different curvature surfaces lead to different sensitivities. The higher curvature induces a higher sensitivity.

4.5.2. Curve surface encoder-decoder experiments

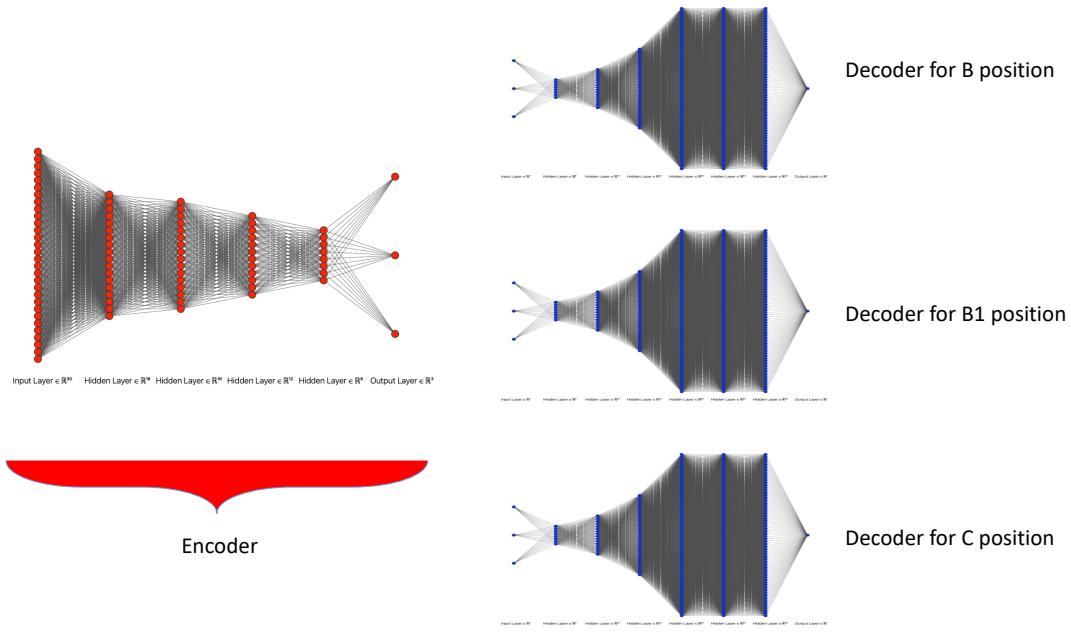

Figure 4-13 Curve surface encoder-decoder architecture.

Table 4-6 Performance of the proposed encoder-decoder and polynomial models on the B position curve.

Model Name	**Encoder** (autoencoder)	**Decoder**	**Polynomial Degree 1**	**Polynomial Degree 2**	**Polynomial Degree 3**	**Polynomial Degree 4**	**Polynomial Degree 5**
Model Structure	FC(30,18) FC(18,16) FC(16,12) FC(12,8) FC(8,3)	FC(3,8) FC(8,16) FC(16,32) FC(32,64) FC(64,64) FC(64,64) FC(64,1)	$y = ax + b$	$y = ax^2 + bx + c$	$y = ax^3 + bx^2 + cx + d$	$y = ax^4 + bx^3 + cx^2 + dx + e$	$y = ax^5 + bx^4 + cx^3 + dx^2 + ex + f$
Number of Neurons	87	252	2	3	4	5	6
FLOPs	24920		2	5	8	11	14
RMSE	0.0283		3.6445	1.3806	1.3508	1.3533	1.3464

Table 4-7 Performance of the proposed encoder-decoder and polynomial models on the B1 position curve.

Model Name	**Encoder** (autoencoder)	**Decoder**	**Polynomial Degree 1**	**Polynomial Degree 2**	**Polynomial Degree 3**	**Polynomial Degree 4**	**Polynomial Degree 5**
Model Structure	FC(30,18) FC(18,16) FC(16,12) FC(12,8) FC(8,3)	FC(3,8) FC(8,16) FC(16,32) FC(32,64) FC(64,64) FC(64,64) FC(64,1)	$y = ax + b$	$y = ax^2 + bx + c$	$y = ax^3 + bx^2 + cx + d$	$y = ax^4 + bx^3 + cx^2 + dx + e$	$y = ax^5 + bx^4 + cx^3 + dx^2 + ex + f$
Number of Neurons	87	252	2	3	4	5	6
FLOPs	24920		2	5	8	11	14
RMSE	0.0633		4.3389	1.9887	1.9342	1.9377	1.9386

Table 4-8 Performance of the proposed encoder-decoder and polynomial models on the C position curve.

Model Name	**Encoder** (autoencoder)	**Decoder**	**Polynomial Degree 1**	**Polynomial Degree 2**	**Polynomial Degree 3**	**Polynomial Degree 4**	**Polynomial Degree 5**
Model Structure	FC(30,18) FC(18,16) FC(16,12) FC(12,8) FC(8,3)	FC(3,8) FC(8,16) FC(16,32) FC(32,64) FC(64,64) FC(64,64) FC(64,1)	$y = ax + b$	$y = ax^2 + bx + c$	$y = ax^3 + bx^2 + cx + d$	$y = ax^4 + bx^3 + cx^2 + dx + e$	$y = ax^5 + bx^4 + cx^3 + dx^2 + ex + f$
Number of Neurons	87	252	2	3	4	5	6
FLOPs	24920		2	5	8	11	14
RMSE	0.0387		2.4482	1.5721	1.5568	1.5561	1.5563

As discussed before, the same encoder-decoder architecture with the same hyperparameters design is utilized. All curve surface calibration data are fed into the encoder part through autoencoder training. The different curvature datasets are used to train different decoders respectively. Hence, it is obtained a unified encoder and distinct decoders (the decoder for the B position, the decoder for the B1 position, and the decoder for the C position), as shown in Figure 4-13.

Similarly, the curve surface datasets are split as 80% for training decoders and 20% for testing the model performances. The polynomial approaches are determined as baselines, including the first-order polynomial, second-order polynomial, third-order polynomial, fourth-order

polynomial, and fifth-order polynomial, by least square (LS) training to gain all parameters. The RMSE is utilized to compare between performances of the proposed encoder-decoder architecture and the polynomial approaches. The results are summarized in Table 4-6, Table 4-7 and Table 4-8.

There are some intuitive findings. Firstly, the higher order of polynomial models can lead to the higher accuracy of the model, while, nonetheless, the best accuracy model is the third-order polynomial and the fourth-order polynomial model for the B1 position curve and C position curve respectively, considering a plausible reason that much higher order polynomial model is overfitted to the training dataset. Secondly, the accuracy of the neural-network based decoder outperforms all polynomial models, improving accuracy by 98%, 97%, 98%, for B position, B1 position, C position respectively. Thirdly, the high accuracy of the neural network decoder is at the cost of higher model complexity, indicated by an undetermined total number of parameters and FLOPs.

4.6. Summary

In this chapter, considering that the flexible capacitive pressure sensors output weak signals, approximately pF level, and are easily deteriorated by various noise and interference, and additionally the noise and interference frequency overlap with signals and are non-stationary, therefore, traditional frequency filters cannot improve denoise performance by large scale, while reference noise generators or wavelet transform or EMD cause the complexity and

computing workload of the system. Deep neural-network based encoder-decoder architecture was proposed, considering its better interpretability and higher learning capacity. An unsupervised autoencoder was used to map capacitance time series values to latent representatives of permittivity, contact area, and distance values. The depth of neural networks will largely enhance learning output accuracy, while the width of neural networks has little impact on accuracy. Furthermore, by joining the neural network decoder, the algorithm can map capacitance time series values to exerted pressure. The proposed algorithm improves the resolution accuracy by 38%, compared with the polynomial fitting algorithm. Finetune learning can be reduced to 1000 epochs after changing the encoder parts. The algorithm computing workload is also acceptable for edge deployment. For the curve surfaces, the fabric capacitive pressure sensors demonstrate good long-term consistency of data readout, and the higher sensitivity is related to the higher curvature. The proposed encoder-decoder algorithm can achieve higher performance of denoise and improve accuracy by 98%, 97%, 98%, for the B position, B1 position, C position respectively.

In all, the algorithm can work well for the denoise task for fabric capacitive pressure sensors, no matter whether the pressure is exerted on a flat surface or curved surface. The algorithm takes advantage of simple and symmetric encoder-decoder fully connected neural network architecture. The unsupervised autoencoder method reduces the human labor to label data and saves the relevant cost. The algorithm benefits less amount of computing and storage resources, compared with other deeper neural networks and more complex architecture, such as the transformer method [280] or diffusion method [281, 282]. Hence, the algorithm is suitable to

deploy on the edge devices to accelerate the signal processing speed. Furthermore, the algorithm can be implemented on embedded systems, such as Field Programmable Gate Array (FPGA) or Digital Signal Processor (DSP), to drastically enhance the processing speed at the lower physical layer.

Chapter 5 Application for Monitoring Skeleton Muscle Force of Lower Extremities

5.1. Introduction

This chapter explores the innovative application of a smart compression garment system designed for the monitoring of skeletal muscle force in the lower extremities. Continuous monitoring of these muscles is crucial, as they play a vital role in numerous daily activities, including balance maintenance, standing, walking, running, and jumping. Traditional methods such as electromyography and physiological cross-sectional area assessments face significant challenges in acquiring precise, real-time data from the human body, often neglecting the aspect of user comfort in wearable technology.

In response to these challenges, this chapter leverages the rapid advancements in fabric-based sensor technology to propose an integrated smart compression stocking system. This system comprises compression garments embedded with fabric capacitive pressure sensors, an edge control unit, a user-friendly mobile application, and a cloud-based backend. The chapter provides an in-depth discussion of the architecture pipeline design and the selection of components, emphasizing a comprehensive, user-centered design approach known as STIMES (Smart Textile Integrated Microelectronic Systems).

To validate the system, clinical experiments were conducted with 12 healthy young participants who performed maximum voluntary isometric contractions of ankle plantarflexion. Data were concurrently collected using both the smart compression stocking system and a standard muscle force measurement device, the Humac NORM. The results demonstrated a strong linear relationship between muscle torque and the system's readouts, with correlation coefficients exceeding 0.92.

Further analysis using a two-way analysis of variance (ANOVA) revealed that variations in ankle angles ($p = 0.055$) had a more significant impact on the results than differences between participants ($p = 0.290$). These findings suggest that the integrated smart compression stocking system is a viable tool for monitoring muscle force in the lower extremities, particularly in isometric conditions.

Section 5.2 describes the proposed smart compression garment system upgrade, including architecture pipeline design, fabric sensors, edge control units and user interface preparation, cloud backend design, deployment, and integration. Section 5.3 describes the clinical experiments design, including participants and experimental protocol, test protocol of maximum voluntary isometric contraction, clinical experiments data collection, and preprocessing. Section 5.4 analyzes the clinical experiment results and discusses the outcome. Section 5.5 provides a summary of this chapter.

5.2. Smart Compression Garment System Upgrade

5.2.1. Background review

Continuous monitoring of the gastrocnemius muscles is essential for facilitating various human activities, including balance maintenance, standing, walking, running, and jumping. Traditional methods such as electromyography and physiological cross-sectional area assessments face inherent challenges in obtaining precise, real-time data from the human body, as detailed in previous chapters. To address these limitations, STIMES offer a promising solution [238].

The rapid advancement of STIMES has brought significant attention to fabric-based sensors, which include technologies such as capacitance [98, 283-285], piezoresistivity [286, 287], piezoelectricity [288-290], and triboelectricity [291-294]. These sensors provide innovative approaches to capturing muscle activity data. Concurrently, the rise of Natural User Interfaces (NUI) emphasizes the creation of intuitive connections between the physical and digital realms, which is crucial for effective big data analysis and machine learning applications [295, 296].

Previous research has investigated the application of fabric resistive strain sensors for monitoring upper arm muscle force [133, 297, 298]. These studies utilized the sensors to detect circumferential strain in the limbs and subsequently predicted muscle force using a circumference-to-torque model across various modes, including isometric, isokinetic, and isotonic. This approach highlights the potential of fabric-based sensors in enhancing the accuracy and usability of muscle monitoring systems. The systems exhibited the benefits of

continuous detection, user comfort, portability, lightweight, and convenience, especially for the sports field. Nonetheless, the previous work never explored the lower extremities muscles, which should be emphasized, due to their complexity and functional significance in weight-bearing and locomotion. Moreover, various fabric-based sensors have unique advantages and various characteristics. Hence, the obtained circumference-to-torque model cannot be generalized for other sensors and needs further study.

Considering the systematic design of an elaborate end-to-end user-centered STIMES lacks enough in-depth research, especially for healthcare applications that highly demand easy use, low cost, long-term adoption, efficient communication between patients and doctors, and effective follow-up, the section addresses these issues to further explore monitoring gastrocnemius muscle force by integrated smart compression stockings, which can deliver healthcare service to anyone at anytime at anywhere.

5.2.2. Architecture pipeline design

Compression stockings are designed to provide graduated compression, with the highest pressure at the ankles that gradually decreases up the leg. This design is intended to maximize therapeutic effectiveness and physiological benefits for users. The compression exerted by these stockings aids in constricting veins and leg tissues, thereby facilitating the efficient return of blood to the heart. This mechanism is advantageous for enhancing blood circulation, preventing blood clots, reducing leg swelling, alleviating discomfort, and providing support during

pregnancy. Despite these benefits, accurately monitoring the pressure distribution in commercially available compression stockings remains challenging.

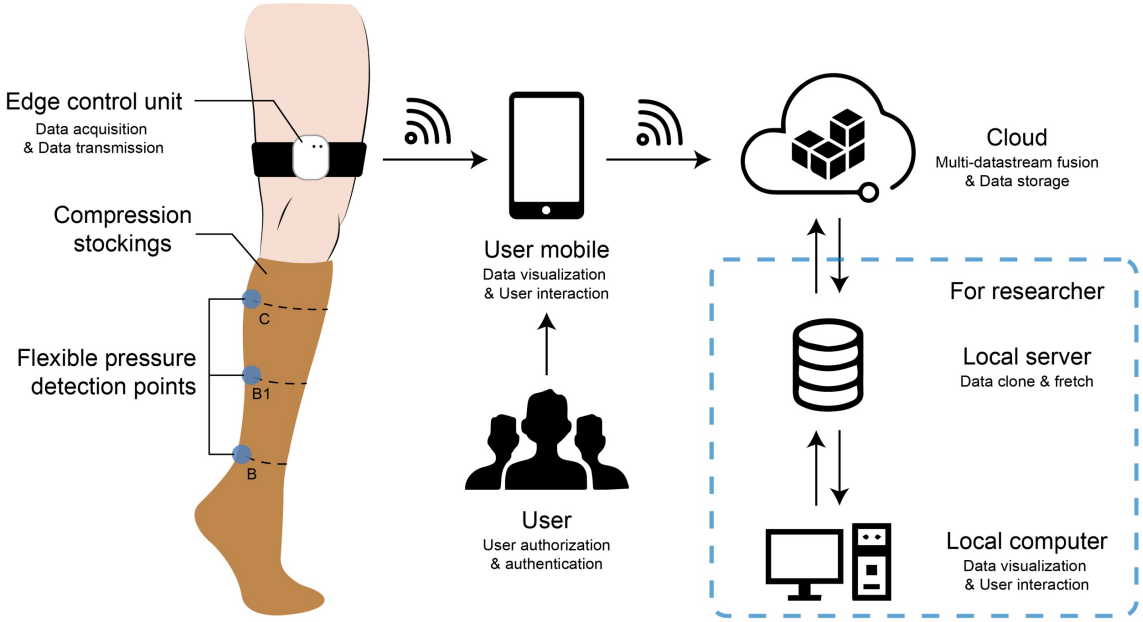

Figure 5-1 Architecture pipeline design for the integrated smart compression stockings system.

This study focuses on the development of smart compression stockings, which integrate compression garments with embedded fabric pressure sensors, an edge control unit, a mobile application, and a cloud-based backend. This innovative system offers several key advantages, including responsiveness to both static and dynamic pressure changes, high sensitivity to pressure variations, and reliable accuracy. By incorporating these advanced features, the smart compression stockings aim to provide a more precise and effective solution for monitoring and optimizing compression therapy. Furthermore, they are designed to be flexible, user-friendly,

and easily integrated with external systems. They also support rapid internal upgrades and repairs, making it adaptable to a wide range of application scenarios. The architectural design of this system is comprehensively illustrated in Figure 5-1.

The development of textile capacitive pressure sensors in the laboratory utilizes a sandwich structure, which offers several advantages. These sensors are easy to fabricate and provide satisfactory accuracy and repeatability. They exhibit high sensitivity within the low-pressure range, specifically below 50 mmHg, making them ideal for applications requiring precise pressure monitoring. Furthermore, these sensors are characterized by low power consumption and rapid response times, enhancing their suitability for dynamic environments. The sensors are strategically positioned at designated points—B, B1, and C—on the compression stockings, in accordance with the RAL-GZ 387/1 standard [228], to ensure optimal performance and compliance with industry benchmarks.

The edge control unit is designed to be both cost-effective and energy-efficient, facilitating the detection, processing, and wireless transmission of electrical signals generated by the sensors. This unit plays a crucial role in the overall system by enabling real-time data acquisition and communication. Complementing the hardware, an Android mobile application has been developed to provide intuitive data visualization and enhance the user interface. This application ensures seamless interaction with the cloud backend, allowing users to access and analyze data effortlessly.

The cloud backend is robustly engineered to support multi-user data storage, authentication, and authorization, ensuring secure and efficient data management. It features a comprehensive data center dashboard that provides users with insights into system performance and data trends. Additionally, the backend incorporates continuous integration and delivery processes, which streamline updates and improvements, maintaining the system's reliability and efficiency. This integrated approach ensures that the smart compression stocking system is both technologically advanced and user-friendly, offering a complete solution for monitoring and optimizing compression therapy.

5.2.3. Fabric sensors, edge control unit, user interface preparation

As shown in the previous chapters, fundamental preparation works involved the design and implementation of fabric pressure capacitive sensors, a dedicated edge control unit, user interface based on the developed Android application.

The capacitive pressure sensor was carefully engineered using a simple sandwich structure, which consists of two layers of conductive fabric serving as electrodes, with a dielectric layer in between. This dielectric layer is made from polydimethylsiloxane (PDMS) infused with carbon black (CB) powder, a combination chosen to enhance the sensor's electrical properties. The surface of the dielectric layer was treated with abrasive paper to further improve its sensitivity and performance. To ensure the sensors are durable and resistant to external friction and mechanical strain, they were encapsulated with protective layers of thermoplastic

polyurethane (TPU). This encapsulation not only protects the sensors but also maintains their flexibility, allowing them to conform to the contours of the body.

These flexible capacitive pressure sensors are designed to be attached to various locations on compression stockings, providing precise pressure monitoring. In this study, the sensors were strategically positioned at specific points, labeled B, B1, and C, on the stockings, ensuring that the sensors deliver optimal performance and accurate pressure readings. By adhering to these standards, the study aims to achieve reliable data collection and enhance the therapeutic effectiveness of the compression stockings.

For the purpose of this study, class I compression garments, adhering to the RAL-GZ 387/1 standard [228], were utilized with healthy participants rather than for therapeutic treatment. These garments exert less than 18 mmHg of compression, minimizing environmental impact on muscles and enhancing long-term wearability. Upon integrating the flexible capacitive pressure sensors, the design of an edge control unit was prioritized to dynamically and simultaneously measure the fabricated sensors' capacitance values and facilitate wireless transmission of real-time data. Key design considerations included ensuring safety, minimizing power consumption, reducing costs, promoting long-term sustainable use, and maintaining portability.

To achieve these objectives, all components were selected from widely available commercial electronic parts. The system's main controller chip was the STM32, while the capacitance

measurement and analog-to-digital converter (ADC) processor was the PCap01. Bluetooth functionality was provided by the nRF51802 processor, charging control was managed by the TP4059 chip, and a 2400mAh lithium battery pack was employed. The relevant material cost for the edge control unit was estimated at 234 RMB, equivalent to approximately 33 USD.

Smart mobile phones are widely used in everyone's daily life and possess the advantage of efficient computation, storage, popular operation systems, functional applications, multimedia functionalities, wireless communication, and traditional phone functions. Hence, commercial smart mobile phones were properly chosen to serve as user interactive devices, which means all human interactions take place on smart phones, including information processing and display, emergency notification and alarm, and other physical exercise recommendation. The received dataflow from the edge control unit was structured and stored in the mobile phones' SQLite database. Heavy computation loads, such as processing capacitance raw values, and data storage were assigned to smart phones, so that the edge control unit consumed less resources and power. The whole system architecture is more flexible and easier to adapt, which meets the golden rules of DevOps practices and agile development. Users could conveniently read pressure values in real-time and receive healthcare notifications after the historic pressure values were analyzed on smart phones.

As Android mobile phones have a higher penetration in the consumer market, therefore, the Android application, named Smart Compression Stocking Utility version 1, was developed through the integrated development environment for Google's Android operating system and

was compatible with Android 8.0 or later architecture. User experience flew from login, scanning and finding Bluetooth devices, pairing to desired devices, and data visualization. Users registered or logged in through used username and password to access the next page. Then clicking the scan button would trigger nearby Bluetooth device detection. After users chose the one matching their smart compression stocking, the status would change to "connected". The application system architecture was built on Android 8.0, leveraging the Bluetooth Low Energy (BLE) protocol stack to facilitate reliable connections between mobile devices and the BLE-enabled sensors embedded in the stockings. To establish stable and efficient communication, the socket method was employed, which ensures a persistent connection for data transmission. The Android native binder was utilized to manage data communication between the Bluetooth data received from the sensors and the upper-layer applications. This approach allows for seamless integration and efficient handling of data, ensuring that the information captured by the sensors is accurately relayed to the mobile application for processing and analysis. The system was designed to present three channels of capacitance data, which were visualized through graphs, textual summaries, and detailed analysis reports. This multi-faceted presentation of data enables users to gain comprehensive insights into the pressure distribution and muscle force dynamics monitored by the smart compression stockings. By integrating these advanced communication and visualization techniques, the system enhances the user experience and provides valuable feedback for both clinical and personal health monitoring applications.

5.2.4. Cloud backend design, deployment, and integration

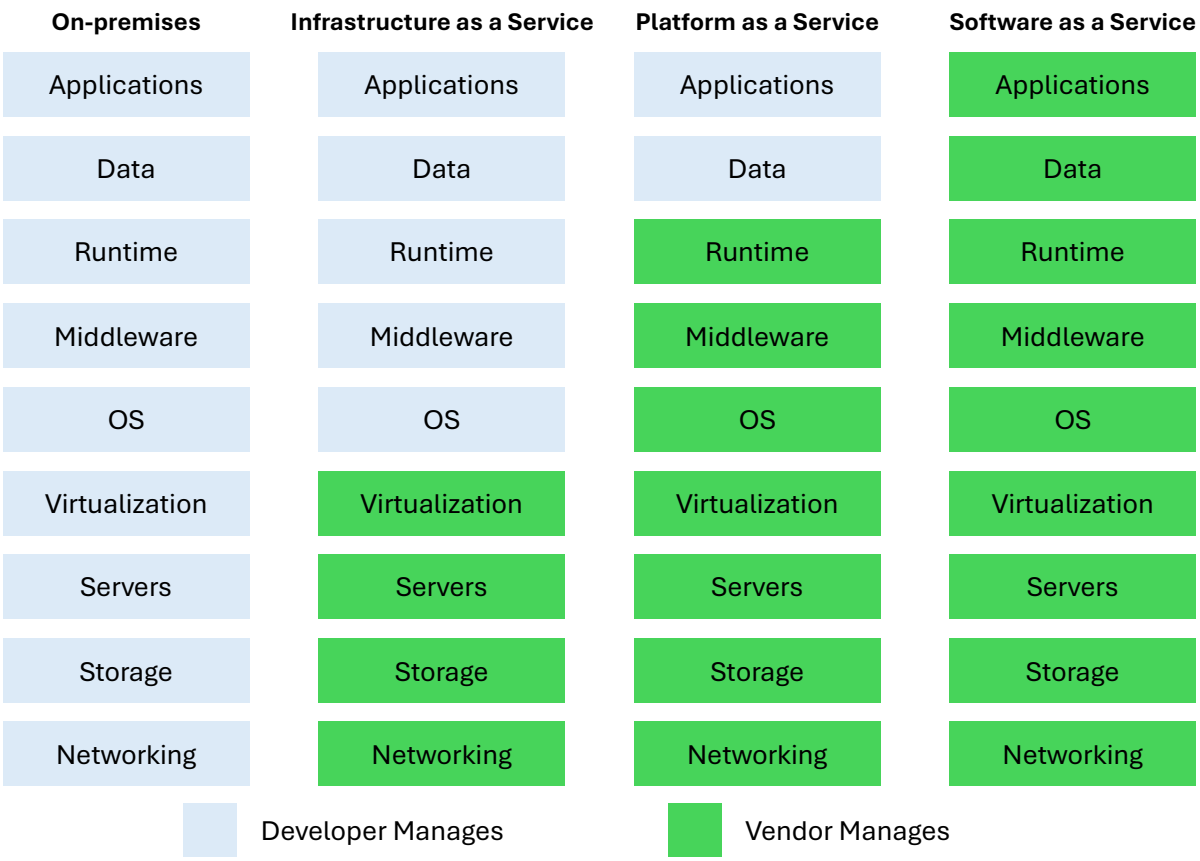

Figure 5-2 Comparison of different Cloud computing services.

Furthermore, to enhance accessibility and usability for users in diverse settings, the cloud backend was meticulously designed and deployed. This system capitalizes on the inherent advantages of cloud computing, including the ability to dynamically scale computing capacity resources and storage resources in response to fluctuating demand. It automatically and resiliently adjusts needed resource allocation, ensuring optimal performance and efficiency. The cloud backend is characterized by rapid response times, secure data communication, and cost-effective operations. Additionally, it facilitates straightforward testing and global deployment, making it an ideal solution for widespread use. A comparative analysis of various

cloud computing services is illustrated in Figure 5-2, highlighting the distinct features and benefits of each option.

In the realm of cloud computing, various service models offer distinct advantages and considerations for organizations. This comparison will delve into the on-premise model, along with the Infrastructure as a Service (IaaS), Platform as a Service (PaaS), and Software as a Service (SaaS) models [299, 300]. The choice between on-premise, IaaS, PaaS, and SaaS models depends on the developers' specific requirements, resources, and priorities. On-premise allows maximum control but requires substantial investments. IaaS offers flexibility and cost savings but retains some infrastructure management responsibilities. PaaS streamlines application development but limits customization. SaaS provides ready-to-use applications but reduces control over the underlying infrastructure. Developers must carefully evaluate their needs and consider factors such as security, scalability, costs, and time-to-market when selecting the most suitable cloud service model.

On-premise deployment involves hosting and managing all IT infrastructure within the organization's premises. This model grants complete control over hardware, software, and data, allowing for customization and adherence to specific security and compliance requirements. However, it necessitates significant upfront investments in hardware and ongoing maintenance costs. Additionally, scaling resources can be time-consuming and may require additional investments.

IaaS provides virtualized computing resources, including servers, storage, and networking components, delivered over the connected network. This model offers flexibility, scalability, and cost savings, as developers can procure and manage resources on-demand, paying only for actual use. With IaaS, developers can focus on their applications and data without the burden of infrastructure management. However, developers remain responsible for operating system management, application deployment, and data security.

PaaS goes a step further by providing a platform for developing, testing, deploying, and managing applications without the need for infrastructure management. PaaS offers a preconfigured environment, including development tools, runtime frameworks, and application services. This enables faster application development, upgrade, and deployment, as developers can concentrate substantially on coding and innovation. However, PaaS limits customization options and may require adherence to specific platform constraints.

SaaS represents the highest level of abstraction, delivering fully functional applications over the connected network. With SaaS, developers can access software applications and services on demand, eliminating the need for installation, maintenance, and management. This model offers scalability, automatic updates, and multi-device accessibility. However, customization options may be limited, as developers must rely on the features and configurations provided by the SaaS provider. Generally, SaaS providers manage networking, storage, servers, virtualization, operation systems, middleware, runtime, data, and applications. For the fast prototype and quick evaluation, the SaaS model was adopted in this research.

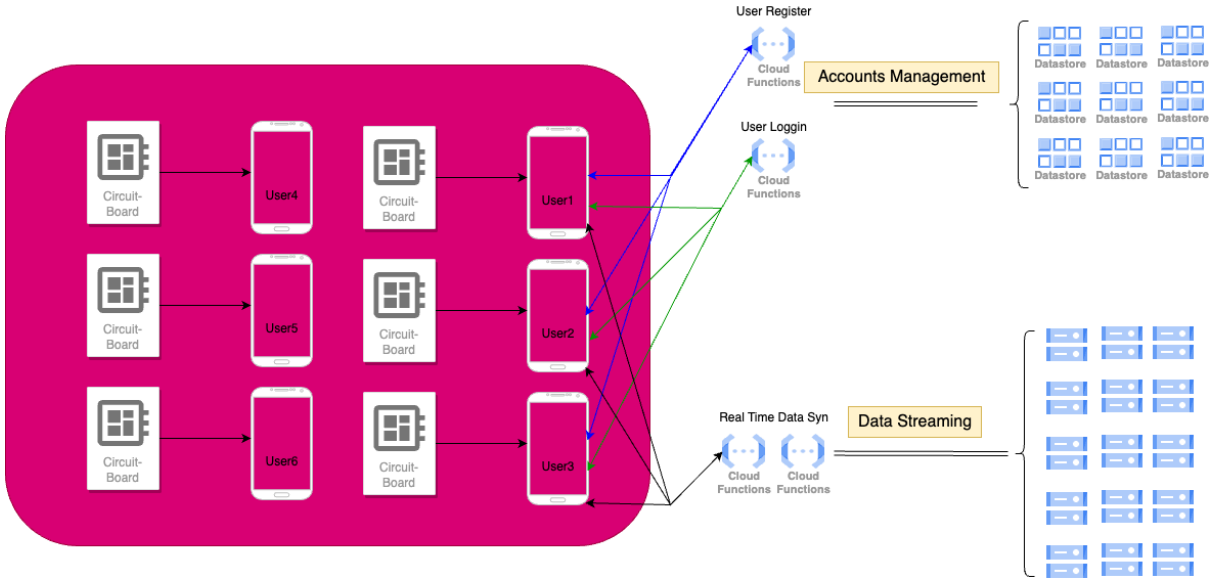

Figure 5-3 Cloud backend architecture and integration.

The Google Cloud Platform was chosen to establish and validate the data pipeline's feasibility and effectiveness. This decision was driven by the platform's robust capabilities in handling large-scale data operations and its support for advanced cloud computing technologies. The Android application, Smart Compression Stocking Utility, was upgraded to version 2 to facilitate secure communication with the cloud endpoint using Hypertext Transfer Protocol Secure (HTTPS). This upgrade ensures that data transmitted between the mobile application and the cloud is protected against unauthorized access and breaches.

The adoption of a microservice architecture was pivotal in achieving functional decoupling and enabling flexible service scaling. This architectural approach allowed for the independent development and deployment of various services, including data streaming and user account management functionalities, using Node.js and JavaScript. These services were implemented

as serverless functions within the Google Cloud Platform, optimizing resource utilization and scalability, as depicted in Figure 5-3..

This cloud-based system architecture supports the storage of comprehensive user information, encompassing account details such as name, password, email, phone number, age, gender, weight, and height, alongside real-time measurement data. These data are organized and managed within cloud-based SQL databases, ensuring efficient data retrieval and management, as illustrated in Figure 5-4 and Figure 5-5. Additionally, the relevant codebase was stored, built, and integrated within the cloud environment to facilitate continuous integration and continuous delivery (CI/CD) processes. This setup ensures that updates to the system are executed seamlessly and efficiently, enhancing the overall functionality and reliability of the smart compression stocking system. By leveraging the capabilities of the Google Cloud Platform, the study demonstrates a scalable and secure approach to managing and analyzing health-related data in real-time.

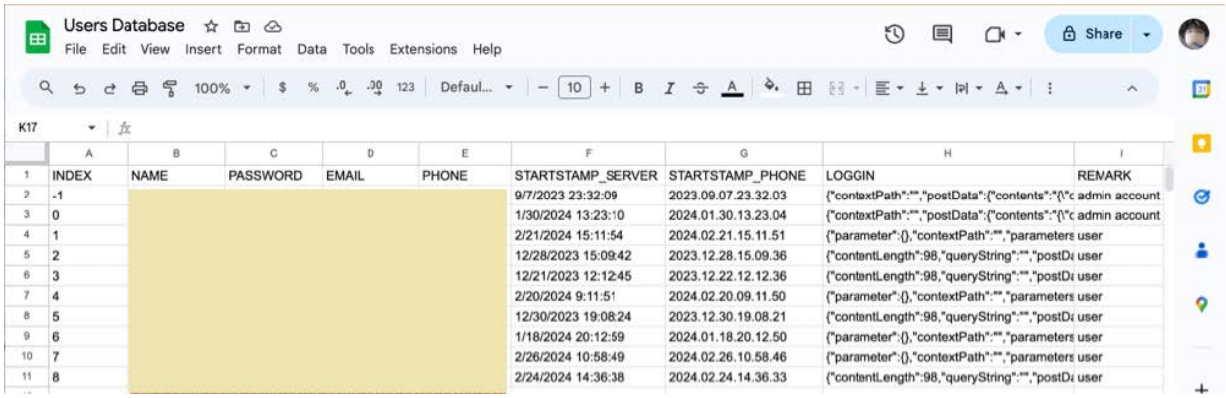

	A	B	C	D	E	F	G	H	I
1	INDEX	NAME	PASSWORD	EMAIL	PHONE	STARTSTAMP_SERVER	STARTSTAMP_PHONE	LOGGIN	REMARK
2	-1					9/7/2023 23:32:09	2023.09.07.23.32.03	{"contextPath":"","postData":{"contents":"{\"c	admin account
3	0					1/30/2024 13:23:10	2024.01.30.13.23.04	{"contextPath":"","postData":{"contents":"{\"c	admin account
4	1					2/21/2024 15:11:54	2024.02.21.15.11.51	{"parameter":{},"contextPath":"","parameters	user
5	2					12/28/2023 15:09:42	2023.12.28.15.09.36	{"contentLength":98,"queryString":"","postDa	user
6	3					12/21/2023 12:12:45	2023.12.22.12.12.36	{"contentLength":98,"queryString":"","postDa	user
7	4					2/20/2024 9:11:51	2024.02.20.09.11.50	{"parameter":{},"contextPath":"","parameters	user
8	5					12/30/2023 19:08:24	2023.12.30.19.08.21	{"contentLength":98,"queryString":"","postDa	user
9	6					1/18/2024 20:12:59	2024.01.18.20.12.50	{"parameter":{},"contextPath":"","parameters	user
10	7					2/26/2024 10:58:49	2024.02.26.10.58.46	{"parameter":{},"contextPath":"","parameters	user
11	8					2/24/2024 14:36:38	2024.02.24.14.36.33	{"contentLength":98,"queryString":"","postDa	user

Figure 5-4 Illustration of user information database demo.

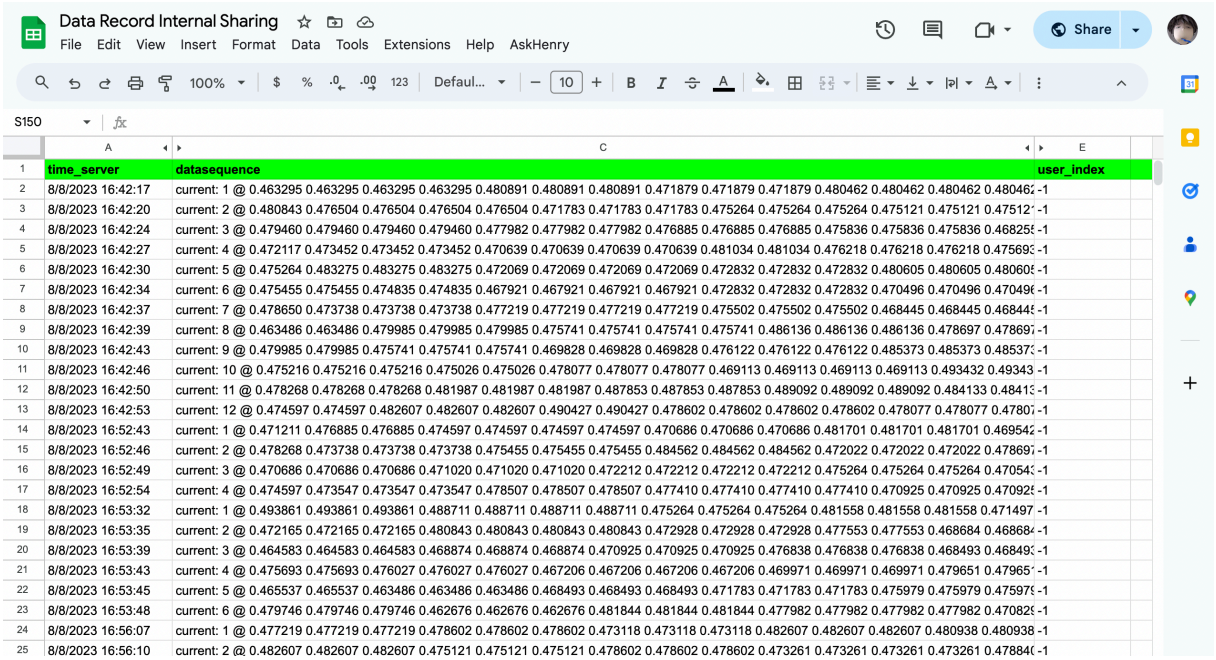

	A	C	E
1	time_server	datasequence	user_index
2	8/8/2023 16:42:17	current: 1 @ 0.463295 0.463295 0.463295 0.463295 0.480891 0.480891 0.480891 0.471879 0.471879 0.471879 0.480462 0.480462 0.480462 0.480462	-1
3	8/8/2023 16:42:20	current: 2 @ 0.480843 0.476504 0.476504 0.476504 0.476504 0.471783 0.471783 0.471783 0.475264 0.475264 0.475264 0.475121 0.475121 0.475121	-1
4	8/8/2023 16:42:24	current: 3 @ 0.479460 0.479460 0.479460 0.479460 0.477982 0.477982 0.477982 0.476885 0.476885 0.476885 0.475836 0.475836 0.475836 0.468255	-1
5	8/8/2023 16:42:27	current: 4 @ 0.472117 0.473452 0.473452 0.473452 0.470639 0.470639 0.470639 0.470639 0.481034 0.481034 0.476218 0.476218 0.476218 0.475693	-1
6	8/8/2023 16:42:30	current: 5 @ 0.475264 0.483275 0.483275 0.483275 0.472069 0.472069 0.472069 0.472069 0.472832 0.472832 0.472832 0.480605 0.480605 0.480605	-1
7	8/8/2023 16:42:34	current: 6 @ 0.475455 0.475455 0.474835 0.474835 0.467921 0.467921 0.467921 0.467921 0.472832 0.472832 0.472832 0.470496 0.470496 0.470496	-1
8	8/8/2023 16:42:37	current: 7 @ 0.478650 0.473738 0.473738 0.473738 0.477219 0.477219 0.477219 0.477219 0.475502 0.475502 0.475502 0.468445 0.468445 0.468445	-1
9	8/8/2023 16:42:39	current: 8 @ 0.463486 0.463486 0.479985 0.479985 0.479985 0.475741 0.475741 0.475741 0.475741 0.486136 0.486136 0.486136 0.478697 0.478697	-1
10	8/8/2023 16:42:43	current: 9 @ 0.479985 0.479985 0.475741 0.475741 0.475741 0.469828 0.469828 0.469828 0.476122 0.476122 0.476122 0.485373 0.485373 0.485373	-1
11	8/8/2023 16:42:46	current: 10 @ 0.475216 0.475216 0.475216 0.475026 0.475026 0.478077 0.478077 0.478077 0.469113 0.469113 0.469113 0.469113 0.493432 0.49343	-1
12	8/8/2023 16:42:50	current: 11 @ 0.478268 0.478268 0.478268 0.481987 0.481987 0.481987 0.487853 0.487853 0.487853 0.489092 0.489092 0.489092 0.484133 0.48413	-1
13	8/8/2023 16:42:53	current: 12 @ 0.474597 0.474597 0.482607 0.482607 0.482607 0.490427 0.490427 0.478602 0.478602 0.478602 0.478602 0.478077 0.478077 0.47801	-1
14	8/8/2023 16:52:43	current: 1 @ 0.471211 0.476885 0.476885 0.474597 0.474597 0.474597 0.474597 0.470686 0.470686 0.470686 0.481701 0.481701 0.481701 0.469542	-1
15	8/8/2023 16:52:46	current: 2 @ 0.478268 0.473738 0.473738 0.473738 0.475455 0.475455 0.475455 0.484562 0.484562 0.484562 0.472022 0.472022 0.472022 0.478691	-1
16	8/8/2023 16:52:49	current: 3 @ 0.470686 0.470686 0.470686 0.471020 0.471020 0.471020 0.472212 0.472212 0.472212 0.472212 0.475264 0.475264 0.475264 0.470543	-1
17	8/8/2023 16:52:54	current: 4 @ 0.474597 0.473547 0.473547 0.473547 0.478507 0.478507 0.478507 0.477410 0.477410 0.477410 0.477410 0.470925 0.470925 0.470925	-1
18	8/8/2023 16:53:32	current: 1 @ 0.493861 0.493861 0.493861 0.488711 0.488711 0.488711 0.488711 0.475264 0.475264 0.475264 0.481558 0.481558 0.481558 0.471497	-1
19	8/8/2023 16:53:35	current: 2 @ 0.472165 0.472165 0.472165 0.480843 0.480843 0.480843 0.480843 0.472928 0.472928 0.472928 0.477553 0.477553 0.468684 0.468684	-1
20	8/8/2023 16:53:39	current: 3 @ 0.464583 0.464583 0.464583 0.468874 0.468874 0.468874 0.470925 0.470925 0.470925 0.476838 0.476838 0.476838 0.468493 0.468493	-1
21	8/8/2023 16:53:43	current: 4 @ 0.475693 0.475693 0.476027 0.476027 0.476027 0.467206 0.467206 0.467206 0.467206 0.469971 0.469971 0.469971 0.479651 0.479651	-1
22	8/8/2023 16:53:45	current: 5 @ 0.465537 0.465537 0.463486 0.463486 0.463486 0.468493 0.468493 0.468493 0.471783 0.471783 0.471783 0.475979 0.475979 0.475979	-1
23	8/8/2023 16:53:48	current: 6 @ 0.479746 0.479746 0.479746 0.462676 0.462676 0.462676 0.481844 0.481844 0.481844 0.477982 0.477982 0.477982 0.477982 0.470828	-1
24	8/8/2023 16:56:07	current: 1 @ 0.477219 0.477219 0.477219 0.478602 0.478602 0.478602 0.473118 0.473118 0.473118 0.482607 0.482607 0.482607 0.480938 0.480938	-1
25	8/8/2023 16:56:10	current: 2 @ 0.482607 0.482607 0.482607 0.475121 0.475121 0.475121 0.478602 0.478602 0.478602 0.473261 0.473261 0.473261 0.473261 0.47884	-1

Figure 5-5 Illustration of user real-time measurement database demo.

5.3. Clinical Experiments Setup and Data Analysis

5.3.1. Participants and experimental protocol

It is through the rigid scrutiny, approval, and other relevant procedures to apply the integrated smart compression stocking system to clinical experiments. In compliance with ethical standards and guidelines, the research conducted in this study involving human subjects or animals adhered to rigorous protocols and procedures. Prior to commencing the research, all ethical and experimental aspects of the study were subjected to thorough review and approval by the Institutional Review Board of the Hong Kong Polytechnic University, under Application No. HSEARS20230717004. This ensured that the study was conducted with the utmost consideration for the welfare, rights, and safety of the participants or subjects involved.

The clinical study was conducted with a cohort of twelve physically fit adult participants, equally divided between six males and six females. Participants' ages ranged from 33 to 21 years, with anthropometric measurements including heights varying from 1.9 m to 1.5 m and weights spanning from 77 kg to 43 kg, as shown in Table 5-1. The exclusion criteria were comprehensive, including self-confirmed inability to perform smooth positional transfers or maintain a seated stable position for over half hour, a body mass index (BMI) exceeding 35 kg/m^2. Neurological exclusion criteria encompassed participants with moderate to severe traumatic brain injury or spinal cord injury, as these conditions could significantly impact motor control and muscle activation patterns relevant to the study measurements. Similarly, individuals with documented cauda equina syndrome or radiculopathy were excluded due to potential lower extremity sensorimotor deficits that could influence muscle function and movement patterns. Musculoskeletal exclusion criteria included any history of surgical interventions on the tested lower extremity, as post-surgical anatomical modifications or scar tissue formation could alter normal biomechanical function and sensor placement accuracy. Participants with documented myopathies were excluded due to inherent muscle tissue abnormalities that could confound muscle activity measurements. Finally, individuals presenting with movement-induced ankle clonus or lower extremity muscle spasms were excluded, as these involuntary muscle contractions could introduce measurement artifacts and compromise data quality during the experimental procedures. All participants provided informed consent, approved by the Hong Kong Polytechnic University Institutional Review Board, and were briefed on data privacy and potential risks associated with the experiment.

Table 5-1 Demographic and anthropometric data of the study participants.

Participant	Age (years)	Gender	Height (cm)	Weight (kg)	BMI	Dominant Leg
Subject_1	25	M	173	65	21.7	R
Subject_2	21	M	175	65	21.2	R
Subject_3	21	M	170	60	20.8	R
Subject_4	21	F	162	45	17.1	R
Subject_5	22	F	166	77	27.9	R
Subject_6	21	F	165	75	27.5	R
Subject_7	22	F	151	44	19.3	R
Subject_8	21	F	150	43	19.1	R
Subject_9	22	F	155	47	19.6	R
Subject_10	31	M	190	75	20.8	R
Subject_11	33	M	175	65	21.2	R
Subject_12	26	M	174	66	21.8	R

The experimental protocol involved positioning participants in a standardized configuration to ensure measurement reliability and biomechanical accuracy. Each participant was fitted with a smart compression stocking on the right lower extremity, with the integrated flexible sensor strategically placed at point C on the gastrocnemius muscle belly, corresponding to the location of maximal cross-sectional area. This positioning optimized sensor contact with the target muscle tissue and minimized movement artifacts during data collection.

Participants were subsequently positioned on a calibrated Humac NORM isokinetic dynamometer system, which provided simultaneous real-time measurement and recording of ankle plantarflexion angular position and corresponding joint torque generation, as illustrated in Figure 5-6. The seating configuration consisted of an upright posture maintained on a foam cushion support, with hip flexion angles standardized between 1.745 rad and 2.094 rad to ensure participant comfort while maintaining postural stability throughout the testing protocol. The ipsilateral knee joint was positioned in full extension, while the right ankle was maintained in anatomical neutral alignment to establish a consistent baseline position.

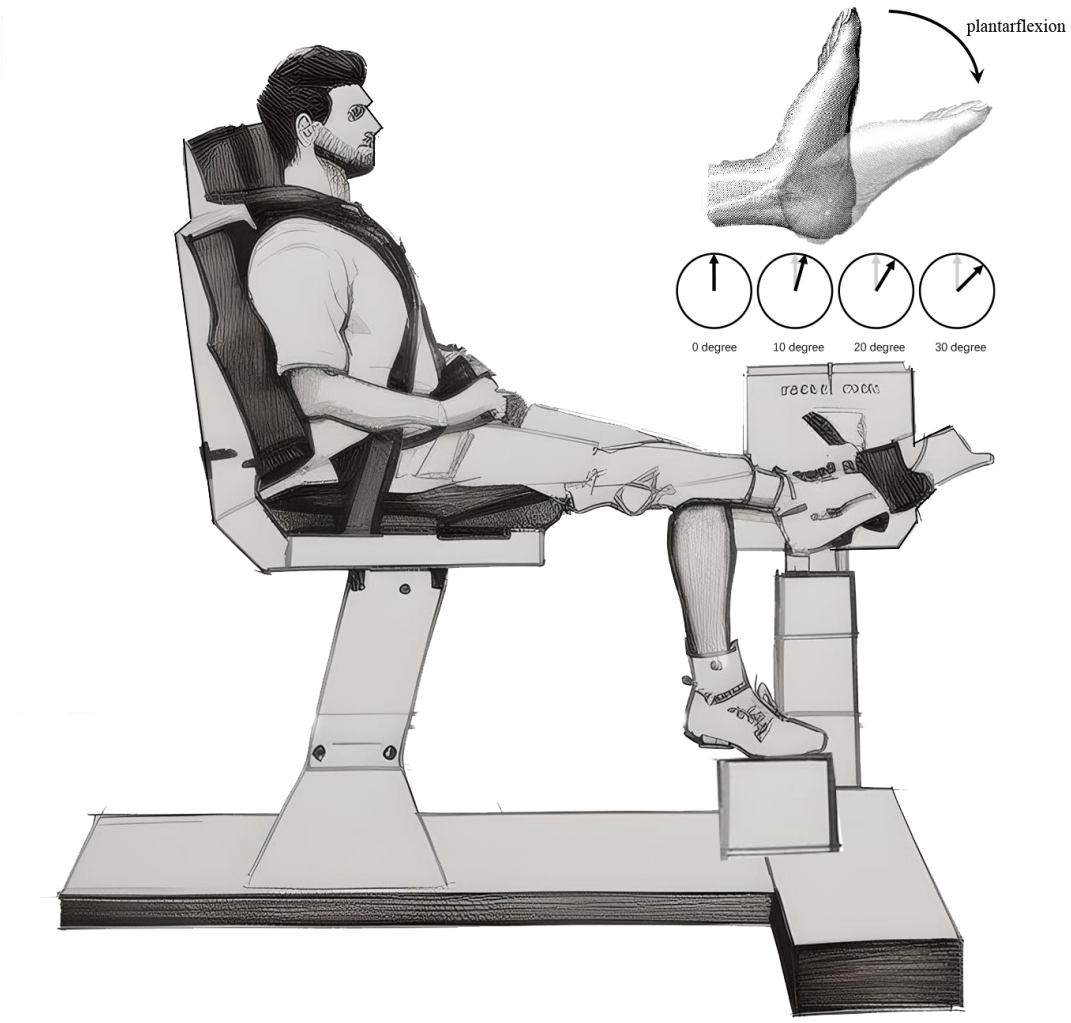

Figure 5-6 Experimental setup and exercise protocol.

Safety and stability were ensured through the application of a waist restraint belt, while the right foot was secured flat against the dynamometer footplate using a padded Velcro fastening system. Critical to the experimental setup was the precise biomechanical alignment whereby the foot position was congruent with the dynamometer's fulcrum point, ensuring optimal alignment between the anatomical ankle joint axis and the mechanical lever arm axis of the device. This configuration provided a standardized measurement foundation while permitting unrestricted

ankle joint movement through the complete range of motion in both plantarflexion and dorsiflexion directions, as depicted in Figure 5-7.

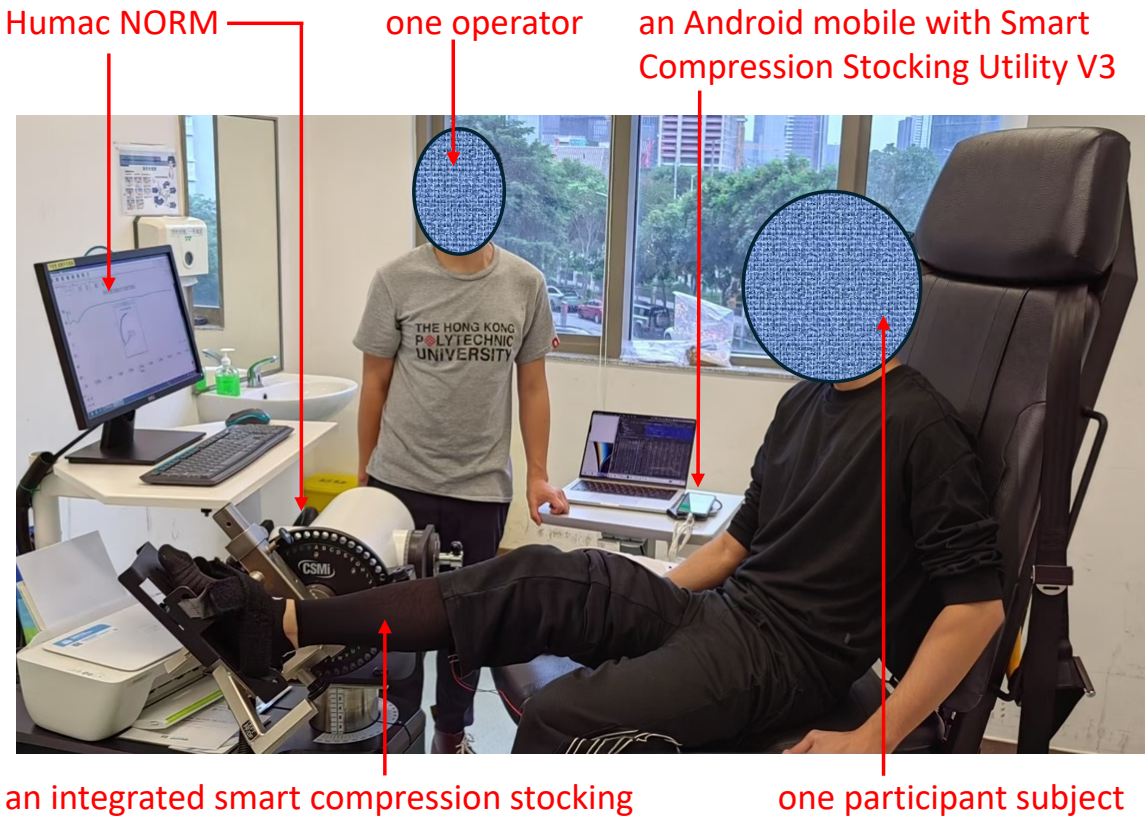

Figure 5-7 Clinical experimental setup on site illustration.

Prior to data collection, the Humac NORM dynamometer underwent systematic calibration procedures and was configured to operate in isometric mode. Torque-time data were continuously recorded throughout each experimental session for subsequent analysis, with data acquisition parameters maintained consistently across all participants to ensure measurement standardization and reliability.

The Smart Compression Stocking Utility Android application was developed and upgraded to version 3, incorporating a new event trigger function. This enhancement allowed the experiment operator to initiate the recording of capacitance value data streams by pressing the "Start Exercise" button, while simultaneously starting the recording of torque data streams on the Humac NORM desktop software. The edge control unit adjusted the sampling rate to 10 Hz, whereas the Humac NORM operated at 10 times of that. The two sets of time-series data were subsequently aligned, compared, and analyzed through correlation analysis to ensure accuracy and reliability in the measurements.

5.3.2. Clinical experimental protocol

The biomechanical principles underlying isometric muscle contraction provide the theoretical foundation for this investigation. During isometric contractions, the generated torque serves as a direct indicator of skeletal muscle force production, particularly when joint position remains constant and the moment arm length is maintained unchanged. This relationship establishes torque as a quantifiable and reliable measure of the force exerted by the target musculature. Previous research has demonstrated that maximum isometric force generation can be calculated through the mathematical relationship between physiological cross-sectional area (PCSA) and maximum isometric stress, with force being the product of these two parameters [223-225]. Additionally, established literature has documented linear relationships between torque generation and limb circumference measurements, providing further validation for morphometric approaches to force estimation [298].

Building upon this theoretical framework, the present study hypothesized that a linear relationship exists between torque generation and pressure variations measured within compression stockings, with these pressure changes resulting from alterations in PCSA during muscle contraction. This hypothesis was systematically evaluated through rigorous statistical analysis to determine the validity and strength of this proposed relationship.

The experimental protocol consisted of a standardized testing sequence wherein each participant completed four distinct exercise conditions with once repetitions. The Humac NORM dynamometer lever arm was systematically positioned at four predetermined angular positions of 0°, 10°, 20°, and 30° of plantarflexion for successive exercises. The reference position of 0° corresponded to the anatomical neutral position, with plantarflexion direction designated as positive angular displacement according to standard biomechanical conventions.

Within each angular position condition, participants were instructed to perform maximum voluntary isometric contractions (MVIC) against the fixed lever arm, maintaining peak effort for a duration of 5 seconds. Following each contraction, a standardized 10-second rest interval was implemented before participants performed a second 5-second MVIC at the next angular position. To minimize the effects of muscle fatigue and reduce participant discomfort, extended rest intervals of 20 seconds were prescribed between successive two exercise sets, allowing for adequate physiological recovery, as depicted in Figure 5-8.

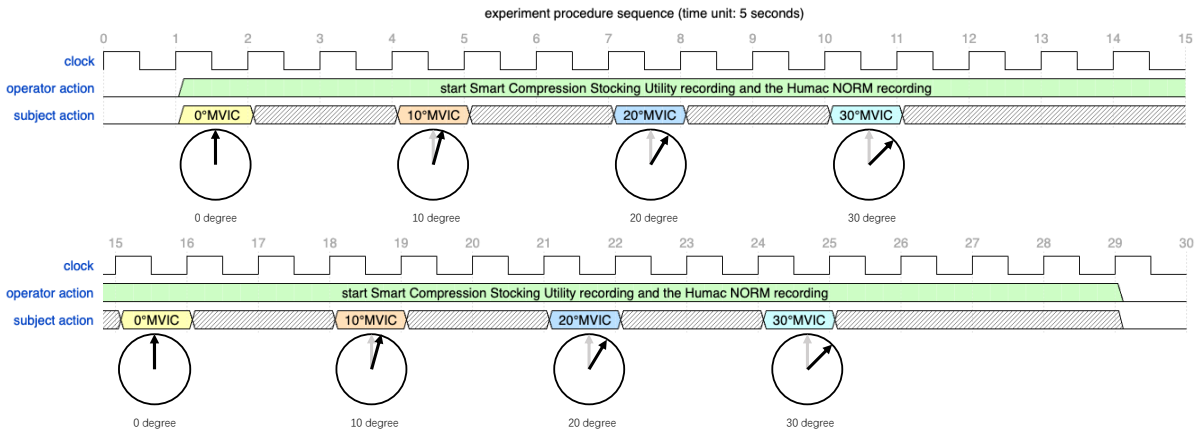

Figure 5-8 The chronological sequence of the standardized clinical experimental protocol.

Throughout the experimental procedures, an experiment operator maintained constant supervision to ensure precise temporal synchronization of data acquisition between the Humac NORM dynamometer system and the smart compression stocking system. This synchronization protocol was critical for maintaining data integrity and enabling accurate correlation analysis between torque measurements and pressure recordings during each contraction phase.

5.3.3. Data collection and preprocessing

This study aims to elucidate the relationship between pressure changes, as indicated by the integrated smart compression stocking system's readout (C), and muscle force, represented by the generated muscle torque values (NT). It is hypothesized that a simple linear relationship exists between these variables, characterized by fitting coefficients, which are defined in Equation (5.1) and determined using the least squares (LS) method. To assess the strength of

this linear relationship, correlation coefficients between *C* and *NT* were calculated, as defined in Equation (5.2).

$$NT = A \times C + B \tag{5.1}$$

$$RR = \frac{conv(C, NT)}{\sigma(C) \times \sigma(NT)} \tag{5.2}$$

The duration of MVIC can be segmented into three different phases, comprising the initial loading phase where force is generated, the holding phase at peak contraction, and the relaxation phase as force dissipates, as depicted in Figure 5-9(b). The loading phase is particularly noteworthy for its linear relationship between muscle volume change and muscle force, as supported by previous research [298]. In contrast, the holding and relaxation phases involve more complex muscle dynamics [301]. Consequently, this study concentrated on the loading phase, which was predefined as the initial 1-second duration within each MVIC across the eight exercises performed by each participant, as illustrated in Figure 5-9(a).

To address inter-individual variability in muscle performance characteristics and minimize potential experimental discrepancies, a normalization procedure was applied to the raw time-series data for both muscle torque and capacitance measurements. This step was crucial due to inherent differences in baseline muscle strength, anatomical dimensions, and physiological

responses among participants, which could introduce systematic bias into the analysis if not properly accounted for.

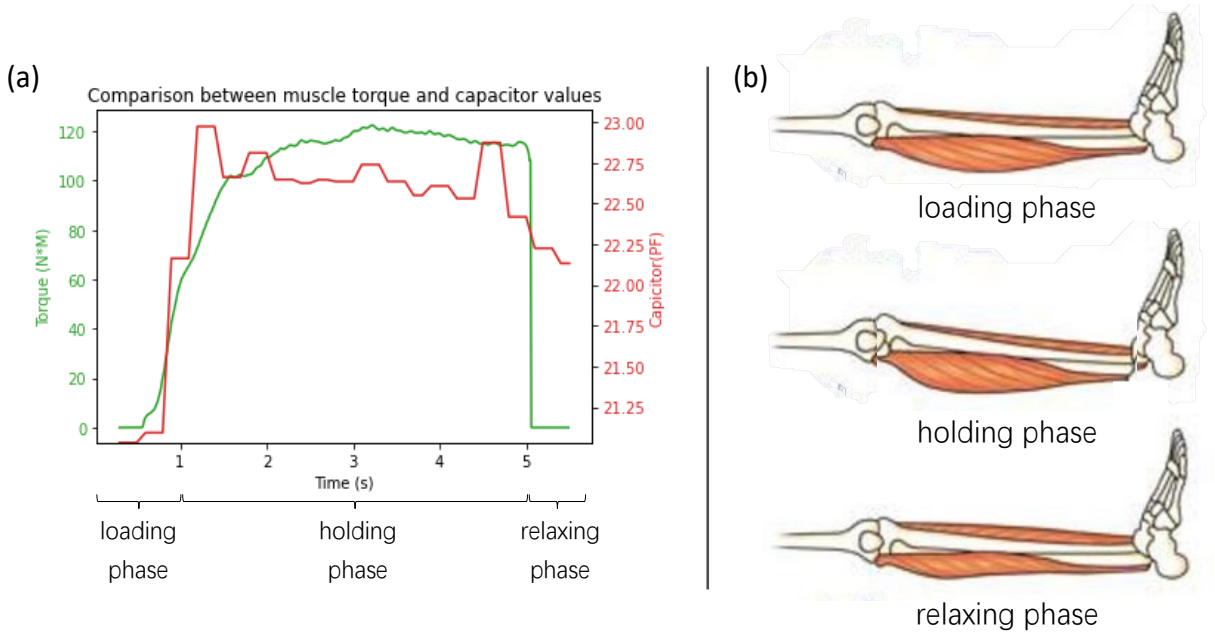

Figure 5-9 Illustrates the three distinct phases of maximum voluntary isometric contractions.

The normalization methodology was implemented on a participant-specific basis, using each individual's complete dataset from all assigned isometric exercise conditions as the reference standard, as defined in Equations (5.3) and (5.4). This within-subject normalization approach ensured that relative changes in torque generation and capacitance variation could be compared across different angular positions and contraction intensities, while controlling for individual baseline differences. By establishing each participant's own performance range as the normalization baseline, the procedure preserved individual physiological response patterns,

enabling meaningful cross-participant comparisons and robust statistical analysis. Consequently, the normalization procedure enhanced the statistical power of the analysis by reducing inter-subject variability, while maintaining the integrity of the fundamental biomechanical relationships under investigation.

Subsequently, the fitting coefficients α and β and correlation coefficients rr were calculated using the normalized capacitance values C_{norm} and normalized torque values NT_{norm}, as denoted in Equations (5.5) and (5.6). This approach ensures a more accurate and reliable analysis of the relationship between pressure changes and muscle force.

$$NT_{norm} = \frac{NT - NT(start)}{\max(NT) - \min(NT)} \tag{5.3}$$

$$C_{norm} = \frac{C - C(start)}{\max(C) - \min(C)} \tag{5.4}$$

$$NT_{norm} = \alpha \times C_{norm} + \beta \tag{5.5}$$

$$rr = \frac{conv(C_{norm}, NT_{norm})}{\sigma(C_{norm}) \times \sigma(NT_{norm})} \tag{5.6}$$

5.4. Clinical Experiments Results Analysis and Discussion

5.4.1. Results analysis

In this study, normalized capacitance values C_{norm} and normalized torque values NT_{norm} were systematically preprocessed for each participant across eight MVIC exercises. The correlation coefficients rr derived from these values serve as indicators of the linear relationship between capacitance and torque, providing insight into the consistency of this relationship across different exercises and participants.

To ensure the robustness and generalizability of the findings, a two-way ANOVA analysis was conducted. This statistical approach allows for the examination of potential effects and interactions between different participants and exercise conditions, thereby verifying the applicability of the results to broader contexts.

Additionally, the assumption of normality for residuals was rigorously tested using histograms, QQ-plots, and the Shapiro–Wilk test. These methods collectively assess whether the residuals from the data are approximately normally distributed, which is a critical assumption for the statistical analyses.

To further validate the clinical experiments, effective sample size calculations were employed. These calculations help determine whether the sample size used in the study is sufficient to support the conclusions drawn, ensuring that the findings are statistically reliable and representative of the population under study.

Specifically, each participant was required to complete eight MVIC exercises, with two exercises performed at each of four different ankle positions: 0°, 10°, 20°, and 30°. The fitting coefficients α and β and correlation coefficients rr between normalized capacitance values C_{norm} and normalized torque values NT_{norm} were calculated with regard to loading phase of each MVIC exercise. The visualization of data for all twelve participants is presented in Figure 5-10.

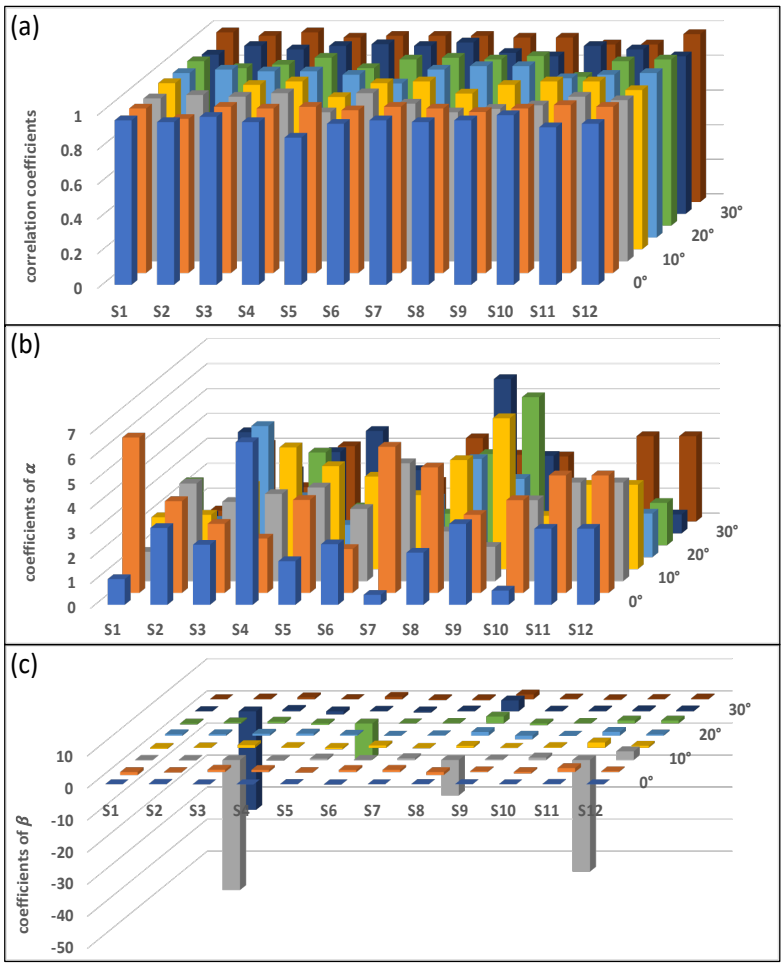

Figure 5-10 The linear regression fitting coefficients and Pearson correlation coefficients across eight MVIC exercises for each participant.

Table 5-2 Summary of the coefficients (α and β) and correlation coefficient for each participant.

Participant	Correlation Coefficient Mean	Correlation Coefficient STD	Alpha Mean	Alpha STD	Beta Mean	Beta STD
Subject_1	0.95	0.02	1.99	1.73	-0.13	0.37
Subject_2	0.92	0.08	2.84	1.02	-3.70	10.20
Subject_3	0.96	0.01	2.85	1.08	-4.58	13.58
Subject_4	0.96	0.01	3.68	1.32	0.01	0.51
Subject_5	0.92	0.05	2.74	1.20	-1.27	3.79
Subject_6	0.95	0.03	2.27	0.72	0.07	0.38
Subject_7	0.96	0.02	2.76	1.75	0.18	0.32
Subject_8	0.94	0.04	3.74	1.37	-0.37	4.22
Subject_9	0.94	0.03	3.57	1.51	-0.09	0.46
Subject_10	0.93	0.04	2.11	0.97	0.09	0.34
Subject_11	0.94	0.02	2.84	1.24	-3.65	11.77
Subject_12	0.94	0.02	2.53	1.81	0.68	0.80

To further analyze the data, the mean and standard deviation of the fitting coefficients α and β and correlation coefficients rr across all eight MVIC exercises for each participant were computed and illustrated in Table 5-2. The results indicate that, for all participants, the mean correlation coefficient exceeds 0.92, with a standard deviation below 0.08, suggesting a strong linear relationship between normalized capacitance and torque values. A two-way ANOVA [302] was conducted to assess the impact of different participants and ankle angles on the correlation coefficients. The analysis revealed no statistically significant differences attributable to either participant factor (p = 0.233) or angular position factor (p = 0.063), nor was there a significant interaction effect between these factors (p = 0.423). This implies a consistent linear relationship between normalized capacitance and torque values, irrespective of participant variability or angular positioning.

Similarly, a two-way ANOVA was employed to evaluate the effects of different participants and ankle angles on the fitting coefficients α and β. The analysis showed no statistically significant differences for coefficients α due to participant factor (p = 0.290) or angular position

factor (p = 0.055), nor was there a significant interaction effect (p = 0.961). For coefficients β, no significant differences were found due to participant factor (p = 0.821) or angular position factor (p = 0.299), with no interaction effect (p = 0.575).

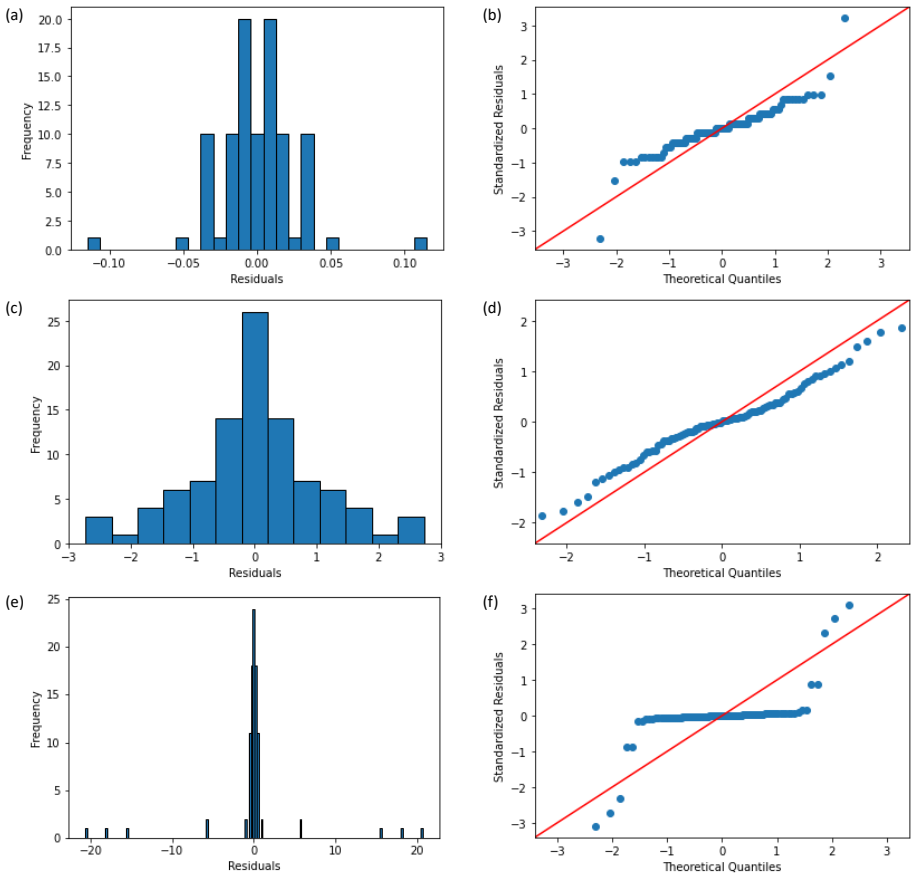

Figure 5-11 Diagnostic plots to visually assess the normality assumptions required for analysis of variance regarding the correlation coefficients rr, the fitting coefficients α and β.

Given the relatively small sample size of twelve participants, the assumption of normality for residuals was tested using histograms, QQ-plots, and the Shapiro-Wilk test for correlation coefficients rr and fitting coefficients α and β, as shown in Figure 5-11. Although the Shapiro-

Wilk test for correlation coefficients rr resulted in rejection ($p = 7\times10^{-7}$), further examination of histograms and residual plots suggested an approximate normal distribution. For fitting coefficients α, the Shapiro-Wilk test did not reject the null hypothesis ($p = 0.169$), indicating a normal distribution. For fitting coefficients β, despite rejection by the Shapiro-Wilk test ($p = 8\times10^{-17}$), histograms and residual plots again suggested approximate normality.

The validity of these findings was assessed through effective sample size calculations [303]. With a significance level of 0.05, a beta of 0.10, and a power of 0.90, assuming correlation coefficients of 0.90 or higher support the null hypothesis of linearity, while 0.80 or lower reject it, the minimal sample size was calculated to be 11. Post-experiment, the mean standard deviation of correlation coefficients was found to be 0.03, indicating the assumed population standard deviation was conservatively larger than the actual ($\sigma = 0.07 > 0.03$). Thus, the sample size requirement was satisfied with the twelve participants recruited for this study.

5.4.2. Results discussion

The integrated smart compression stocking system was developed to monitor lower extremity muscle force, demonstrating a relationship between normalized capacitance and torque values that, while not perfectly linear, achieved correlation coefficients exceeding 0.92. Several physiological and technical factors contribute to the observed nonlinearity in this relationship.

The complex deformation patterns of skeletal muscles during MVIC represent a primary source of nonlinearity. The triceps surae muscle group, consisting of the gastrocnemius medial and

lateral heads, soleus, and plantaris muscles, generates approximately 80% of total plantarflexion force [194, 195], while deeper muscle deformations remain difficult to detect through surface-mounted sensors. Individual variations in exercise comprehension and execution, despite standardized verbal instructions, introduce additional variability between participants and testing sessions.

Technical characteristics of the flexible capacitive pressure sensors also contribute to measurement nonlinearity. The incorporation of carbon black powder into the polydimethylsiloxane matrix and surface roughening of the dielectric layer enhance sensor sensitivity but create irregular microstructures that produce nonlinear capacitance responses to applied pressure. The viscoelastic properties of the sensor materials further contribute to capacitance fluctuations and initial measurement drift.

Statistical analysis of the linear relationship coefficients α revealed standard deviations below 1.81 across participants from Table 5-2, indicating low dispersion between different ankle angle conditions. Two-way ANOVA demonstrated no statistically significant effects of participant factors on the slope coefficients α, though angular position factors approached significance with greater influence on the relationship parameters. Clinical observations confirmed that larger ankle angles increased the difficulty of force generation, consistent with established muscle force-length properties and previous research demonstrating that gastrocnemius and soleus muscles operate on the ascending limb and plateau regions of their force-length curves [304-306].

The intercept coefficients β, representing initial exercise conditions, exhibited values approximating zero across most participants, reflecting the challenge of precisely controlling initial muscle contraction states. Limited analysis was conducted on these parameters due to the practical impossibility of standardizing passive muscle states between individuals.

Study limitations include restricted sensor sensitivity, with capacitance changes of only 2-3 pF during loading phases, necessitating future improvements in sensor matrix design and garment integration. The small cohort of twelve healthy young adults limits generalizability, requiring larger and more diverse populations for enhanced statistical power. Additionally, the reliance on raw capacitance measurements affected by sensor noise and fluctuations suggests future research should incorporate advanced machine learning algorithms for data denoising and outlier management.

5.5. Summary

In this chapter, it was explored about the relationship between pressure changes, measured by the integrated smart compression stocking system, and muscle force, indicated by muscle torque values (*NT*), during isometric contractions. We hypothesized a linear relationship between the system's readout (*C*) and the torque values (*NT*). To quantify this, we calculated fitting and correlation coefficients between normalized readout and torque values during the loading phase of each MVIC exercise.

Twelve healthy young individuals participated, completing eight MVIC exercises at ankle positions of 0°, 10°, 20°, and 30°. These angles were selected to represent varying positions, with 0° as the anatomical baseline. Participants performed MVICs against a fixed lever arm, maintaining contractions for 5 seconds, with rest intervals to prevent fatigue. Data synchronization between the Humac NORM and the Smart Compression Stocking Utility V3 was ensured by an experiment operator.

Analysis revealed a strong linear relationship between normalized readouts and torque values, with correlation coefficients rr averaging above 0.92 and standard deviations below 0.08. A two-way ANOVA showed no significant differences in correlation coefficients due to participant variability ($p = 0.233$) or angular position ($p = 0.063$), nor any interaction effects ($p = 0.423$), indicating consistency across participants and positions.

Further ANOVA analysis on fitting coefficients α showed no significant impact from participant factor ($p = 0.290$) or angular position ($p = 0.055$), and no interaction effects ($p = 0.961$). Similarly, no significant differences were found for coefficients β, with participant factor ($p = 0.821$) and angular position ($p = 0.299$) showing no impact, and no interaction effects ($p = 0.575$).

Given the small sample size, normality of residuals was assessed using histograms, QQ plots, and the Shapiro-Wilk test. Despite deviations suggested by the Shapiro-Wilk test for correlation

coefficients rr (p = 7×10^{-7}), further analysis indicated approximate normality. For fitting coefficients α, the Shapiro-Wilk test supported normal distribution (p = 0.169), and similar findings were observed for coefficients β, despite initial rejection ($p = 8\times10^{-17}$).

Effective sample size calculations confirmed the validity of results, with a minimal sample size of 11 required for a significance level of 0.05 and power of 0.90. The actual mean standard deviation of correlation coefficients was 0.03, supporting the robustness of the findings. Overall, the study suggests a general linear relationship between normalized capacitance and torque values, consistent across participants and ankle positions. Future work will expand participant scope, explore isotonic and isokinetic modes, and develop advanced data processing algorithms for enhanced feature extraction.

Chapter 6 Conclusions, Limitations and Recommendations for Future Work

6.1. Conclusions

This report presents a study on the smart compression garments system design, integration, signal processing, and application for healthcare. A comprehensive review has been conducted on different compression garments and compression therapies, such as chronic venous disease management, scar management, orthopedic application, body shaping application, sportswear application, and other applications. Considering traditional functional compression garments cannot provide real-time pressure measurement and accurate pressure management, smart functional compression garments are highly demanding.

A literature review on signal processing was completed. To deal with deterministic signals, adopted time domain analysis, spatial domain analysis, and frequency domain analysis, incorporate classic Fourier Transform, CTFS, CTFT, DTFS, DTFT, FFT. To deal with stochastic signals, it involves MLE, MAP, and other nonparametric context estimations. Furthermore, to deal with signals with complex features, adopted advanced approaches include time-frequency representation of STFT and Wavelet Transform (CWT, DWT), PSD analysis for stochastic processes and ARIMA. Lastly, to deal with higher-level information of complex signals, Machine Learning and Deep Learning are adopted. Specifically, considering the

complexity of the smart compression garments systems and there is seldom research touching directly on them, the dedicated signal processing method is invaluable for further research.

It then reviewed skeleton muscle anatomy and muscle contraction mechanism, current EMG method and PCSA methods to detect muscle status and their limitations, such as being incapable of acquiring accurate and simultaneous time series data pertaining to human bodies, and less consideration for long-term user comfort. The gastrocnemius muscle is a vital muscle for many daily activities such as maintaining posture, walking, executing dynamic movements, and shock absorbing. Therefore, applying a new smart compression garment system to monitor the gastrocnemius muscle is precious for patients and doctors, promising for research, but also challenging.

Based on the comprehensive literature review, system integration of smart textile-integrated microelectronic systems was completed, including the hardware and software architecture design and implementation. The architecture utilizes off-the-shelf and lower-cost components and commonly used facility tools or platforms so that the system offers high sensitivity for low-pressure detection and maintains accuracy and flexibility for comfortable, long-term use. Its intuitive interface and modular design enable easy integration with existing external systems and support rapid upgrades and repairs. Configurable software and hardware ensure adaptability for various compression therapy applications. The whole system involves compression garments, embedded flexible sensors, edge control units, user interactive devices, software applications, and benefits of BOM cost of 234 RMB or 33 USD.

Signal processing of the smart textile-integrated microelectronic system was completed based on the proposed smart compression garments system. Considering textile flexible sensors are suspectable to noise and fluctuations, deep neural network based encoder decoder architecture has been proposed to denoise with respect to fabricated sensors. For the flat surface pressure, the algorithms achieved the pressure measurement root mean square error of 0.7 mmHg, a 38% increase from that obtained by traditional polynomial regression. After 1000 epochs of fine-tuning for different autoencoder parts, the root mean square error was 0.9 mmHg. For the curve surface pressure, the fabric capacitive pressure sensors demonstrate good long-term (10-day) consistency of data readout and higher sensitivity at the higher curvature. Specifically on the B position, B1 position, C position of the wooden leg, the algorithms achieved the pressure measurement root mean square error of 0.028 mmHg, 0.063 mmHg, 0.039 mmHg, and correspondingly 98%, 97%, 98% increase from that obtained by traditional polynomial regression. The algorithm benefits acceptable computing and storage resource requirements and is suitable for edge deployment.

To validate the clinical efficacy of the smart textile-integrated microelectronic system, a controlled experimental study was conducted to assess gastrocnemius muscle force during maximum voluntary isometric contractions (MVIC) of ankle plantarflexion. The integrated smart compression stocking system was evaluated against established clinical measurement protocols to determine its accuracy and reliability for lower extremity muscle assessment.

Twelve healthy young adults participated in the validation study, performing standardized MVIC ankle plantarflexion exercises under controlled laboratory conditions. Data acquisition was performed simultaneously using both the proposed smart compression stocking system and a calibrated dynamometer (Humac NORM) serving as the gold standard reference. Statistical analysis revealed strong linear correlations between muscle torque measurements and system output readings, with correlation coefficients exceeding 0.92, indicating high measurement fidelity. Two-way analysis of variance (ANOVA) demonstrated that ankle joint angle variations exerted a more significant influence on measurement outcomes ($p = 0.055$) compared to inter-participant variability ($p = 0.290$). These findings suggest that the measurement precision is primarily dependent on biomechanical positioning rather than individual physiological differences. The validation results establish the smart compression stocking system as a viable tool for non-invasive monitoring of lower extremity muscle forces during isometric contractions, with potential applications in clinical rehabilitation and performance assessment.

The thesis culminates in several noteworthy conclusions that not only summarize the key findings but also make substantial contributions to the existing body of knowledge within the relevant scientific domains. The major conclusions can be summarized as follows:

(1) Diverse compression therapy application scenarios have been investigated, which implies that imperceptible, multifunctional, long-term used smart compression garments are highly desirable as they can monitor the variation in pressure and offer information during therapy or advice on how to enhance therapy efficacy.

(2) In-depth review of various signal processing methods to provide guidelines for smart compression garment physical layer design, especially considering fabricated sensors' performance is deteriorated by parasitic capacitances caused by surrounding electromagnetic interference, proximity effects, and deformation on curved surfaces.

(3) A review of muscle contraction mechanisms, popular detection approaches of EMG methods and PCSA methods, and their inevitable limitations highlight the benefits and importance of the application of smart compression garment systems to detect skeleton muscle contraction.

(4) A smart compression garment system has been designed and prototyped, including compression garments, embedded fabric capacitive sensors, edge control units, user interactive devices, and software applications. The components are all available off-the-shelf, commonly used, lower cost of 234 RMB or 33 USD. The whole system has the advantages of flexibility, user-friendliness, modular design, configurable hardware and software.

(5) A unified encoder-decoder MLP architecture was proposed, where encoder parts are obtained from the stacked autoencoder method and decoder parts are trained according to different downstream tasks. The architecture has the advantages of high interpretability, low cost of unsupervised learning, and adaptability to deploy on edge control units which require low computation and storage resources.

(6) The smart compression stockings measurement datasets were established, consisting of 22,498 pairs of data (capacitance versus pressure) regarding flat surface pressure and 75,888 pairs of data (capacitance versus pressure) regarding curved surface pressure.

(7) The proposed deep neural network algorithms were trained and evaluated. The benchmarks were chosen as polynomial methods. Evaluations were around the depth factor of neural networks, the width factor of neural networks, the complexity of neural networks, the interchangeability of encoders, and different datasets of flat surface pressure and curved surface pressure. Although the algorithms need more computations and storage, the algorithms outperform the best polynomial model by 38% accuracy improvement regarding flat surface pressure and outperform the best polynomial models by 98%, 97%, 98%, for the B position, B1 position, C position respectively regarding to curved surface pressure.

(8) The smart compression garment system could be applied for monitoring the skeleton muscle force of lower extremities, which is essential for many daily activities. A clinical validation study was conducted involving twelve healthy participants who engaged in maximum voluntary isometric contractions of ankle plantarflexion under controlled experimental conditions. The analysis yielded correlation coefficients exceeding 0.92, indicating a robust linear relationship between the muscle torque measured and the output from the smart compression stocking system. Further statistical evaluation using two-way analysis of variance revealed that the angular positioning of the ankle joint had a more pronounced effect on measurement outcomes

than inter-participant variability. The influence of joint angle approached statistical significance ($p = 0.055$), whereas the effects related to individual participant differences were not significant ($p = 0.290$). These findings suggest that the measurement system is more responsive to biomechanical changes associated with joint positioning than to the physiological differences among participants. The validation results underscore the clinical utility of the integrated smart compression stocking system for monitoring lower extremity muscle force during isometric contractions. This establishes its potential as a reliable tool for assessing muscle function in both rehabilitation and sports medicine contexts.

6.2. Limitations and Recommendations for Future Work

The research outcomes presented in this study are subject to certain limitations that restrict the generalizability of the obtained results. It is important to acknowledge and consider these limitations when interpreting the findings and applying them to broader contexts. Firstly, the fabric capacitive pressure sensors did not present high sensitivity during clinical experiments. The sensor fabrication through PDMS mixed with CB powder and the dielectric layer roughed by abrasive paper caused the instability of initial capacitance readout drift and capacitance values readout fluctuation when pressure was exerted. This also caused the inconsistency between the different batches of sensor fabrication. Secondly, the research did not concentrate on long-term wearable performance tests and user experience tests, which are highly valuable for patients' real-life usage and can guide the future improvement of sensors and hardware iterative design. Thirdly, proposed encoder-decoder algorithms were not used in the clinical

experiments. This denoise method could stabilize the data stream and reduce the fluctuation and interference from unknown sources. However, this would also bring lower explainability and higher model complexity. Fourthly, 12 healthy people are not enough to evidently prove the generalization of obtained results for a larger population. On the other hand, the Cloud architecture should be adjusted to accommodate millions of users in the future. Online Transaction Processing, Online Analytical Processing, and Big Data mining are supportive technical pillars to realize in the next work. Fifthly, this research only touched the muscle force in isometric mode, rather than other complicated conditions of isotonic mode and isokinetic mode, other complex diseases, syndromes, or high-level information, such as muscle atrophy and muscle hypertrophy detection, myasthenia detection, the elder falling down detection and prediction, chronic venous disease management, scar management, orthopedic application, body shaping application, sportswear application, other applications. The proposed deep learning based unsupervised encoder-decoder architecture could be utilized further and derive the data-driven solution models.

Although the proposed smart compression stocking system presents enormous future-oriented potential, considering the limited time and resources related to completed research work, there are some preliminary works that need to be done in the near future to achieve better system performance and greater user experience. This can further broaden and deepen knowledge related to the smart textile-integrated microelectronic system.

6.2.1. Encoder-decoder model inference for muscle force monitoring

In the research, the smart compression stocking system was applied for monitoring the gastrocnemius muscle force. Data processing was utilized to deal with the fabric pressure sensors' raw capacitance data streaming. However, according to the analysis and experiments results from Chapter 4 Unsupervised Encoder-Decoder for Edge Signal Processing, the linear fitting equation caused pressure measurement root mean square error of 6.4231 mmHg on the flat surface, and caused pressure measurement root mean square error of 3.6445 mmHg, 4.3389 mmHg, 2.4482 mmHg for B position, B1 position, C position respectively on the curve surface. These errors offer plausible explanations of the observed deviations from perfect linearity between normalized capacitance measurements and normalized torque values (the correlation coefficients exceeding 0.92). Nevertheless, the proposed encoder-decoder can reduce pressure measurement error and achieve the root mean square error of 0.7 mmHg for flat surface, and that of 0.028 mmHg, 0.063 mmHg, 0.039 mmHg, for B position, B1 position, C position on curve surface respectively. Therefore, it is feasible with higher confidence to increase the linearity relationship between the system output and muscle torques, by inputting the raw capacitance data streaming into the trained encoder-decoder models and then analyzing the model inference data. The unsupervised encoder-decoder method takes advantage of the lower cost of no human labeling data, simple algorithms, less storage and computation resources needed, and high-speed computing which is tailored for real-time data processing on edge devices. This will transfer the paradigm from hand-crafted complicated data processing algorithms to general deep learning approaches, which can save plenty of intensive labor on deriving close expressions of formulas and improve accuracy by a large margin. However, because different people's legs have different curvatures, the curvature will change during the

muscle contraction and relaxation on the same position of the same person's leg, sensors may slide on the nearby positions which possess different curvatures, hence, this needs more future study to come up with one better neural network model suitable for different situations.

6.2.2. Edge control unit design and integration improvement

In this work, the edge control unit was an essential hardware component to support the whole compression garment system, which realized to read the capacitance values of the flexible pressure sensors and transmit the values to mobile phones through Bluetooth protocol. However, the current edge control unit prototypes were larger in size and heavier weight, which caused the wear discomfort. Edge control unit version 2 was re-designed, re-layout, re-prototype, as shown in Figure 6-1.

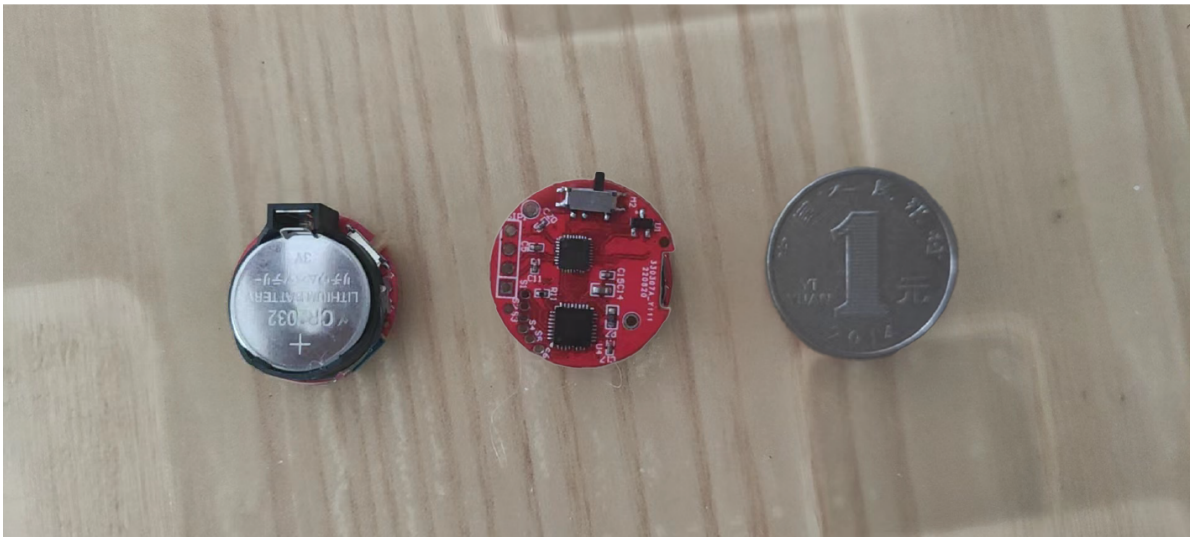

Figure 6-1 Frontside and backside of coin-size edge control unit 2.0 PCBA.

Based on the solution of PCap01 for capacitance measurement, PW02 (Pangwei Link, China) for data transmission through BLE 5.0, CR2032 lithium-ion battery with 225 mAh capacity to power supply. The edge control unit 2.0 was the coin-size and 7 grams weight, which is much lighter to wear and more convenient to integrate with other accessories. In the future, a comprehensive user experience test will be completed around the edge control unit 2.0, as displayed in Figure 6-2.

Figure 6-2 Housing design for edge control unit 2.0.

6.2.3. MetaHealth applications through smart compression garment systems

As smart compression garment systems can be used and integrated into various scenarios, and the metaverse becomes popular and obviously trendy after COVID-19, to combine these technologies can lead to cost-effective MetaHealth, which can benefit a large amount of patients.

Nowadays, the metaverse is widely adopted for collaborative working, education, clinic care, wellness, and monetization through gamification. By developing on the Unity, the MetaHealth can be demonstrated by 4 exemplary rooms in the future research senarios, which are the medical consultation room, smart medical compression stockings room, smart medical glove room, and smart medical facemask room. Based on the proposed Cloud architecture and blockchain, remote medical consultation will be realized, involving 24*7 continuous biometric monitoring, electronic medical records, shared and immutable records, personal data privacy protection, and potential data marketplace across regional healthcare systems when adopting Federated Learning. In the smart medical compression stockings room, more than continuous pressure monitoring and muscle force monitoring, there are more intervention treatments for patients by ankle pumping and leg posture detection. In the smart medical glove room, patients can go through rehabilitation treatment by participating in metaverse games. Moreover, the smart medical glove can benefit remote medical education, including surgery operation education, glove pressure streaming record, freshman training and examination. Finally, in the smart medical facemask room, users can wear a smart medical facemask to continuously monitor breath pressure and encourage them to do lung capacity increase exercise. This is significant for patients who recover from the COVID-19. The MetaHealth is an ongoing project, taking advantage of low-cost and interactive smart compression garment systems, which can help remote patients and is an adding-value supplement to the current healthcare system. The MetaHealth will also explore chronic venous disease management, scar management, orthopedic application, body shaping application, sportswear application, and other applications, where traditional commercial compression garments are widely used, but there

are still huge gaps in users' expectations and traditional commercial compression garments available, as shown in Figure 6-3. This not only highlights the urgency and significance of further academic research but also demonstrates the potential market value of user-centered smart compression garment systems, as shown in Figure 6-4 and Figure 6-5. The MetaHealth needs more study in the future and to analyze objective feedback of patients to improve the user experience at scale.

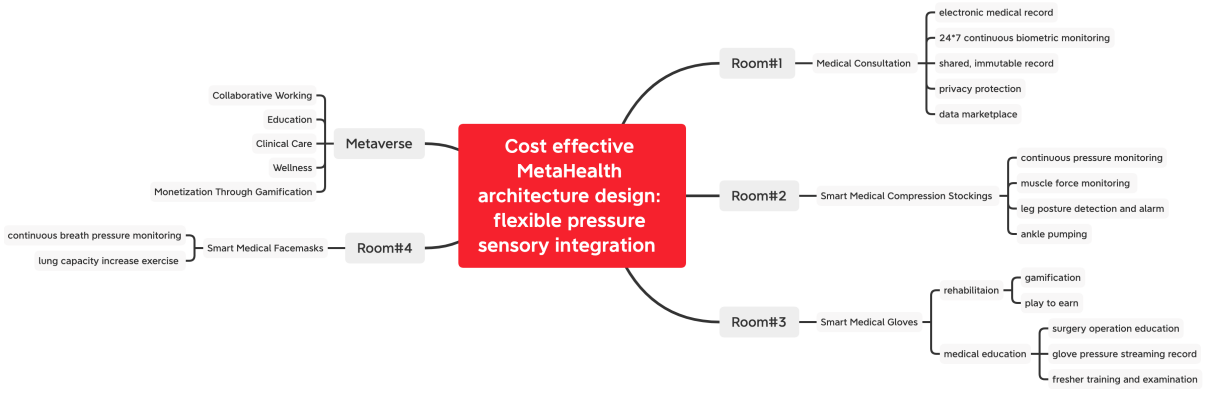

Figure 6-3 Illustration of cost-effective MetaHealth architecture design.

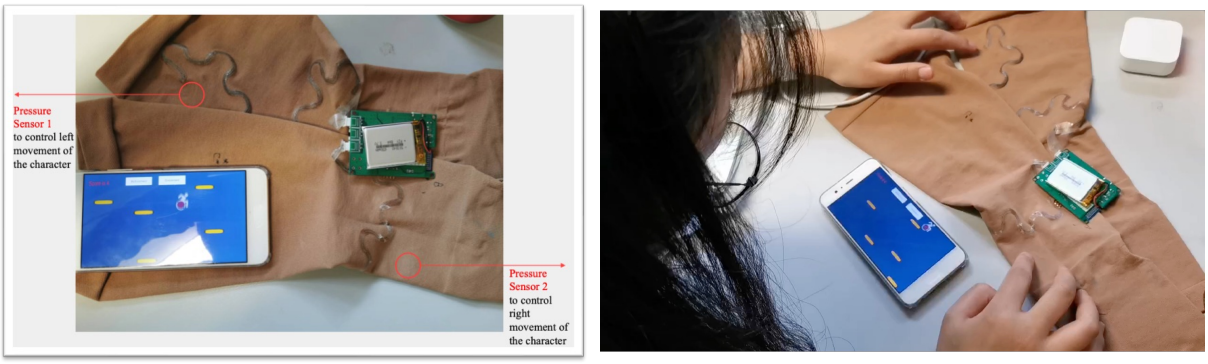

Figure 6-4 Demo of gaming in the MetaHealth.

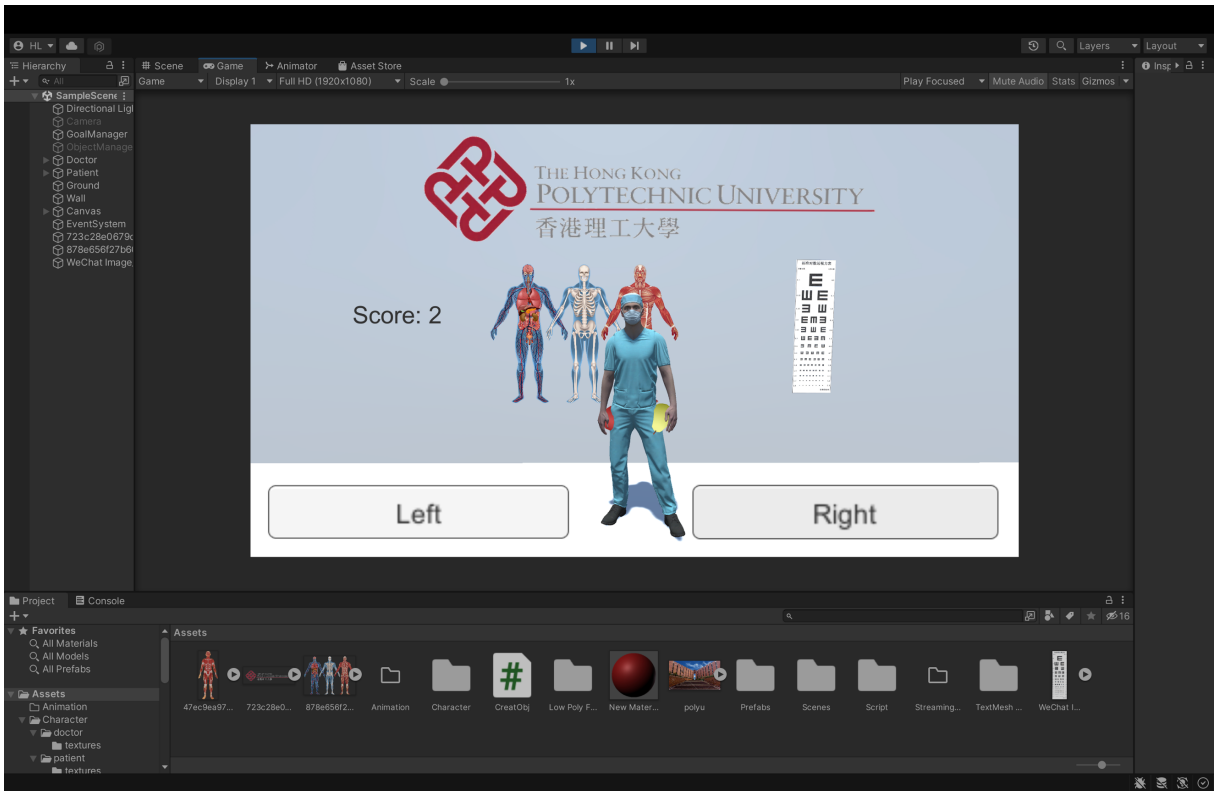

Figure 6-5 The smart medical glove room was developed on Unity.

REFERENCES

[1] D. Gupta, "Functional clothing-Definition and classification," *Indian Journal of Fibre & Textile Research,* vol. 36, no. 4, pp. 321-326, Dec 2011.

[2] Y. Xiong and X. Tao, "Compression garments for medical therapy and sports," *Polymers,* vol. 10, no. 6, p. 663, 2018.

[3] B. A. MacRae, J. D. Cotter, and R. M. Laing, "Compression garments and exercise," *Sports medicine,* vol. 41, no. 10, pp. 815-843, 2011.

[4] L. Wang, M. Felder, and J. Y. Cai, "Study of properties of medical compression garment fabrics," *Journal of Fiber Bioengineering and Informatics,* vol. 4, no. 1, pp. 15-22, 2011.

[5] I. Iniesta, "Hippocratic Corpus," *BMJ: British Medical Journal (Online),* vol. 342, 2011.

[6] G. Lippi, E. J. Favaloro, and G. Cervellin, "Prevention of venous thromboembolism: focus on mechanical prophylaxis," in *Seminars in thrombosis and hemostasis*, 2011, vol. 37, no. 03, pp. 237-251.

[7] H. A. Martin, "The india-rubber bandage for ulcers and other diseases of the legs," *British Medical Journal,* vol. 2, no. 930, p. 624, 1878.

[8] C. L. Felty and T. W. Rooke, "Compression therapy for chronic venous insufficiency," in *Seminars in vascular surgery*, 2005, vol. 18, no. 1, pp. 36-40.

[9] M. J. Staley and R. L. Richard, "Use of pressure to treat hypertrophic burn scars," *Advances in wound care: the journal for prevention and healing,* vol. 10, no. 3, pp. 44-46, 1997.

[10] S. Tanaka, T. Midorikawa, and H. Tokura, "Effects of pressure exerted on the skin by elastic cord on the core temperature, body weight loss and salivary secretion rate at 35 C," *European journal of applied physiology,* vol. 96, no. 4, pp. 471-476, 2006.

[11] D.-P. Born, B. Sperlich, and H.-C. Holmberg, "Bringing light into the dark: effects of compression clothing on performance and recovery," *International journal of sports physiology and performance,* vol. 8, no. 1, pp. 4-18, 2013.

[12] W. Fu, Y. Liu, and Y. Fang, "Research advancements in humanoid compression garments in sports," *International Journal of Advanced Robotic Systems,* vol. 10, no. 1, p. 66, 2013.

[13] O. Troynikov, E. Ashayeri, M. Burton, A. Subic, F. Alam, and S. Marteau, "Factors influencing the effectiveness of compression garments used in sports," *Procedia Engineering,* vol. 2, no. 2, pp. 2823-2829, 2010.

[14] R. Duffield and M. Portus, "Comparison of three types of full-body compression garments on throwing and repeat-sprint performance in cricket players," *British journal of sports medicine,* vol. 41, no. 7, pp. 409-414, 2007.

[15] C. C. Wang and K. Tang, "Pattern computation for compression garment by a physical/geometric approach," *Computer-Aided Design,* vol. 42, no. 2, pp. 78-86, 2010.

[16] J. A. Hill, G. Howatson, K. A. Van Someren, S. Davidson, and C. R. Pedlar, "The variation in pressures exerted by commercially available compression garments," *Sports Engineering,* vol. 18, no. 2, pp. 115-121, 2015.

[17] J. Raffetto and F. Mannello, "Pathophysiology of chronic venous disease," *International angiology: a journal of the International Union of Angiology,* vol. 33, no. 3, pp. 212-221, 2014.
[18] R. T. Eberhardt and J. D. Raffetto, "Chronic venous insufficiency," *Circulation,* vol. 130, no. 4, pp. 333-346, 2014.
[19] L. Robertson, C. a. Evans, and F. Fowkes, "Epidemiology of chronic venous disease," *Phlebology,* vol. 23, no. 3, pp. 103-111, 2008.
[20] A. Jawien, "The influence of environmental factors in chronic venous insufficiency," *Angiology,* vol. 54, no. 1_suppl, pp. S19-S31, 2003.
[21] A. N. Nicolaides *et al.*, "Management of chronic venous disorders of the lower limbs guidelines according to scientific evidence," *International angiology,* vol. 27, no. 1, p. 1, 2008.
[22] G. S. Barron, S. E. Jacob, and R. S. Kirsner, "Dermatologic complications of chronic venous disease: medical management and beyond," *Annals of vascular surgery,* vol. 21, no. 5, pp. 652-662, 2007.
[23] P. L. Antignani, "Classification of chronic venous insufficiency: a review," *Angiology,* vol. 52, no. 1_suppl, pp. S17-S26, 2001.
[24] M. H. Meissner *et al.*, "Primary chronic venous disorders," *Journal of vascular surgery,* vol. 46, no. 6, pp. S54-S67, 2007.
[25] C.-M. Fan, "Venous pathophysiology," in *Seminars in interventional radiology*, 2005, vol. 22, no. 03, pp. 157-161.
[26] E. P. Bachelor, "Varicose veins and telangiectasias: Diagnosis and treatment," *Plastic and Reconstructive Surgery,* vol. 108, no. 2, pp. 572-573, 2001.
[27] J. Schuren and K. Mohr, "Pascal's law and the dynamics of compression therapy: a study on healthy volunteers," *International angiology,* vol. 29, no. 5, p. 431, 2010.
[28] X. Dai, Y. Li, R. Liu, and Y. L. Kwok, "Part 4: Biomechanical engineering of compression stockings," in *Biomechanical Engineering of Textiles and Clothing*: Woodhead Publishing Ltd., 2006, pp. 332-346.
[29] J. Hill, G. Howatson, K. van Someren, S. Davidson, and C. Pedlar, "Pressures exerted by commercially available lower limb compression garments," *British Journal of Sports Medicine,* vol. 48, no. 7, pp. 608-608, 2014.
[30] F. Amsler and W. Blättler, "Compression therapy for occupational leg symptoms and chronic venous disorders–a meta-analysis of randomised controlled trials," *European Journal of Vascular and Endovascular Surgery,* vol. 35, no. 3, pp. 366-372, 2008.
[31] H. Partsch *et al.*, "Classification of compression bandages: practical aspects," *Dermatologic surgery,* vol. 34, no. 5, pp. 600-609, 2008.
[32] M. S. Weingarten, "State-of-the-art treatment of chronic venous disease," *Clinical infectious diseases,* pp. 949-954, 2001.
[33] H. Partsch, R. Damstra, and G. Mosti, "Dose finding for an optimal compression pressure to reduce chronic edema of the extremities," *International angiology: a journal of the International Union of Angiology,* vol. 30, no. 6, pp. 527-533, 2011.
[34] H. Partsch, "Compression therapy: clinical and experimental evidence," *Annals of vascular diseases,* vol. 5, no. 4, pp. 416-422, 2012.

[35] B. Partsch and H. Partsch, "Calf compression pressure required to achieve venous closure from supine to standing positions," *Journal of vascular surgery,* vol. 42, no. 4, pp. 734-738, 2005.
[36] A. D. Widgerow and L. A. Chait, "Scar management practice and science: a comprehensive approach to controlling scar tissue and avoiding hypertrophic scarring," *Advances in Skin & Wound Care,* vol. 24, no. 12, pp. 555-561, 2011.
[37] G. G. Gauglitz, H. C. Korting, T. Pavicic, T. Ruzicka, and M. G. Jeschke, "Hypertrophic scarring and keloids: pathomechanisms and current and emerging treatment strategies," *Mol Med,* vol. 17, no. 1, pp. 113-125, 2011.
[38] F. Renò *et al.*, "In vitro mechanical compression induces apoptosis and regulates cytokines release in hypertrophic scars," *Wound repair and regeneration,* vol. 11, no. 5, pp. 331-336, 2003.
[39] H. Partsch and P. Mortimer, "Compression for leg wounds," *British Journal of Dermatology,* vol. 173, no. 2, pp. 359-369, 2015.
[40] E. Van den Kerckhove *et al.*, "The assessment of erythema and thickness on burn related scars during pressure garment therapy as a preventive measure for hypertrophic scarring," *Burns,* vol. 31, no. 6, pp. 696-702, 2005.
[41] J. M. Zurada, D. Kriegel, and I. C. Davis, "Topical treatments for hypertrophic scars," *Journal of the American Academy of Dermatology,* vol. 55, no. 6, pp. 1024-1031, 2006.
[42] P. A. Sharp, B. Pan, K. P. Yakuboff, and D. Rothchild, "Development of a best evidence statement for the use of pressure therapy for management of hypertrophic scarring," *Journal of Burn Care & Research,* vol. 37, no. 4, pp. 255-264, 2016.
[43] J. Johnson, B. Greenspan, D. Gorga, W. Nagler, and C. Goodwin, "Compliance with pressure garment use in burn rehabilitation," *The Journal of burn care & rehabilitation,* vol. 15, no. 2, pp. 181-188, 1994.
[44] I. Parry, C. Hanley, J. Niszczak, S. Sen, T. Palmieri, and D. Greenhalgh, "Harnessing the transparent face orthosis for facial scar management: a comparison of methods," *Burns,* vol. 39, no. 5, pp. 950-956, 2013.
[45] B. Rogers *et al.*, "Computerized manufacturing of transparent face masks for the treatment of facial scarring," *The Journal of burn care & rehabilitation,* vol. 24, no. 2, pp. 91-96, 2003.
[46] C. Yip, Z. Mehmood, and M. Shah, "Lego as a customisable pressure garment insert," *Burns: Journal of the International Society for Burn Injuries,* vol. 34, no. 3, pp. 430-431, 2008.
[47] K. LáZáR, "Application of knitted fabrics in technical and medical textiles," in *Proceedings of the 45th International Congress (IFKT)*, Ljubljana, Slovenia, 2010, pp. 27-29.
[48] D. Ališauskienė, D. Mikučionienė, and L. Milašiute, "Influence of inlay-yarn properties and insertion density on the compression properties of knitted orthopaedic supports," *Fibres & Textiles in Eastern Europe,* no. 6 (102), pp. 74--78, 2013.
[49] D. Guptaa, "Functional clothing—Definition and classification," *Indian Journal of Fibre & Textile Research,* vol. 36, pp. 321-326, 2011.

[50] D. Mikučionienė and L. Milašiūtė, "Influence of knitted orthopaedic support construction on compression generated by the support," *Journal of Industrial Textiles,* vol. 47, no. 4, pp. 551-566, 2017.
[51] A. Chan, "Effect of clothing pressure on the tightness sensation of girdles," *International Journal of Clothing Science and Technology,* vol. 14, no. 2, pp. 100-110, 2002.
[52] H. Makabe, H. Momota, T. Mitsuno, and K. Ueda, "A study of clothing pressure developed by the girdle," *Journal of the Japan Research Association for Textile End-Uses,* vol. 32, no. 9, pp. 424-438, 1991.
[53] B. DOAN *et al.*, "Evaluation of a lower-body compression garment," *Journal of sports sciences,* vol. 21, no. 8, pp. 601-610, 2003.
[54] B. Sperlich, M. Haegele, S. Achtzehn, J. Linville, H.-C. Holmberg, and J. Mester, "Different types of compression clothing do not increase sub-maximal and maximal endurance performance in well-trained athletes," *Journal of sports sciences,* vol. 28, no. 6, pp. 609-614, 2010.
[55] W. J. Kraemer *et al.*, "Continuous compression as an effective therapeutic intervention in treating eccentric-exercise-induced muscle soreness," *Journal of Sport Rehabilitation,* vol. 10, no. 1, pp. 11-23, 2001.
[56] W. J. Kraemer *et al.*, "Effects of a whole body compression garment on markers of recovery after a heavy resistance workout in men and women," *The Journal of Strength & Conditioning Research,* vol. 24, no. 3, pp. 804-814, 2010.
[57] A. T. Scanlan, B. J. Dascombe, P. R. Reaburn, and M. Osborne, "The effects of wearing lower-body compression garments during endurance cycling," *International journal of sports physiology and performance,* vol. 3, no. 4, pp. 424-438, 2008.
[58] A. J. Pearce, D. J. Kidgell, L. A. Grikepelis, and J. S. Carlson, "Wearing a sports compression garment on the performance of visuomotor tracking following eccentric exercise: A pilot study," *Journal of Science and medicine in Sport,* vol. 12, no. 4, pp. 500-502, 2009.
[59] T. Higgins, G. A. Naughton, and D. Burgess, "Effects of wearing compression garments on physiological and performance measures in a simulated game-specific circuit for netball," *Journal of Science and Medicine in Sport,* vol. 12, no. 1, pp. 223-226, 2009.
[60] C. A. da Silva, L. Helal, R. P. da Silva, K. C. Belli, D. Umpierre, and R. Stein, "Association of lower limb compression garments during high-intensity exercise with performance and physiological responses: a systematic review and meta-analysis," *Sports medicine,* vol. 48, pp. 1859-1873, 2018.
[61] D.-F. Xu, D.-Y. Liu, and Z.-M. Wu, "Analysis of physiological response by pressure developed by female swimsuit," *Journal of Beijing Institute of Clothing Technology (Natural Science Edition),* 2012.
[62] H. MOROOKA, M. NAKAHASHI, H. MOROOKA, and K. KITAMURA, "Effects of clothing pressure exerted on a trunk on heart rate, blood pressure, skin blood flow and respiratory function," *Sen'i Kikai Gakkaishi (Journal of the Textile Machinery Society of Japan),* vol. 54, no. 2, pp. 57-62, 2001.

[63] G. B. Curtis and J. Schuler, *Your pregnancy week by week*. Da Capo Lifelong Books, 2016.
[64] M. T. Woo, K. Davids, J. Y. Chow, and T. Jaakkola, "Acute effects of wearing compression knee-length socks on ankle joint position sense in community-dwelling older adults," *Plos one,* vol. 16, no. 2, p. e0245979, 2021.
[65] M. T. Woo, K. Davids, J. Liukkonen, J. Y. Chow, and T. Jaakkola, "Immediate effects of wearing knee length socks differing in compression level on postural regulation in community-dwelling, healthy, elderly men and women," *Gait & Posture,* vol. 66, pp. 63-69, 2018.
[66] K. Baige, F. Noé, N. Bru, and T. Paillard, "Effects of compression garments on balance control in young healthy active subjects: a hierarchical cluster analysis," *Frontiers in Human Neuroscience,* vol. 14, p. 582514, 2020.
[67] E.-J. Jeon, H.-C. You, D.-M. Kim, and H.-E. Kim, "Market survey and motion characteristics research on fitness compression wear to improve muscle efficiency for the elderly," *Fashion & Textile Research Journal,* vol. 20, no. 3, pp. 343-352, 2018.
[68] M. T. Woo, "The influence of wearable garments on postural regulation and joint position sense action in elderly individuals," *Ph.D. dissertation,* 2020.
[69] A. Belbasis, F. K. Fuss, and J. Sidhu, "Muscle activity analysis with a smart compression garment," *Procedia Engineering,* vol. 112, pp. 163-168, 2015.
[70] A. Belbasis and F. K. Fuss, "Development of next-generation compression apparel," *Procedia Technology,* vol. 20, pp. 85-90, 2015.
[71] A. Belbasis, F. K. Fuss, and J. Sidhu, "Estimation of cruciate ligament forces via smart compression garments," *Procedia Engineering,* vol. 112, pp. 169-174, 2015.
[72] A. BELBASIS, "Muscle and soft tissue monitoring via smart compression garments," Ph.D. dissertation, RMIT University.
[73] B. Greenspan and M. A. Lobo, "Design and initial testing of an affordable and accessible smart compression garment to measure physical activity using conductive paint stretch sensors," *Multimodal Technologies and Interaction,* vol. 4, no. 3, p. 45, 2020.
[74] C. Gonçalves, A. F. da Silva, R. Simoes, J. Gomes, L. Stirling, and B. Holschuh, "Design and characterization of an active compression garment for the upper extremity," *IEEE/ASME Transactions on Mechatronics,* vol. 24, no. 4, pp. 1464-1472, 2019.
[75] C. Gonçalves, A. F. da Silva, and R. Simoes, "Wearable textile elongation sensor," in *Proc. 5th Int. Conf. Integrity Reliability, and Failure (IFRF)*, Lyon, France, 2016, pp. 90-95.
[76] S. T. Yang *et al.*, "An active compression sleeve with variable pressure levels using a wire-fabric mechanism and a soft sensor," *Smart Materials and Structures,* vol. 28, no. 11, p. 114002, 2019.
[77] I. Swain, "The measurement of interface pressure," in *Pressure ulcer research: Current and future perspectives*. A. Smith and B. Jones, Eds. New York, NY, USA: Springer, 2005, pp. 51-71.

[78] C. Zhi, S. Shi, Y. Si, B. Fei, H. Huang, and J. Hu, "Recent progress of wearable piezoelectric pressure sensors based on nanofibers, yarns, and their fabrics via electrospinning," *Advanced Materials Technologies,* vol. 8, no. 5, p. 2201161, 2023.
[79] C. Garcia, I. Trendafilova, R. G. de Villoria, and J. S. del Rio, "Self-powered pressure sensor based on the triboelectric effect and its analysis using dynamic mechanical analysis," *Nano Energy,* vol. 50, pp. 401-409, 2018.
[80] H. Lei, Y. Chen, Z. Gao, Z. Wen, and X. Sun, "Advances in self-powered triboelectric pressure sensors," *Journal of Materials Chemistry A,* vol. 9, no. 36, pp. 20100-20130, 2021.
[81] J. h. Li, J. h. Chen, and F. Xu, "Sensitive and wearable optical microfiber sensor for human health monitoring," *Advanced Materials Technologies,* vol. 3, no. 12, p. 1800296, 2018.
[82] E. Vorathin, Z. Hafizi, N. Ismail, and M. Loman, "Review of high sensitivity fibre-optic pressure sensors for low pressure sensing," *Optics & Laser Technology,* vol. 121, p. 105841, 2020.
[83] S. Han *et al.*, "High‐performance pressure sensors based on 3D microstructure fabricated by a facile transfer technology," *Advanced Materials Technologies,* vol. 4, no. 5, p. 1800640, 2019.
[84] Y. Pang *et al.*, "Epidermis microstructure inspired graphene pressure sensor with random distributed spinosum for high sensitivity and large linearity," *ACS nano,* vol. 12, no. 3, pp. 2346-2354, 2018.
[85] J. Shi *et al.*, "Multiscale hierarchical design of a flexible piezoresistive pressure sensor with high sensitivity and wide linearity range," *Small,* vol. 14, no. 27, p. 1800819, 2018.
[86] S. Peng, P. Blanloeuil, S. Wu, and C. H. Wang, "Rational design of ultrasensitive pressure sensors by tailoring microscopic features," *Advanced Materials Interfaces,* vol. 5, no. 18, p. 1800403, 2018.
[87] X. Chen *et al.*, "Highly compressible and robust polyimide/carbon nanotube composite aerogel for high-performance wearable pressure sensor," *ACS applied materials & interfaces,* vol. 11, no. 45, pp. 42594-42606, 2019.
[88] L.-Q. Tao *et al.*, "Graphene-paper pressure sensor for detecting human motions," *ACS nano,* vol. 11, no. 9, pp. 8790-8795, 2017.
[89] Z. Yang *et al.*, "Graphene textile strain sensor with negative resistance variation for human motion detection," *ACS nano,* vol. 12, no. 9, pp. 9134-9141, 2018.
[90] L. Wang, K. Wang, Z. Lou, K. Jiang, and G. Shen, "Plant‐based modular building blocks for "green" electronic skins," *Advanced Functional Materials,* vol. 28, no. 51, p. 1804510, 2018.
[91] M. Liu *et al.*, "Large‐area all‐textile pressure sensors for monitoring human motion and physiological signals," *Advanced materials,* vol. 29, no. 41, p. 1703700, 2017.
[92] J. Lekkala, "Plantar shear stress measurements—A review," *Clinical Biomechanics,* vol. 29, no. 5, pp. 475-483, 2014.
[93] A. Fiorillo, C. Critello, and S. Pullano, "Theory, technology and applications of piezoresistive sensors: A review," *Sensors and Actuators A: Physical,* vol. 281, pp. 156-175, 2018.

[94] J. Li, L. Fang, B. Sun, X. Li, and S. H. Kang, "Recent progress in flexible and stretchable piezoresistive sensors and their applications," *Journal of the Electrochemical Society,* vol. 167, no. 3, p. 037561, 2020.
[95] J. Wang *et al.*, "A highly sensitive and flexible pressure sensor with electrodes and elastomeric interlayer containing silver nanowires," *Nanoscale,* vol. 7, no. 7, pp. 2926-2932, 2015.
[96] S. Bilent, T. H. N. Dinh, E. Martincic, and P.-Y. Joubert, "Porous polymer based flexible pressure sensors for medical applications," in *Proceedings*, 2018, vol. 60, no. 1: MDPI.
[97] S. Bilent, T. H. N. Dinh, E. Martincic, and P.-Y. Joubert, "Influence of the porosity of polymer foams on the performances of capacitive flexible pressure sensors," *Sensors,* vol. 19, no. 9, p. 1968, 2019.
[98] J. Lee *et al.*, "Conductive fiber‐based ultrasensitive textile pressure sensor for wearable electronics," *Advanced materials,* vol. 27, no. 15, pp. 2433-2439, 2015.
[99] A. Chhetry, H. Yoon, and J. Y. Park, "A flexible and highly sensitive capacitive pressure sensor based on conductive fibers with a microporous dielectric for wearable electronics," *Journal of Materials Chemistry C,* vol. 5, no. 38, pp. 10068-10076, 2017.
[100] Z. He *et al.*, "Capacitive pressure sensor with high sensitivity and fast response to dynamic interaction based on graphene and porous nylon networks," *ACS applied materials & interfaces,* vol. 10, no. 15, pp. 12816-12823, 2018.
[101] J. C. Yang *et al.*, "Microstructured porous pyramid-based ultrahigh sensitive pressure sensor insensitive to strain and temperature," *ACS applied materials & interfaces,* vol. 11, no. 21, pp. 19472-19480, 2019.
[102] S. R. A. Ruth, L. Beker, H. Tran, V. R. Feig, N. Matsuhisa, and Z. Bao, "Rational design of capacitive pressure sensors based on pyramidal microstructures for specialized monitoring of biosignals," *Advanced functional materials,* vol. 30, no. 29, p. 1903100, 2020.
[103] C. M. Boutry *et al.*, "A hierarchically patterned, bioinspired e-skin able to detect the direction of applied pressure for robotics," *Science Robotics,* vol. 3, no. 24, p. eaau6914, 2018.
[104] Y. Luo *et al.*, "Flexible capacitive pressure sensor enhanced by tilted micropillar arrays," *ACS applied materials & interfaces,* vol. 11, no. 19, pp. 17796-17803, 2019.
[105] L. Ma *et al.*, "Highly sensitive flexible capacitive pressure sensor with a broad linear response range and finite element analysis of micro-array electrode," *Journal of Materiomics,* vol. 6, no. 2, pp. 321-329, 2020.
[106] J. Yang *et al.*, "Flexible, tunable, and ultrasensitive capacitive pressure sensor with microconformal graphene electrodes," *ACS applied materials & interfaces,* vol. 11, no. 16, pp. 14997-15006, 2019.
[107] Y. Quan *et al.*, "Highly sensitive and stable flexible pressure sensors with micro-structured electrodes," *Journal of Alloys and Compounds,* vol. 699, pp. 824-831, 2017.
[108] H. Kim *et al.*, "Transparent, flexible, conformal capacitive pressure sensors with nanoparticles," *Small,* vol. 14, no. 8, p. 1703432, 2018.

[109] Y. Xiong, "Pressure management for medical compression stockings: prediction, computer integrated manufacturing and pressure monitoring by fabric sensors," Ph.D. dissertation, Hong Kong Polytechnic University, 2022.
[110] Y. Wan *et al.*, "A highly sensitive flexible capacitive tactile sensor with sparse and high‐aspect‐ratio microstructures," *Advanced Electronic Materials,* vol. 4, no. 4, p. 1700586, 2018.
[111] W. Yang, Y. Liu, W. Xu, and H.-Y. Nie, "Design and fabrication of flexible capacitive sensor with cellular structured dielectric layer via 3D printing," *IEEE Sensors Journal,* vol. 21, no. 9, pp. 10473-10482, 2021.
[112] S. R. A. Ruth, V. R. Feig, H. Tran, and Z. Bao, "Microengineering pressure sensor active layers for improved performance," *Advanced Functional Materials,* vol. 30, no. 39, p. 2003491, 2020.
[113] H. Wang *et al.*, "Flexible capacitive pressure sensors for wearable electronics," *Journal of materials chemistry.,* vol. 10, no. 5, pp. 1594-1605, 2022.
[114] T. Hua *et al.*, "A sensitivity-optimized flexible capacitive pressure sensor with cylindrical ladder microstructural dielectric layers," *Sensors,* vol. 23, no. 9, p. 4323, 2023.
[115] S.-W. Kim *et al.*, "A highly sensitive and flexible capacitive pressure sensor based on alignment airgap dielectric," *Sensors,* vol. 22, no. 19, p. 7390, 2022.
[116] Q. Yu and J. Zhang, "Flexible capacitive pressure sensor based on a double-sided microstructure porous dielectric layer," *Micromachines,* vol. 14, no. 1, p. 111, 2022.
[117] Y. Chen, P. Zhang, Y. Li, K. Zhang, J. Su, and L. Huang, "Flexible capacitive pressure sensor based on multi-walled carbon nanotubes microstructure electrodes," *Journal of Physics D: Applied physics,* vol. 54, no. 15, p. 155101, 2021.
[118] Y. Zhao *et al.*, "Highly sensitive and flexible capacitive pressure sensors combined with porous structure and hole array using sacrificial templates and laser ablation," *Polymers,* vol. 16, no. 16, p. 2369, 2024.
[119] Y. Shi *et al.*, "Flexible capacitive pressure sensor based on microstructured composite dielectric layer for broad linear range pressure sensing applications," *Micromachines,* vol. 13, no. 2, p. 223, 2022.
[120] K. Zhao *et al.*, "Highly sensitive and flexible capacitive pressure sensors based on vertical graphene and micro-pyramidal dielectric layer," *Nanomaterials,* vol. 13, no. 4, p. 701, 2023.
[121] H. Cui *et al.*, "A sensitive and flexible capacitive pressure sensor based on a porous hollow hemisphere dielectric layer," *Micromachines,* vol. 14, no. 3, p. 662, 2023.
[122] T.-H. Nguyen, B.-V. Ngo, T.-N. Nguyen, and C. C. Vu, "Flexible pressure sensors and machine learning algorithms for human walking phase monitoring," *Micromachines,* vol. 14, no. 7, p. 1411, 2023.
[123] L. Xia *et al.*, "High-Performance Flexible Capacitive Pressure Sensor Based on a Spiked Nickel/Polyimide Composite Nanofiber Membrane," *ACS sensors.,* vol. 10, no. 2, pp. 1450-1460, 2025.

[124] J. Wang, H. Sun, S. Chen, C. Xu, and Z. Wang, "Flexible capacitive pressure sensors with porous double microstructured layers," *Matéria (Rio de Janeiro),* vol. 29, no. 3, p. e20230344, 2024.
[125] R. Lan *et al.*, "High-sensitivity flexible capacitive pressure sensors based on biomimetic hibiscus flower microstructures," *ACS omega,* vol. 9, no. 12, pp. 13704-13713, 2024.
[126] H. Yu *et al.*, "Wide-range flexible capacitive pressure sensors based on dielectrics with various porosity," *Micromachines,* vol. 13, no. 10, p. 1588, 2022.
[127] S. Pandey and S. K. Mandal, "Development and Assessment of Highly Sensitive, Economically Viable, and Environmentally Sustainable Fabric-Based Flexible Capacitive Pressure Sensors," *Journal of Techniques,* vol. 7, no. 1, pp. 19-27, 2025.
[128] M. Chen *et al.*, "Novel flexible capacitive pressure sensor with a wide detection range enabled by carboxyl iron particle-paraffin wax/silicone composite," *Composites Communications,* vol. 47, p. 101884, 2024.
[129] C.-K. Lim, "Enhancing Sensing Performance of Capacitive Sensors Using Kirigami Structures," *Sensors,* vol. 24, no. 21, p. 6930, 2024.
[130] V. Sravani and S. K. Venkata, "An improved capacitance pressure sensor with a novel electrode design," *Sensors and Actuators A: Physical,* vol. 332, p. 113112, 2021.
[131] S. Y. Joo *et al.*, "Clinical utility of the portable pressure-measuring device for compression garment pressure measurement on hypertrophic scars by burn injury during compression therapy," *Journal of Clinical Medicine,* vol. 11, no. 22, p. 6743, 2022.
[132] H. Ugra, C. Monteverdi, R. Polino, J. Bishop, J. Buckley, and A. Gorea, "Comparison of two pressure sensors used for evaluating performance of compression apparel," in *International Textile and Apparel Association Annual Conference Proceedings*, 2024, vol. 80, no. 1.
[133] C. Wang, X. Wang, Q. Li, and X. Tao, "Recognizing and predicting muscular fatigue of biceps brachii in motion with novel fabric strain sensors based on machine learning," *Biomedical Signal Processing and Control,* vol. 96, p. 106647, 2024.
[134] L. Gao *et al.*, "High-mechanical-resolution pressure sensor based on melt-blown fibers in integrated wearable mask for respiratory monitoring," *IEEE Transactions on Electron Devices,* vol. 68, no. 11, pp. 5765-5772, 2021.
[135] M. Akay, *Detection and estimation methods for biomedical signals*. Academic Press, Inc., 1996.
[136] H. J. Hermens, B. Commission of the European Communities, P. Health Research, and S. project, *European recommendations for surface electromyography : results of the SENIAM project*, 2nd ed. The Netherlands : Roessingh Research and Development, 1999.
[137] R. Merletti and P. A. Parker, *Electromyography : physiology, engineering, and noninvasive applications*. Hoboken, NJ, USA: IEEE/Wiley-Interscience, 2004.
[138] H. Hu, J.-J. Ding, K.-H. Lin, and W.-C. Yang, "Freezing of gaits detection for Parkinson's disease patients using fast time-frequency analysis methods and onset detection," in *2014 IEEE International Conference on Consumer Electronics-Taiwan*, 2014: IEEE, pp. 191-192.

[139] B. Dong, J. Yang, Y. Ma, and X. Zhang, "Medical monitoring model of internet of things based on the adaptive threshold difference algorithm," *International Journal of Multimedia and Ubiquitous Engineering,* vol. 11, no. 5, pp. 75-82, 2016.
[140] O. Valenzuela, B. Prieto, E. Delgado-Marquez, H. Pomares, and I. Rojas, "Wearable intelligent system for the diagnosis of cardiac diseases working in real time and with low energy cost," in *Proceedings*, 2018, vol. 2, no. 19: MDPI, p. 513.
[141] A. V. Oppenheim, *Signals and systems*, 2nd ed. Upper Saddle River, NJ, USA: Prentice Hall, 1997.
[142] A. V. Oppenheim, *Discrete-time signal processing*. Pearson Education India, 1999.
[143] L. Shu, X. Tao, and D. D. Feng, "Intelligent footwear system for continuous dynamic Foot monitoring in daily activities based on fabric pressure sensors," in *International Symposium on New Frontiers in Fiber Materials Science 2011*, 2011: Fiber Society.
[144] L. Shu, T. Hua, Y. Wang, Q. Li, D. D. Feng, and X. Tao, "In-shoe plantar pressure measurement and analysis system based on fabric pressure sensing array," *IEEE Transactions on information technology in biomedicine,* vol. 14, no. 3, pp. 767-775, 2010.
[145] C. W. Therrien, *Discrete random signals and statistical signal processing*. Prentice Hall PTR, 1992.
[146] C.-Y. Chi, C.-H. Chen, C.-C. Feng, and C.-Y. Chen, "Fundamentals of statistical signal processing," *Blind Equalization and System Identification: Batch Processing Algorithms, Performance and Applications,* pp. 83-182, 2006.
[147] R. J. Larsen, *An introduction to mathematical statistics and its applications*, Sixth ed. Boston, MA, USA: Pearson, 2018.
[148] G. Casella, *Statistical inference*, 2nd ed. Pacific Grove, Calif.: Duxbury/Thomson Learning, 2002.
[149] H.-Y. Gao and A. G. Bruce, "Waveshrink with firm shrinkage," *Statistica Sinica,* vol. 7, pp. 855-874, 1997.
[150] R. R. Coifman, Y. Meyer, S. Quake, and M. V. Wickerhauser, "Signal processing and compression with wavelet packets," in *Wavelets and their applications*: Springer, 1994, pp. 363-379.
[151] C. Taswell, "The what, how, and why of wavelet shrinkage denoising," *Computing in Science & Engineering,* vol. 2, no. 3, pp. 12-19, 2000.
[152] D. L. Donoho and J. M. Johnstone, "Ideal spatial adaptation by wavelet shrinkage," *Biometrika,* vol. 81, no. 3, pp. 425-455, 1994.
[153] H. Y. Gao, "Choice of thresholds for wavelet shrinkage estimate of the spectrum," *Journal of Time Series Analysis,* vol. 18, no. 3, pp. 231-251, 1997.
[154] P. Moulin, "Wavelet thresholding techniques for power spectrum estimation," *IEEE Transactions on Signal Processing,* vol. 42, no. 11, pp. 3126-3136, 1994.
[155] J. Joy, S. Peter, and N. John, "Denoising using soft thresholding," *International Journal of Advanced Research in Electrical, Electronics and Instrumentation Engineering,* vol. 2, no. 3, pp. 1027-1032, 2013.
[156] A. Papoulis, *Random variables and stochastic processes*. McGraw Hill, 1965.

[157] D. Kannan, *An introduction to stochastic processes*. New York: New York : North Holland, 1979.
[158] C. L. Nikias and J. M. Mendel, "Signal processing with higher-order spectra," *IEEE Signal Processing Magazine,* vol. 10, no. 3, pp. 10-37, 1993.
[159] R. J. Hyndman and G. Athanasopoulos, *Forecasting: principles and practice*. OTexts, 2018.
[160] A. Burkov, *The hundred-page machine learning book*. Andriy Burkov Quebec City, QC, Canada, 2019.
[161] J. Snoek, H. Larochelle, and R. P. Adams, "Practical bayesian optimization of machine learning algorithms," *Advances in Neural Information Processing Systems,* vol. 25, p. 2951, 2012.
[162] H. Gould, J. Tobochnik, and W. Christian, "An introduction to computer simulation methods," *Comput. Phys,* vol. 10, pp. 652-653, 2007.
[163] A. Géron, *Hands-on machine learning with Scikit-Learn, Keras, and TensorFlow: Concepts, tools, and techniques to build intelligent systems*. O'Reilly Media, Inc., 2019.
[164] A. Zhang, Z. C. Lipton, M. Li, and A. J. Smola, "Dive into deep learning," *arXiv:2106.11342 [cs.LG],* 2021.
[165] K. Hornik, "Some new results on neural network approximation," *Neural networks,* vol. 6, no. 8, pp. 1069-1072, 1993.
[166] K. Hornik, M. Stinchcombe, and H. White, "Universal approximation of an unknown mapping and its derivatives using multilayer feedforward networks," *Neural Networks,* vol. 3, no. 5, pp. 551-560, 1990.
[167] K. Hornik, "Approximation capabilities of multilayer feedforward networks," *Neural Networks,* vol. 4, no. 2, pp. 251-257, 1991.
[168] K. Hornik, M. Stinchcombe, and H. White, "Multilayer feedforward networks are universal approximators," *Neural Networks,* vol. 2, no. 5, pp. 359-366, 1989.
[169] Y. LeCun, L. Bottou, Y. Bengio, and P. Haffner, "Gradient-based learning applied to document recognition," *Proceedings of the IEEE,* vol. 86, no. 11, pp. 2278-2324, 1998.
[170] A. Krizhevsky, I. Sutskever, and G. E. Hinton, "Imagenet classification with deep convolutional neural networks," *Advances in Neural Information Processing Systems,* vol. 25, pp. 1097-1105, 2012.
[171] C. Szegedy *et al.*, "Going deeper with convolutions," in *Proc. IEEE Conf. on Computer Vision and Pattern Recognition (CVPR)*, 2015, pp. 1-9.
[172] K. Simonyan and A. Zisserman, "Very deep convolutional networks for large-scale image recognition," *arXiv:1409.1556 [cs.CV],* 2014.
[173] D. Bahdanau, K. Cho, and Y. Bengio, "Neural machine translation by jointly learning to align and translate," *arXiv:1409.0473 [cs.CL],* 2014.
[174] A. Vaswani *et al.*, "Attention is all you need," in *Advances in Neural Information Processing Systems*, 2017, pp. 5998-6008.
[175] R. C. Staudemeyer and E. R. Morris, "Understanding LSTM – a tutorial into long short-term memory recurrent neural networks," *arXiv:1909.09586 [cs.NE],* 2019.

[176] A. Sherstinsky, "Fundamentals of recurrent neural network (RNN) and long short-term memory (LSTM) network," *Physica D: Nonlinear Phenomena,* vol. 404, p. 132306, 2020.
[177] R. Sutton, "Two problems with back propagation and other steepest descent learning procedures for networks," in *Proceedings of the Eighth Annual Conference of the Cognitive Science Society*, 1986, pp. 823-832.
[178] N. Qian, "On the momentum term in gradient descent learning algorithms," *Neural networks,* vol. 12, no. 1, pp. 145-151, 1999.
[179] J. Duchi, E. Hazan, and Y. Singer, "Adaptive subgradient methods for online learning and stochastic optimization," *Journal of Machine Learning Research,* vol. 12, no. 7, pp. 2121-2159, 2011.
[180] J. Dean *et al.*, "Large scale distributed deep networks," *Advances in neural information processing systems,* vol. 25, 2012.
[181] G. Hinton, S. Nitish, and K. Swersky, "Divide the gradient by a running average of its recent magnitude," *Neural Networks for Machine Learning,* 2011.
[182] M. D. Zeiler, "ADADELTA: an adaptive learning rate method," *arXiv:1212.5701 [cs.LG],* 2012.
[183] D. P. Kingma and J. Ba, "Adam: A method for stochastic optimization," *arXiv:1412.6980 [cs.LG],* 2014.
[184] S. J. Reddi, S. Kale, and S. Kumar, "On the convergence of adam and beyond," *arXiv:1904.09237 [cs.LG],* 2019.
[185] S. Ioffe and C. Szegedy, "Batch normalization: Accelerating deep network training by reducing internal covariate shift," in *Proc. Int. Conf. on Machine Learning (ICML)*, 2015, pp. 448-456.
[186] N. Srivastava, G. Hinton, A. Krizhevsky, I. Sutskever, and R. Salakhutdinov, "Dropout: a simple way to prevent neural networks from overfitting," *The journal of machine learning research,* vol. 15, no. 1, pp. 1929-1958, 2014.
[187] D. Mishkin and J. Matas, "All you need is a good init," *arXiv:1511.06422 [cs.LG],* 2015.
[188] K. He, X. Zhang, S. Ren, and J. Sun, "Delving deep into rectifiers: Surpassing human-level performance on imagenet classification," in *Proceedings of the IEEE international conference on computer vision*, 2015, pp. 1026-1034.
[189] X. Glorot and Y. Bengio, "Understanding the difficulty of training deep feedforward neural networks," in *Proceedings of the thirteenth international conference on artificial intelligence and statistics*, 2010: JMLR Workshop and Conference Proceedings, pp. 249-256.
[190] P. A. Huijing, "Architecture of the human gastrocnemius muscle and some functional consequences," *Cells Tissues Organs,* vol. 123, no. 2, pp. 101-107, 1985.
[191] N. J. Cronin, J. Avela, T. Finni, and J. Peltonen, "Differences in contractile behaviour between the soleus and medial gastrocnemius muscles during human walking," *Journal of Experimental Biology,* vol. 216, no. 5, pp. 909-914, 2013.
[192] A. Werkhausen, S. Willwacher, and K. Albracht, "Medial gastrocnemius muscle fascicles shorten throughout stance during sprint acceleration," *Scandinavian journal of medicine & science in sports,* vol. 31, no. 7, pp. 1471-1480, 2021.

[193] K. K. Rana, S. Das, and R. Verma, "Double plantaris muscle: A cadaveric study with clinical importance," *Int J Morphol,* vol. 24, no. 3, pp. 495-8, 2006.
[194] D. Landin, M. Thompson, and M. Reid, "Knee and ankle joint angles influence the plantarflexion torque of the gastrocnemius," *Journal of clinical medicine research,* vol. 7, no. 8, p. 602, 2015.
[195] M. Murray, G. Guten, J. Baldwin, and G. Gardner, "A comparison of plantar flexion torque with and without the triceps surae," *Acta Orthopaedica Scandinavica,* vol. 47, no. 1, pp. 122-124, 1976.
[196] T. Fukunaga *et al.*, "Physiological cross‐sectional area of human leg muscles based on magnetic resonance imaging," *Journal of orthopaedic research,* vol. 10, no. 6, pp. 926-934, 1992.
[197] Y.-W. Chang, R. E. Hughes, F.-C. Su, E. Itoi, and K.-N. An, "Prediction of muscle force involved in shoulder internal rotation," *Journal of Shoulder and Elbow Surgery,* vol. 9, no. 3, pp. 188-195, 2000.
[198] J. Ringelberg, "EMG and force production of some human shoulder muscles during isometric abduction," *Journal of biomechanics,* vol. 18, no. 12, pp. 939-947, 1985.
[199] A. Hof, "The relationship between electromyogram and muscle force," *Sportverletzung· Sportschaden,* vol. 11, no. 03, pp. 79-86, 1997.
[200] A. L. Hof, "EMG and muscle force: an introduction," *Human Movement Science,* vol. 3, no. 1-2, pp. 119-153, 1984.
[201] R. E. Hughes, "Force analysis of rotator cuff muscles," *Clinical Orthopaedics and Related Research®,* vol. 330, pp. 75-83, 1996.
[202] F. C. Van der Helm, "A finite element musculoskeletal model of the shoulder mechanism," *Journal of biomechanics,* vol. 27, no. 5, pp. 551-569, 1994.
[203] J. Challis and D. Kerwin, "An analytical examination of muscle force estimations using optimization techniques," *Proceedings of the Institution of Mechanical Engineers, Part H: Journal of Engineering in Medicine,* vol. 207, no. 3, pp. 139-148, 1993.
[204] R. A. Brand, D. R. Pedersen, and J. A. Friederich, "The sensitivity of muscle force predictions to changes in physiologic cross-sectional area," *Journal of biomechanics,* vol. 19, no. 8, pp. 589-596, 1986.
[205] H. J. Hermens *et al.*, "European recommendations for surface electromyography," *Roessingh research and development,* vol. 8, no. 2, pp. 13-54, 1999.
[206] D. Stegeman and H. Hermens, "Standards for surface electromyography: The European project Surface EMG for non-invasive assessment of muscles (SENIAM)," *Enschede: Roessingh Research and Development,* vol. 10, pp. 8-12, 2007.
[207] H. U. Kuriki, E. M. Mello, F. M. De Azevedo, L. S. O. Takahashi, N. Alves, and R. de Faria Negrão Filho, *The relationship between electromyography and muscle force*. Citeseer, 2012.
[208] J. H. Lawrence and C. De Luca, "Myoelectric signal versus force relationship in different human muscles," *Journal of Applied Physiology,* vol. 54, no. 6, pp. 1653-1659, 1983.
[209] B. Bigland-Ritchie, "EMG/force relations and fatigue of human voluntary contractions," *Exercise and sport sciences reviews,* vol. 9, no. 1, pp. 75-118, 1981.

[210] E. Henneman, G. Somjen, and D. O. Carpenter, "Functional significance of cell size in spinal motoneurons," *Journal of neurophysiology,* vol. 28, no. 3, pp. 560-580, 1965.
[211] E. Henneman and C. B. Olson, "Relations between structure and function in the design of skeletal muscles," *Journal of neurophysiology,* vol. 28, no. 3, pp. 581-598, 1965.
[212] J. V. Basmajian, "Their function revealed by Electromyography," *Muscle Alive,* vol. 212, 1985.
[213] S. Heintz and E. M. Gutierrez-Farewik, "Static optimization of muscle forces during gait in comparison to EMG-to-force processing approach," *Gait & posture,* vol. 26, no. 2, pp. 279-288, 2007.
[214] A. Hof, H. Elzinga, W. Grimmius, and J. Halbertsma, "Detection of non-standard EMG profiles in walking," *Gait & posture,* vol. 21, no. 2, pp. 171-177, 2005.
[215] D. A. Winter, *Biomechanics and motor control of human gait: normal, elderly and pathological*. University of Waterloo Press, 1991.
[216] M. M. Liu, W. Herzog, and H. H. Savelberg, "Dynamic muscle force predictions from EMG: an artificial neural network approach," *Journal of electromyography and kinesiology,* vol. 9, no. 6, pp. 391-400, 1999.
[217] M. M. Bamman, S. G. Ingram, J. F. Caruso, and M. C. Greenisen, "Evaluation of surface electromyography during maximal voluntary contraction," *The Journal of Strength & Conditioning Research,* vol. 11, no. 2, pp. 68-72, 1997.
[218] D. Tkach, H. Huang, and T. A. Kuiken, "Study of stability of time-domain features for electromyographic pattern recognition," *Journal of neuroengineering and rehabilitation,* vol. 7, no. 1, pp. 1-13, 2010.
[219] J. D. Silverman, G. Balbinot, K. Masani, J. Zariffa, and P. Eng, "Validity and reliability of surface electromyography features in lower extremity muscle contraction in healthy and spinal cord–injured participants," *Topics in Spinal Cord Injury Rehabilitation,* vol. 27, no. 4, pp. 14-27, 2021.
[220] M. L. Martin, K. J. Travouillon, P. A. Fleming, and N. M. Warburton, "Review of the methods used for calculating physiological cross‐sectional area (PCSA) for ecological questions," *Journal of Morphology,* vol. 281, no. 7, pp. 778-789, 2020.
[221] C. Gans, "The functional significance of muscle architecture: A theoretical analysis," *Adv Anat Embryol Cell Biol,* vol. 38, pp. 115-142, 1965.
[222] C. Gans and F. De Vree, "Functional bases of fiber length and angulation in muscle," *journal of Morphology,* vol. 192, no. 1, pp. 63-85, 1987.
[223] R. L. Lieber and J. Fridén, "Functional and clinical significance of skeletal muscle architecture," *Muscle & Nerve: Official Journal of the American Association of Electrodiagnostic Medicine,* vol. 23, no. 11, pp. 1647-1666, 2000.
[224] S. Medler, "Comparative trends in shortening velocity and force production in skeletal muscles," *American Journal of Physiology-Regulatory, Integrative and Comparative Physiology,* vol. 283, no. 2, pp. R368-R378, 2002.
[225] T. S. Buchanan, D. G. Lloyd, K. Manal, and T. F. Besier, "Neuromusculoskeletal modeling: estimation of muscle forces and joint moments and movements from measurements of neural command," *Journal of applied biomechanics,* vol. 20, no. 4, pp. 367-395, 2004.

[226] B. Bolsterlee, A. N. Vardy, F. C. van der Helm, and H. D. Veeger, "The effect of scaling physiological cross-sectional area on musculoskeletal model predictions," *Journal of biomechanics,* vol. 48, no. 10, pp. 1760-1768, 2015.
[227] Y. Huang, X. Fan, S. C. Chen, and N. Zhao, "Emerging technologies of flexible pressure sensors: materials, modeling, devices, and manufacturing," *Advanced functional materials,* vol. 29, no. 12, p. 1808509, 2019.
[228] RAL Deutsches Institut für Gütesicherung und Kennzeichnung e. V., "Medical compression hosiery – quality assurance," RAL Deutsches Institut für Gütesicherung und Kennzeichnung e.V.: Bonn, Germany, Bonn, Germany, RAL-GZ 387/1, 2008.
[229] L. Shu, "Wearable body area sensor networks for continuous dynamic health monitoring in daily activities: case study of intelligent footwear system," Ph.D. dissertation, Hong Kong Polytechnic University, 2012.
[230] S. Al-Sarawi, M. Anbar, K. Alieyan, and M. Alzubaidi, "Internet of Things (IoT) communication protocols," in *Proc. 8th Int. Conf. on Information Technology (ICIT)*, 2017: IEEE, pp. 685-690.
[231] W. Wang, S. L. Capitaneanu, D. Marinca, and E.-S. Lohan, "Comparative analysis of channel models for industrial IoT wireless communication," *IEEE Access,* vol. 7, pp. 91627-91640, 2019.
[232] D. Yang *et al.*, "Expert consensus on the metaverse in medicine," *Clinical eHealth,* vol. 5, pp. 1-9, 2022.
[233] J. Thomason, "MetaHealth-how will the metaverse change health care?," *Journal of Metaverse,* vol. 1, no. 1, pp. 13-16, 2021.
[234] I. Skalidis, O. Muller, and S. Fournier, "CardioVerse: the cardiovascular medicine in the era of metaverse," *Trends in Cardiovascular Medicine,* 2022.
[235] D. Chen and R. Zhang, "Exploring research trends of emerging technologies in health metaverse: a bibliometric analysis," *Available at SSRN 3998068,* 2022.
[236] Y. S. Dewi and G. S. Darma, "Shifting business strategy of international standard hospital in metaverse era," *JMMR (Jurnal Medicoeticolegal dan Manajemen Rumah Sakit),* vol. 11, no. 1, pp. 30-43, 2022.
[237] X. Wang, Y. Han, V. C. Leung, D. Niyato, X. Yan, and X. Chen, *Edge AI: Convergence of edge computing and artificial intelligence*. Springer, 2020.
[238] J. Shi *et al.*, "Smart textile‐integrated microelectronic systems for wearable applications," *Advanced materials,* vol. 32, no. 5, p. 1901958, 2020.
[239] S. Liu, K. Ma, B. Yang, H. Li, and X. Tao, "Textile electronics for VR/AR applications," *Advanced Functional Materials,* vol. 31, no. 39, p. 2007254, 2021.
[240] A. Servati, L. Zou, Z. J. Wang, F. Ko, and P. Servati, "Novel flexible wearable sensor materials and signal processing for vital sign and human activity monitoring," *Sensors,* vol. 17, no. 7, p. 1622, 2017.
[241] K. T. Sweeney, T. E. Ward, and S. F. McLoone, "Artifact removal in physiological signals—Practices and possibilities," *IEEE transactions on information technology in biomedicine,* vol. 16, no. 3, pp. 488-500, 2012.
[242] T. Tamura, Y. Maeda, M. Sekine, and M. Yoshida, "Wearable photoplethysmographic sensors—past and present," *Electronics,* vol. 3, no. 2, pp. 282-302, 2014.

[243] P. Celka *et al.*, "Wearable biosensing: signal processing and communication architectures issues," *Journal of Telecommunications and Information Technology,* pp. 90-104, 2005.
[244] R. Yousefi, M. Nourani, S. Ostadabbas, and I. Panahi, "A motion-tolerant adaptive algorithm for wearable photoplethysmographic biosensors," *IEEE Journal of Biomedical and Health Informatics,* vol. 18, no. 2, pp. 670-681, 2013.
[245] S. H. Kim, D. W. Ryoo, and C. Bae, "Adaptive noise cancellation using accelerometers for the PPG signal from forehead," in *Proc. 29th IEEE Eng. in Med. and Biol. Soc. (EMBS)*, 2007, pp. 2564-2567.
[246] L. Zou, X. Chen, A. Servati, S. Soltanian, P. Servati, and Z. J. Wang, "A blind source separation framework for monitoring heart beat rate using nanofiber-based strain sensors," *IEEE Sensors Journal,* vol. 16, no. 3, pp. 762-772, 2015.
[247] M. Raghuram, K. V. Madhav, E. H. Krishna, N. R. Komalla, K. Sivani, and K. A. Reddy, "Dual-tree complex wavelet transform for motion artifact reduction of PPG signals," in *Proc. IEEE Int. Symp. on Medical Measurements and Applications (MeMeA)*, 2012, pp. 1-4.
[248] Q. Wang, P. Yang, and Y. Zhang, "Artifact reduction based on Empirical Mode Decomposition (EMD) in photoplethysmography for pulse rate detection," in *Proc. IEEE Eng. in Med. and Biol. Soc. (EMBC)*, 2010: IEEE, pp. 959-962.
[249] W. Navaraj and R. Dahiya, "Fingerprint‐enhanced capacitive‐piezoelectric flexible sensing skin to discriminate static and dynamic tactile stimuli," *Advanced Intelligent Systems,* vol. 1, no. 7, p. 1900051, 2019.
[250] Y. Wang, X. Wu, D. Mei, L. Zhu, and J. Chen, "Flexible tactile sensor array for distributed tactile sensing and slip detection in robotic hand grasping," *Sensors and Actuators A: Physical,* vol. 297, p. 111512, 2019.
[251] K. Xu *et al.*, "Show, attend and tell: Neural image caption generation with visual attention," in *International conference on machine learning*, 2015, pp. 2048-2057.
[252] A. Karpathy and L. Fei-Fei, "Deep visual-semantic alignments for generating image descriptions," in *Proceedings of the IEEE conference on computer vision and pattern recognition*, 2015, pp. 3128-3137.
[253] O. Vinyals, A. Toshev, S. Bengio, and D. Erhan, "Show and tell: Lessons learned from the 2015 mscoco image captioning challenge," *IEEE transactions on pattern analysis and machine intelligence,* vol. 39, no. 4, pp. 652-663, 2016.
[254] J. Lu, C. Xiong, D. Parikh, and R. Socher, "Knowing when to look: Adaptive attention via a visual sentinel for image captioning," in *Proceedings of the IEEE conference on computer vision and pattern recognition*, 2017, pp. 375-383.
[255] K. Cho *et al.*, "Learning phrase representations using RNN encoder-decoder for statistical machine translation," *arXiv:1406.1078 [cs.CL],* 2014.
[256] I. Sutskever, O. Vinyals, and Q. V. Le, "Sequence to sequence learning with neural networks," *Advances in Neural Information Processing Systems,* vol. 27, 2014.
[257] A. Kumar and S. Sarawagi, "Calibration of encoder decoder models for neural machine translation," *arXiv:1903.00802 [cs.CL],* 2019.

[258] N. Kalchbrenner and P. Blunsom, "Recurrent continuous translation models," in *Proceedings of the 2013 conference on empirical methods in natural language processing*, 2013, pp. 1700-1709.
[259] A. See, P. J. Liu, and C. D. Manning, "Get to the point: Summarization with pointer-generator networks," *arXiv:1704.04368 [cs.CL],* 2017.
[260] R. Nallapati, B. Zhou, C. Gulcehre, and B. Xiang, "Abstractive text summarization using sequence-to-sequence rnns and beyond," *arXiv:1602.06023 [cs.CL],* 2016.
[261] K. Lopyrev, "Generating news headlines with recurrent neural networks," *arXiv:1512.01712 [cs.CL],* 2015.
[262] A. M. Rush, S. Chopra, and J. Weston, "A neural attention model for abstractive sentence summarization," *arXiv:1509.00685 [cs.CL],* 2015.
[263] J. Yin, X. Jiang, Z. Lu, L. Shang, H. Li, and X. Li, "Neural generative question answering," *arXiv:1512.01337 [cs.CL],* 2015.
[264] Y.-p. Nie, Y. Han, J.-m. Huang, B. Jiao, and A.-p. Li, "Attention-based encoder-decoder model for answer selection in question answering," *Frontiers of Information Technology & Electronic Engineering,* vol. 18, no. 4, pp. 535-544, 2017.
[265] S. Bae, D. Kim, J. Kim, and E. Choi, "Question answering for complex electronic health records database using unified encoder-decoder architecture," in *Machine Learning for Health*, 2021: PMLR, pp. 13-25.
[266] I. Allaouzi, M. B. Ahmed, and B. Benamrou, "An Encoder-Decoder model for visual question answering in the medical domain," in *CLEF (Working Notes)*, 2019.
[267] G. E. Hinton, S. Osindero, and Y.-W. Teh, "A fast learning algorithm for deep belief nets," *Neural computation,* vol. 18, no. 7, pp. 1527-1554, 2006.
[268] Y. Bengio, P. Lamblin, D. Popovici, and H. Larochelle, "Greedy layer-wise training of deep networks," *Advances in Neural Information Processing Systems,* vol. 19, 2006.
[269] J. Masci, U. Meier, D. Cireşan, and J. Schmidhuber, "Stacked convolutional auto-encoders for hierarchical feature extraction," in *International conference on artificial neural networks*, 2011: Springer, pp. 52-59.
[270] N. Srivastava, E. Mansimov, and R. Salakhudinov, "Unsupervised learning of video representations using lstms," in *International conference on machine learning*, 2015: PMLR, pp. 843-852.
[271] Y.-A. Chung, C.-C. Wu, C.-H. Shen, H.-Y. Lee, and L.-S. Lee, "Audio word2vec: Unsupervised learning of audio segment representations using sequence-to-sequence autoencoder," *arXiv:1603.00982 [cs.SD],* 2016.
[272] P. Vincent, H. Larochelle, I. Lajoie, Y. Bengio, P.-A. Manzagol, and L. Bottou, "Stacked denoising autoencoders: Learning useful representations in a deep network with a local denoising criterion," *Journal of machine learning research,* vol. 11, no. 12, 2010.
[273] P. Vincent, H. Larochelle, Y. Bengio, and P.-A. Manzagol, "Extracting and composing robust features with denoising autoencoders," in *Proceedings of the 25th international conference on Machine learning*, 2008, pp. 1096-1103.

[274] S. Rifai, P. Vincent, X. Muller, X. Glorot, and Y. Bengio, "Contractive auto-encoders: Explicit invariance during feature extraction," in *Proceedings of the International Conference on Machine Learning (ICML)*, 2011.
[275] A. Makhzani and B. Frey, "K-sparse autoencoders," *arXiv:1312.5663 [cs.LG],* 2013.
[276] A. Ng, "Sparse autoencoder (CS294A Lecture Notes)," Stanford University, Stanford, CA, 2011.
[277] D. P. Kingma and M. Welling, "Auto-encoding variational bayes," *arXiv:1312.6114 [cs.LG],* 2013.
[278] A. Makhzani, J. Shlens, N. Jaitly, I. Goodfellow, and B. Frey, "Adversarial autoencoders," *arXiv:1511.05644 [cs.LG],* 2015.
[279] J.-L. Lee and D.-S. Kim, "Segmented Two-Dimensional Progressive Polynomial Calibration Method for Nonlinear Sensors," *Sensors,* vol. 24, no. 21, p. 7058, 2024.
[280] A. Vaswani *et al.*, "Attention is all you need," *Advances in Neural Information Processing Systems,* vol. 30, 2017.
[281] J. Ho, A. Jain, and P. Abbeel, "Denoising diffusion probabilistic models," *Advances in Neural Information Processing Systems,* vol. 33, pp. 6840-6851, 2020.
[282] R. Rombach, A. Blattmann, D. Lorenz, P. Esser, and B. Ommer, "High-resolution image synthesis with latent diffusion models," in *Proceedings of the IEEE/CVF conference on computer vision and pattern recognition*, 2022, pp. 10684-10695.
[283] F. Guan *et al.*, "Silver nanowire–bacterial cellulose composite fiber-based sensor for highly sensitive detection of pressure and proximity," *ACS nano,* vol. 14, no. 11, pp. 15428-15439, 2020.
[284] Q. Zhang, Y. L. Wang, Y. Xia, P. F. Zhang, T. V. Kirk, and X. D. Chen, "Textile‐only capacitive sensors for facile fabric integration without compromise of wearability," *Advanced Materials Technologies,* vol. 4, no. 10, p. 1900485, 2019.
[285] J. Lee *et al.*, "Stretchable and suturable fibre sensors for wireless monitoring of connective tissue strain," *Nature Electronics,* vol. 4, no. 4, pp. 291-301, 2021.
[286] S. Choi *et al.*, "Conductive hierarchical hairy fibers for highly sensitive, stretchable, and water‐resistant multimodal gesture‐distinguishable sensor, VR applications," *Advanced Functional Materials,* vol. 29, no. 50, p. 1905808, 2019.
[287] A. Leber, C. Dong, R. Chandran, T. Das Gupta, N. Bartolomei, and F. Sorin, "Soft and stretchable liquid metal transmission lines as distributed probes of multimodal deformations," *Nature Electronics,* vol. 3, no. 6, pp. 316-326, 2020.
[288] F. Mokhtari, J. Foroughi, T. Zheng, Z. Cheng, and G. M. Spinks, "Triaxial braided piezo fiber energy harvesters for self-powered wearable technologies," *Journal of Materials Chemistry A,* vol. 7, no. 14, pp. 8245-8257, 2019.
[289] S. Ahn *et al.*, "Wearable multimode sensors with amplified piezoelectricity due to the multi local strain using 3D textile structure for detecting human body signals," *Nano Energy,* vol. 74, p. 104932, 2020.
[290] W. Yan *et al.*, "Single fibre enables acoustic fabrics via nanometre-scale vibrations," *Nature,* vol. 603, no. 7902, pp. 616-623, 2022.

[291] K. Dong, X. Peng, and Z. L. Wang, "Fiber/fabric‐based piezoelectric and triboelectric nanogenerators for flexible/stretchable and wearable electronics and artificial intelligence," *Advanced Materials,* vol. 32, no. 5, p. 1902549, 2020.
[292] C. Ning *et al.*, "Flexible and stretchable fiber‐shaped triboelectric nanogenerators for biomechanical monitoring and human‐interactive sensing," *Advanced Functional Materials,* vol. 31, no. 4, p. 2006679, 2021.
[293] C. Ning *et al.*, "Helical fiber strain sensors based on triboelectric nanogenerators for self-powered human respiratory monitoring," *Acs Nano,* vol. 16, no. 2, pp. 2811-2821, 2022.
[294] W. Yang *et al.*, "Self‐powered interactive fiber electronics with visual‐digital synergies," *Advanced Materials,* vol. 33, no. 45, p. 2104681, 2021.
[295] M. Chen *et al.*, "Imperceptible, designable, and scalable braided electronic cord," *Nature Communications,* vol. 13, no. 1, p. 7097, 2022.
[296] W. Liu, "Natural user interface-next mainstream product user interface," in *Proc. IEEE 11th Int. Conf. Comput.-Aided Ind. Design Concept*, 2010, vol. 1, pp. 203-205.
[297] X. Wang, X. Tao, and R. C. So, "A bio-mechanical model for elbow isokinetic and isotonic flexions," *Scientific reports,* vol. 7, no. 1, p. 8919, 2017.
[298] X. Wang, X. Tao, R. C. So, L. Shu, B. Yang, and Y. Li, "Monitoring elbow isometric contraction by novel wearable fabric sensing device," *Smart Materials and Structures,* vol. 25, no. 12, p. 125022, 2016.
[299] M. Saraswat and R. Tripathi, "Cloud computing: Analysis of top 5 CSPs in SaaS, PaaS and IaaS platforms," in *2020 9th International Conference System Modeling and Advancement in Research Trends (SMART)*, 2020: IEEE, pp. 300-305.
[300] C. M. Mohammed and S. R. Zeebaree, "Sufficient comparison among cloud computing services: IaaS, PaaS, and SaaS: A review," *International Journal of Science and Business,* vol. 5, no. 2, pp. 17-30, 2021.
[301] P. Hodges, L. Pengel, R. Herbert, and S. Gandevia, "Measurement of muscle contraction with ultrasound imaging," *Muscle & Nerve: Official Journal of the American Association of Electrodiagnostic Medicine,* vol. 27, no. 6, pp. 682-692, 2003.
[302] Y. Fujikoshi, "Two-way ANOVA models with unbalanced data," *Discrete Mathematics,* vol. 116, no. 1-3, pp. 315-334, 1993.
[303] M. Noordzij, G. Tripepi, F. W. Dekker, C. Zoccali, M. W. Tanck, and K. J. Jager, "Sample size calculations: basic principles and common pitfalls," *Nephrology dialysis transplantation,* vol. 25, no. 5, pp. 1388-1393, 2010.
[304] C. N. Maganaris, "Force‐length characteristics of the in vivo human gastrocnemius muscle," *Clinical Anatomy: The Official Journal of the American Association of Clinical Anatomists and the British Association of Clinical Anatomists,* vol. 16, no. 3, pp. 215-223, 2003.
[305] W. Herzog, L. Read, and H. Ter Keurs, "Experimental determination of force—length relations of intact human gastrocnemius muscles," *Clinical Biomechanics,* vol. 6, no. 4, pp. 230-238, 1991.

[306] C. N. Maganaris, "Force–length characteristics of in vivo human skeletal muscle," *Acta Physiologica Scandinavica,* vol. 172, no. 4, pp. 279-285, 2001.